

RL-TR-96-162
Final Technical Report
October 1996



OPTOELECTRONIC MQW DEVICES AND SYSTEMS FOR APPLICATION IN OPTICALLY CONTROLLED MILLIMETER- WAVE OSCILLATORS

University of Michigan

Sponsored by
Advanced Research Projects Agency
ARPA Order No. 8556

APPROVED FOR PUBLIC RELEASE; DISTRIBUTION UNLIMITED.

19961125 039

The views and conclusions contained in this document are those of the authors and should not be interpreted as necessarily representing the official policies, either expressed or implied, of the Advanced Research Projects Agency or the U.S. Government.

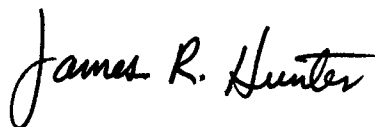
DTIC QUALITY INSPECTED 3

Rome Laboratory
Air Force Materiel Command
Rome, New York

This report has been reviewed by the Rome Laboratory Public Affairs Office (PA) and is releasable to the National Technical Information Service (NTIS). At NTIS it will be releasable to the general public, including foreign nations.

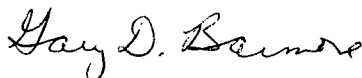
RL-TR-96-162 has been reviewed and is approved for publication.

APPROVED:



JAMES R. HUNTER
Project Engineer

FOR THE COMMANDER:



GARY D. BARMORE, Maj, USAF
Deputy Director
Surveillance & Photonics Directorate

If your address has changed or if you wish to be removed from the Rome Laboratory mailing list, or if the addressee is no longer employed by your organization, please notify RL/OCPC, 25 Electronic PKY, Rome, NY 13441-4514. This will assist us in maintaining a current mailing list.

Do not return copies of this report unless contractual obligations or notices on a specific document require that it be returned.

OPTOELECTRONIC MQW DEVICES AND SYSTEMS FOR APPLICATION
IN OPTICALLY CONTROLLED MILLIMETER-WAVE OSCILLATORS

Contractor: University of Michigan
Contract Number: F30602-92-C-0087
Effective Date of Contract: 22 May 1992
Contract Expiration Date: 31 December 1995
Short Title of Work: Optoelectronic MQW Devices and Systems
for Application in Optically Controlled
Millimeter-wave Oscillators

Period of Work Covered: May 92 - Dec 95

Principal Investigator: Dr. P. Bhattacharya
Phone: (313) 763-6678

RL Project Engineer: James R. Hunter
Phone: (315) 330-7045

Approved for public release; distribution unlimited.

This research was supported by the Advanced Research Projects
Agency of the Department of Defense and was monitored by
James R. Hunter, Rome Laboratory/OCPC, 25 Electronic Pky
Rome, NY 13441-4514.

REPORT DOCUMENTATION PAGE			Form Approved OMB No. 0704-0188	
Public reporting burden for this collection of information is estimated to average 1 hour per response, including the time for reviewing instructions, searching existing data sources, gathering and maintaining the data needed, and completing and reviewing the collection of information. Send comments regarding this burden estimate or any other aspect of this collection of information, including suggestions for reducing this burden, to Washington Headquarters Services, Directorate for Information Operations and Reports, 1215 Jefferson Davis Highway, Suite 1204, Arlington, VA 22202-4302, and to the Office of Management and Budget, Paperwork Reduction Project (0704-0188), Washington, DC 20503.				
1. AGENCY USE ONLY (Leave blank)	2. REPORT DATE October 1996	3. REPORT TYPE AND DATES COVERED FINAL MAY 92 - DEC 95		
4. TITLE AND SUBTITLE Optoelectronic MQW Devices and Systems for Application in Optically Controlled Millimeter-Wave Oscillators		5. FUNDING NUMBERS C - F30602-92-C-0087 PE - 61101E PR - H556 TA - 00 WU - 01		
6. AUTHOR(S) P. Bhattacharya, G.I. Haddad, J. Singh				
7. PERFORMING ORGANIZATION NAME(S) AND ADDRESS(ES) University of Michigan Department of Electrical Engineering and Computer Science Ann Arbor MI 48109-2122		8. PERFORMING ORGANIZATION REPORT NUMBER		
9. SPONSORING / MONITORING AGENCY NAME(S) AND ADDRESS(ES) ARPA/MTO 3701 NORTH FAIRFAX DR. ARLINGTON VA 22203-1714		10. SPONSORING / MONITORING AGENCY REPORT NUMBER RL-TR-96-162		
11. SUPPLEMENTARY NOTES ARPA Technical: Brian Hendrickson Rome Laboratory Project Engineer: J. HUNTER/OCPC/(315)330-7045				
12a. DISTRIBUTION AVAILABILITY STATEMENT Approved for public release; distribution unlimited.		12b. DISTRIBUTION CODE		
13. ABSTRACT (Maximum 200 words) The objective of this program was the realization of optically controlled millimeter-wave and microwave GaAs and InP-based circuits. The primary goal was the development of heterojunction bipolar transistors (HBTs) with the ability to be controlled optically. Of particular interest is the ability to convert a microwave signal modulated onto an optical carrier into an electrical signal which in turn will be used to injection-lock a microwave oscillator. This optically injection-locked oscillator has application to optically implemented control of phased array antenna systems. This report documents significant device developments such as a high-frequency, discrete device for injection locking (InP based MODFET with $f_{max} \sim 300$ GHz; GaAs based HBTs with $f_{max} \sim 90$ GHz; InP based HBTs with $f_{max} \sim 110$ GHz), an Indium-Tin-Oxide (ITO) transparent ohmic contact technology, a high speed Barrier Reservoir and Quantum Well Electron Transport (BRAQWET) modulator (17 GHz bandwidth in GaAs based devices), and monolithically integrated oscillator circuits with guided wave optical injection with tuning range of 100 MHz injection-locked at 14 GHz.				
14. SUBJECT TERMS optically controlled oscillator, Quantum Well Modulator, Optical injection-locking		15. NUMBER OF PAGES		
		16. PRICE CODE		
17. SECURITY CLASSIFICATION OF REPORT UNCLASSIFIED	18. SECURITY CLASSIFICATION OF THIS PAGE UNCLASSIFIED	19. SECURITY CLASSIFICATION OF ABSTRACT UNCLASSIFIED	20. LIMITATION OF ABSTRACT UNLIMITED	

NSN 7540-01-280-5500

DTIC QUALITY INSPECTED 3

Standard Form 298 (Rev. 2-89)
Prescribed by ANSI Std. Z39-18
298-102

CHAPTER I

INTRODUCTION

1.1 Forward

With the ever increasing need to transfer greater amounts of information, communication systems are rapidly being changed over from electrical signals being sent over wires to optical signals being sent over high bandwidth optical fibers. However, while optics may be superior for many applications such as data transmission, electronics are still superior for other applications such as the processing of information. Obviously, the high-speed conversion of information from optical to electronic form, and the reverse, is a topic of much importance.

This report is concerned primarily with the development of heterojunction bipolar transistors (HBTs) with the ability to be controlled optically. Of particular interest is the ability to convert a microwave signal modulated onto an optical carrier into an electrical signal which in turn will be used to injection-lock a microwave oscillator. The principal application of an optically injection locked oscillator is for use in an optically controlled phased array antenna system.

1.2 Phased Array Antenna Systems

Future generations of phased array antenna systems will require thousands of active radiating elements to achieve the necessary ultra-narrow beam profiles. Individual monolithic microwave integrated circuit (MMIC) transmit-receive modules in the large array must be synchronized to a master oscillator for the radiating elements to coherently combine and form a single beam. Conventional systems using metal waveguides or coaxial cables quickly become too heavy and unwieldy as the number of array elements increases.

Optical fiber links carrying the microwave reference signals on a modulated optical carrier have been proposed for the large array systems [1]. This method, pictured in Fig. 1.1, has several advantages. First, the optical fibers replace metal waveguides or coaxial cables, greatly reducing the weight of the system. Second, the master oscillator is protected from possible reflections caused at the locked oscillator. Finally, the use of optical fiber insures immunity from electromagnetic interference. At the transmit/receive module, the modulated light is either converted into an electrical signal and used to injection lock a local oscillator, or the light could be used to directly control an active element in the local oscillator, thus reducing system complexity.

1.3 Optical Control of Microwave Oscillators

The use of optical signals to control high speed electronic circuits is advantageous due to the wide bandwidth of the optical control signals and their inherent isolation from RF signals. Optical signals can be routed via lightweight fiber or monolithically integrated optical waveguides without affecting signals

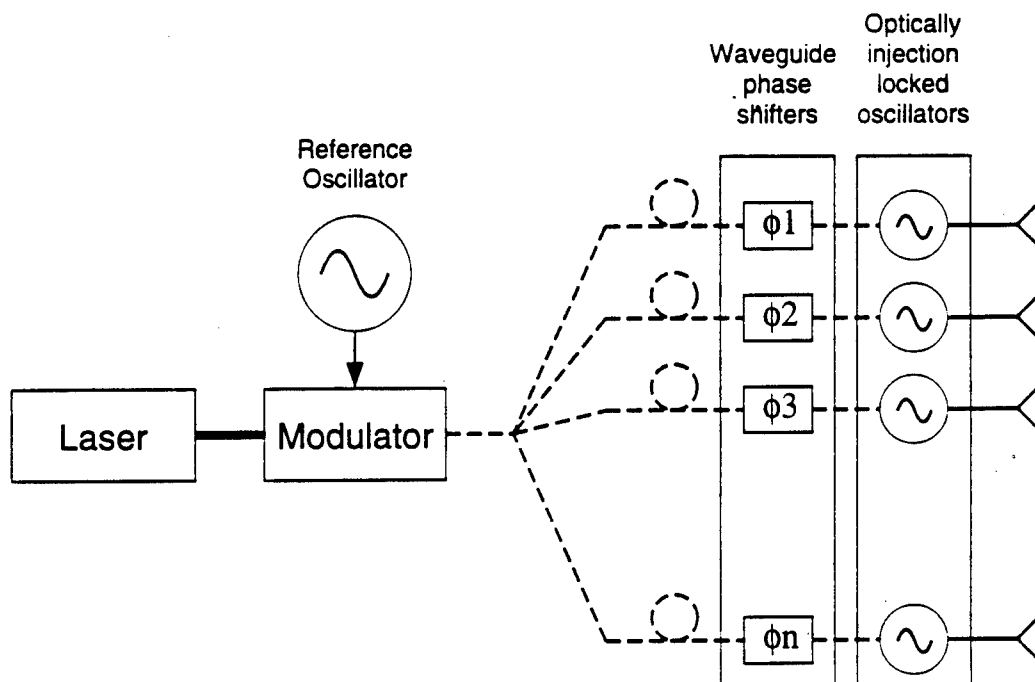


Figure 1.1: Phased array system using optical fibers for distribution of the reference oscillations. At the transmit/receive module, the modulated light is converted into an electrical signal and used to injection lock a local oscillator.

transmitted on microwave waveguides [2].

The optical control of microwave oscillators can be realized in one or more of three basic forms: Optical switching, optical tuning, and optical injection locking. Figure 1.2 shows the basic characteristics of each approach [3]. With optical switching, the intensity of the input light controls the output power of the oscillator — primarily applied in a non-linear fashion for turning on and off the controlled oscillator. With optical tuning, the intensity of the input light controls the output frequency of the oscillator.

Optical injection locking refers to the use of a high-frequency modulated optical control signal to fix the frequency of a free-running oscillator. When in locked condition, the oscillator will oscillate at the same frequency as the injection locking signal. There will be a phase offset ϕ between the oscillator's output signal and the injected signal. The phase offset varies by $\pm 90^\circ$ over the injection locking bandwidth ω_{max} . The injection locking bandwidth and phase error were theoretically modeled by Alder [4] in 1946 and are analytically represented as

$$\omega_{max} = \frac{\omega_o}{2Q} \sqrt{\frac{P_{inj}}{P_o}} \quad (1.1)$$

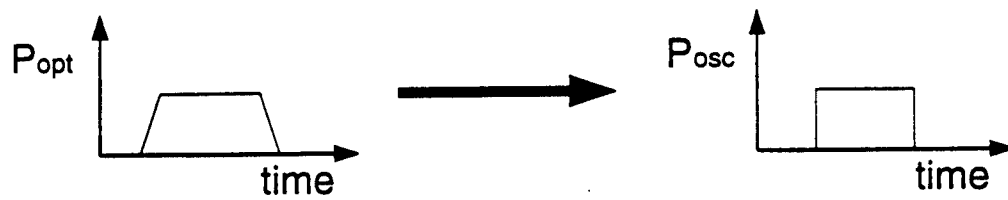
and

$$\phi = \sin^{-1} \left(\frac{\omega_{lock} - \omega_o}{\omega_{max}} \right), \quad (1.2)$$

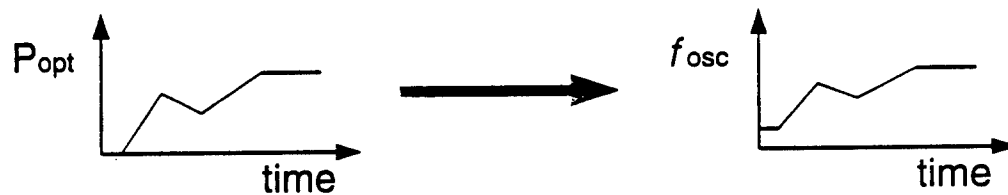
where ω_o is the free running oscillation frequency, ω_{lock} is the injection locking frequency, P_{inj} and P_o are the injected power and oscillator output power and Q is the quality factor of the oscillator. Q provides a measure for loss in the resonant circuit and is defined as

$$Q = \omega \frac{(\text{average energy stored})}{(\text{energy loss/second})} \quad (1.3)$$

a) Optical Switching



b) Optical Tuning



c) Optical Injection Locking

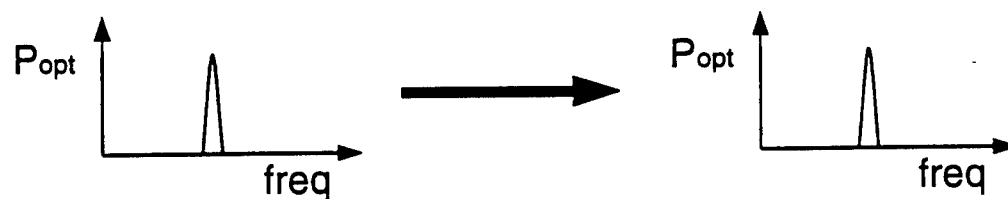


Figure 1.2: Three optical control methods for oscillators: a) optical switching, b) optical tuning, and c) optical injection locking.

Equation 1.1 shows that the injection locking range should have a square root dependence on the injected signal power. Furthermore, the quality factor of an oscillator can be experimentally determined by using Eqn. 1.1 in conjunction with a controlled injection locking experiment.

Optical tuning and injection locking effects of microwave oscillators have previously been studied for GaAs MESFET [5, 6, 7], and InGaAs/InAlAs MOD-FET based oscillators [8, 9, 10]. However, little work has been done on the optical control of high-speed heterojunction bipolar transistor (HBT) based circuits due to difficulties in coupling light into the devices. While FET devices have an advantage of easier light coupling through the gate-source and gate-drain openings, the use of HBT devices offers several significant advantages.

1.4 Heterojunction Bipolar Transistors for Optical Control Applications

Using HBTs as the active devices in microwave oscillator circuits provides several advantages [11]. The distances that determine carrier transit time are controlled by epitaxial growth rather than lithography. Therefore, high performance devices are possible without requiring submicron lithography. Higher current densities are possible since the entire emitter area conducts current rather than just a thin conducting channel. Also, devices are shielded from traps in the bulk and surface regions, contributing to a low $\frac{1}{f}$ noise and trap-induced frequency dependence. This is attractive for low phase noise microwave oscillator applications.

For optical control implementations, HBTs again have several advantages over MESFETs. The HBT has a greater optical absorption length. The HBT

also has photocurrent gain. Due to these factors, the HBT has a larger photoresponse which in turn should result in a larger optical tuning range and injection locking bandwidth.

To use an HBT for optical control, it is important that the photogenerated carriers have the maximum effect on the operation of the device. Ideally, any photocurrent generated should be amplified by transistor action for best responsivity. For the HBT, this would require that all photo-generated carriers be either in the base or in the base/collector depletion region. Fortunately, due to the heterojunction nature of the HBT, this requirement is intrinsically satisfied. Since the emitter is a wider band gap material than the base and collector in a single-heterostructure bipolar transistor (SHBT), photons with energies less than the band gap of the emitter but greater than the band gap of the base will find the emitter transparent and will not be absorbed until they reach the desired location.

The primary disadvantage of using HBTs is that light access is difficult because standard high-frequency HBT designs utilize a self-aligned emitter and base metalization which blocks access to the desired absorption regions. In this work, several different novel device designs are used to allow direct light access into an HBT.

There is a wide variety of heterostructure materials to choose from when designing an HBT. Figure 1.3 shows the band-gaps and lattice constants of several common compound semiconductors. For growth on GaAs substrates, the $\text{Al}_x\text{Ga}_{1-x}\text{As}$ ternary alloy and $\text{In}_{0.5}\text{Ga}_{0.5}\text{P}$ offer a wide range of choices for lattice matched heterostructures. In the InP system, $\text{In}_{.53}\text{Ga}_{.47}\text{As}$, $\text{In}_{.52}\text{Al}_{.48}\text{As}$, and the quaternary systems $\text{In}_{1-x}\text{Ga}_x\text{As}_y\text{P}_{1-y}$ and $\text{In}_x\text{Ga}_y\text{Al}_{1-x-y}\text{As}$ are pos-

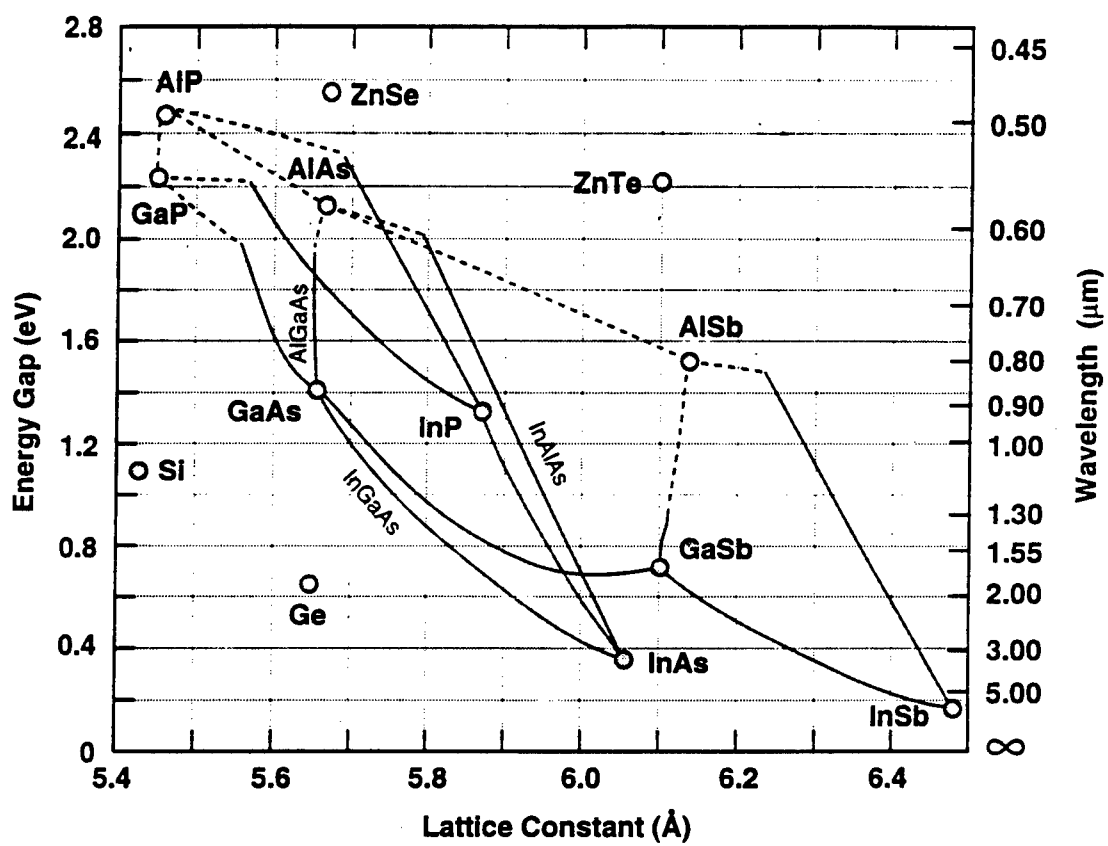


Figure 1.3: Bandgaps of common compound semiconductors and their alloys

sible choices. In this work, HBTs based on both the $\text{Al}_x\text{Ga}_{1-x}\text{As}/\text{GaAs}$ and $\text{In}_{.52}\text{Al}_{.48}\text{As}/\text{In}_{.53}\text{Ga}_{.47}\text{As}$ heterojunctions have been used.

1.5 Optical Modulators

One important issue in the optical control of microwave systems that cannot be overlooked, is the availability of stable high frequency modulated optical sources. For practical optical systems, the compact size of the semiconductor laser makes it the preferred light source. While semiconductor lasers can be directly modulated, with today's technology very high modulation bandwidths are only achieved with operation at high photon densities [12, 13] which compromises the long term reliability of the laser. The use of an external modulator in conjunction with a semiconductor laser offers the potential to realize high modulation bandwidths in practical systems [14]. This work has investigated a semiconductor waveguide intensity modulator based on electroabsorption in a blockaded reservoir and quantum well electron transfer (BRAQWET) structure.

CHAPTER II

FABRICATION PROCESSES AND DEVICE LAYOUT FOR OPTO-ELECTRONIC DEVICES

2.1 Introduction

In this chapter, the techniques that were used to fabricate the different HBT structures and waveguide optical modulators are presented. Section 2.2 will discuss the individual process steps required for device processing while sections 2.3–2.6 will present the different fabrication processes and device layouts used for making the devices discussed in the following chapters.

2.2 Processing Techniques

Due to the wide variety of materials used in opto-electronic devices, a wide and varied knowledge of the various etching, metalization, and fabrication processes is important. In this section, the various wet chemical etching techniques utilized for this work are discussed. Also, the use of ion implantation for the selective passivation of GaAs and related materials is discussed in detail. For discussions on RIE dry etching techniques and ohmic contacts to III/V semiconductors, the reader is referred to references [15] and [16].

2.2.1 Wet Chemical Etching

$\text{H}_3\text{PO}_4 : \text{H}_2\text{O}_2 : \text{H}_2\text{O}$ (1:1:20)

The $\text{H}_3\text{PO}_4 : \text{H}_2\text{O}_2 : \text{H}_2\text{O}$ etch mixture is useful for etching $\text{Al}_x\text{Ga}_{1-x}\text{As}$, $\text{In}_{.53}\text{Ga}_{.47}\text{As}$, and $\text{In}_{.52}\text{Al}_{.48}\text{As}$ [17, 18]. It is selective against etching P containing compounds. This etch proceeds with the oxidation of the semiconductor surface by the H_2O_2 . The oxide is then dissolved by the H_3PO_4 . The etch rate in the (1:1:20) concentration is approximately 250 nm/min and scales linearly with concentration (eg. (1:1:40) etches at 120 nm/min). This etch has serious undercutting problems when the Ni/Ge/Au/Ti/Au ohmic contact is exposed to the etch solution. $\text{NH}_4\text{OH} : \text{H}_2\text{O}_2 : \text{H}_2\text{O}$ should be used for GaAs etches in these cases.

$\text{HCl} : \text{H}_3\text{PO}_4$ (1:6)

The $\text{HCl} : \text{H}_3\text{PO}_4$ etch mixture etches InP and InGaP [19]. It is selective against As containing compounds. HCl is the reactive species in this etch mixture. However, a pure HCl etch is very fast and results in a rough etch surface. H_3PO_4 serves to slow down the etch rate so that the etched surface is smooth. The etch rate of InP with this etchant is about 500 nm/min.

$\text{HBr} : \text{SBW} : \text{H}_2\text{O}$ (1:10:40)

The saturated bromine water (SBW) mixture is required for removal of InGaAsP since $\text{H}_3\text{PO}_4 : \text{H}_2\text{O}_2 : \text{H}_2\text{O}$ will not etch P containing materials and $\text{HCl} : \text{H}_3\text{PO}_4$ is selective against As. This etchant is non-selective for most compound semiconductor materials [20]. Unfortunately, the etch is non-uniform and results in a deeper etch next to masked features than in open areas. Etch rates vary: 250 nm/min for InP, 140 nm/min for InAlAs and InGaAs, and about

100 nm/min for InGaAsP.

NH₄OH : H₂O₂ : H₂O (16:40:2000)

The ammonium-hydroxide (NH₄OH) etch is a very well controlled etchant for GaAs and AlGaAs. This etch is selective against In containing compounds. In the standard mixture, this etchant has similar etch rates of ~240 nm/min for Al_xGa_{1-x}As with aluminum content below 50% (which accounts for almost all situations encountered in opto-electronic device processing). However, this etchant can also provide an excellent selective etch of GaAs over AlGaAs if the pH of the solution is controlled [21, 22]. For instance, a selectivity of 100:1 for GaAs over Al_{0.3}Ga_{0.7}As is achieved for a mixture with a pH of 8.4.

HCl : H₂O (3:1)

The HCl : H₂O (3:1) etchant has been found to provide a selective etch for In_{0.52}Al_{0.48}As over In_{0.53}Ga_{0.47}As [23]. Note that in lower concentrations (say, 1:1), this etchant does not attack either InGaAs or InAlAs. The etch rate of InAlAs is approximately 650 nm/min. However, the etch surface is very rough — so rough that it appears darkened to the eye. However, since it doesn't etch InGaAs, the surface becomes smooth again once an InGaAs stop layer is reached. Etch endpoint detection is possible simply by observing when the darkened InAlAs etch surface clears when the InGaAs stop layer is reached. This would not be a useful etch without the use of a InGaAs stop layer. Care must also be taken as this provides a very fast etch for InP and InGaP.

2.2.2 O⁺ Implantation for Passivation of GaAs

Ion implant isolation is an effective and commonly used method for providing electrical isolation between neighboring GaAs semiconductor devices [15]. Very high resistivities ($\geq 10^7$ cm) are commonly achieved in GaAs implanted with oxygen. The technique relies on the creation of deep level centers by ion bombardment which trap the charge carriers in the material. At normal operating temperatures, these deep levels are not significantly thermally ionized and therefore the material is rendered electrically passivated [24]. With O⁺ implantation, the deep level traps are created by implantation damage rather than the presence of the oxygen ions. In fact, when O⁺ implant isolated GaAs is annealed at temperatures higher than 550° C, the crystal damage is repaired and compensation effects are cancelled [24].

One useful feature of implant isolation is the ability to selectively passivate epitaxial layers. Since electrical passivation is achieved by compensation of charge carriers, it is possible to choose implant dosages which will fully compensate lightly doped layers while leaving heavily doped layers unaffected. An important example of this is in high performance HBT designs [25, 26]. To reduce the base-collector capacitance, a low dosage implantation is performed through the base, collector and sub-collector layers in the regions of the device not directly under the emitter mesa structures. The lightly doped collector region is passivated, but the heavily doped base and sub-collector regions are not significantly affected. This results in a significant reduction of base-collector capacitance while still allowing for low resistance base and collector contacts.

This production of semi-insulating layers also applies to related compounds such as GaP [27] and In₅₂Al₄₈As [28]. Unfortunately, the implant isolation

technique does not work as well with $\text{In}_{.53}\text{Ga}_{.47}\text{As}$ and InP . In these materials, the damage centers form donor-like traps [29]. With careful tailoring of implant dosage, compensation of p -type material is possible but the maximum resistivity is low ($\approx 10^6 \text{ cm}$). Too high of a dosage will cause p -type materials to become slightly n -type. Passivation of n -type InP or $\text{In}_{.53}\text{Ga}_{.47}\text{As}$ is basically ineffective with maximum resistivities in the 10^3 – 10^4 cm range.

High Energy Implantation

One important recent development is the use of a single high-energy implantation step [30, 31] instead of the more common use of multiple implants at low ion energies. Figures 2.1 (a) and (b) show TRIM [32] damage profiles which compare the use of a multiple keV O^+ implantation sequence to a single 5 MeV O^+ implant. As can be seen, the single MeV implant produces the same vacancy concentrations in the device region as the multiple implant process. The heavy damage associated with the stopping of the O^+ ion is confined to the substrate where it has no effect on device performance. HBTs fabricated using the standard multiple keV implant procedure show undesirable parasitic current components [33] which are possibly due to the presence of implanted oxygen atoms in the semiconductor layers near the active device. The use of a single high-energy O^+ implantation is therefore preferable for HBT fabrication.

2.3 Circular Emitter HBT Fabrication

The “OPHBT” mask set contains non-self aligned devices with circular emitters. Light access is possible through a round hole in the center of the ring-shaped emitter contact. A mesa etch to the semi-insulating substrate is used

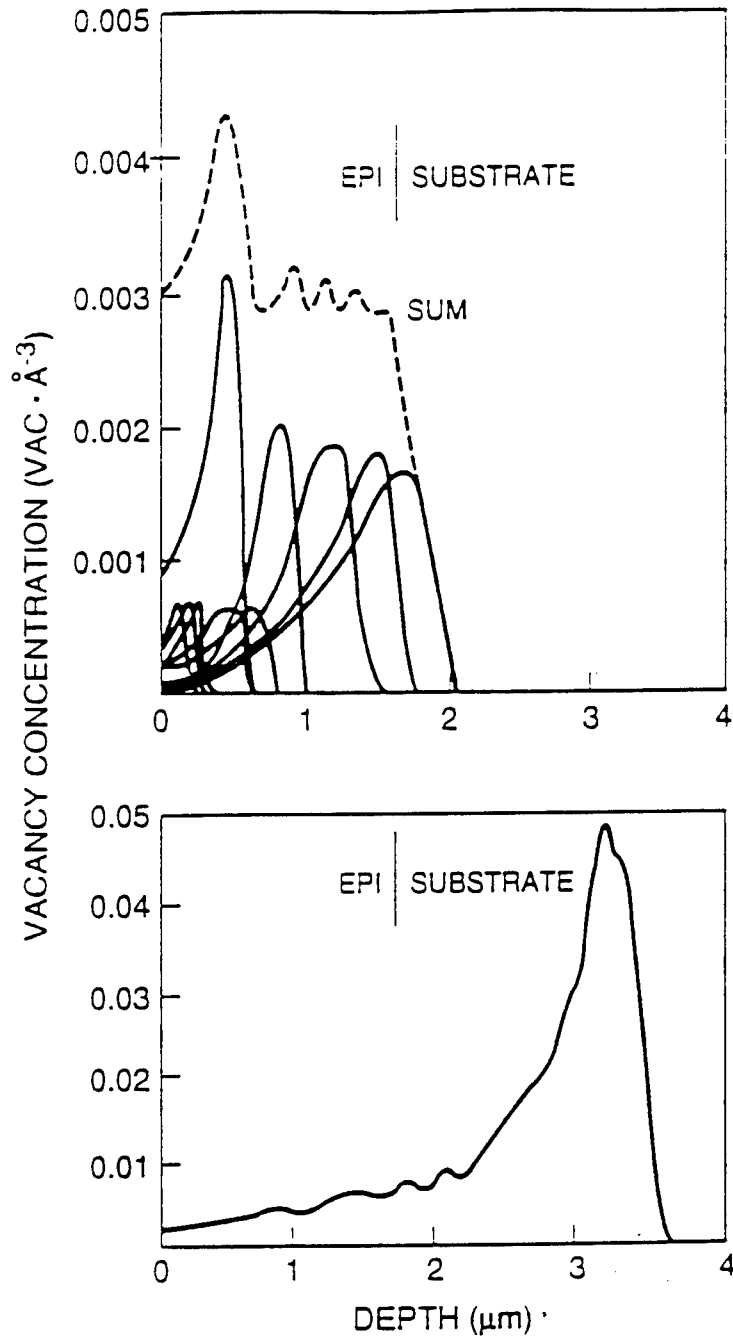


Figure 2.1: Vacancy profiles created in GaAs by (a) multiple O^+ implantations at 40, 100, 200 and 250 keV compared to (b) a single 5 MeV O^+ implantation. Note the difference in vertical scales and that the vacancy concentrations in the device region are similar. (from Elliman *et al.* [30])

for device isolation. There are several different sized devices ranging from 12 μm to 36 μm diameter emitters with optical access windows ranging from 4 μm to 20 μm . Figure 2.2 shows a close up of a single device with a 28 μm diameter emitter and a 12 μm diameter access window. Figure 2.2 also shows a diagram illustrating the fabrication process sequence.

Fabrication begins with the emitter mesa etch to etch down to the base layer. Since the base layer is thin, a very slow etch process must be used and electrical surface breakdown probing is used for endpoint detection. The *p*-ohmic base contacts are then evaporated and lifted-off using a positive photoresist process such as 1813+chlorobenzene. Next, the collector mesa etch is performed to etch down to the sub-collector layer. The emitter and base ohmic contacts are then evaporated and lifted-off using the same positive photoresist process. Device isolation is achieved with a final mesa etch down to the semi-insulating substrate. At this point, a thin passivation/isolation SiO_2 layer is deposited by plasma enhanced chemical vapor deposition (PECVD). This layer serves to isolate the device layers from the interconnect metalization. Via holes are etched through the SiO_2 layer using RIE. Finally, the devices are completed with the deposition of thick Ti/Al/Ti/Au for the interconnect metalization.

2.4 Transparent Contact HBT Fabrication

The "HBT2" mask set is used to make multi-fingered self aligned devices which allow light access through a transparent emitter contact. Device isolation is achieved using a high energy O^+ implantation step. Consequently, this mask set is limited for use with GaAs-based layer structures as implant isolation is ineffective for InGaAs based structures. Emitter contacts are made

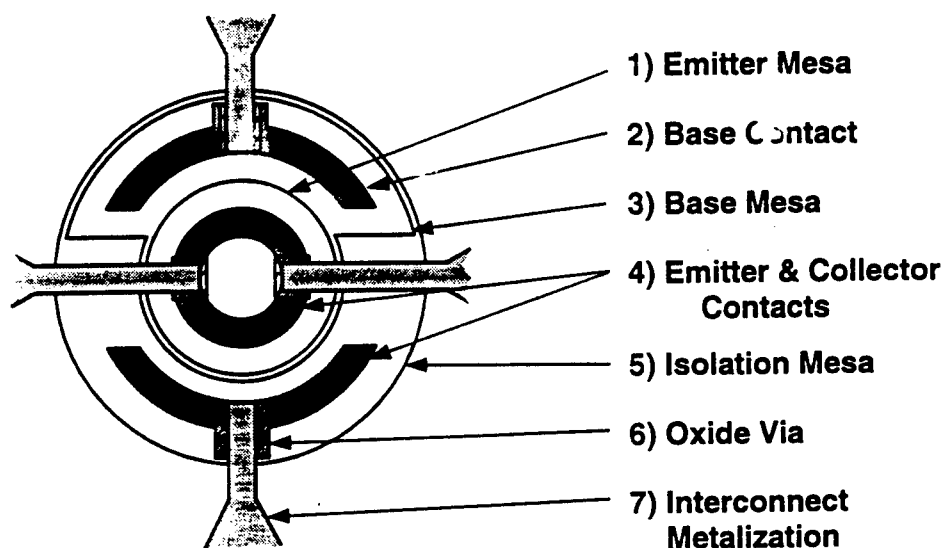
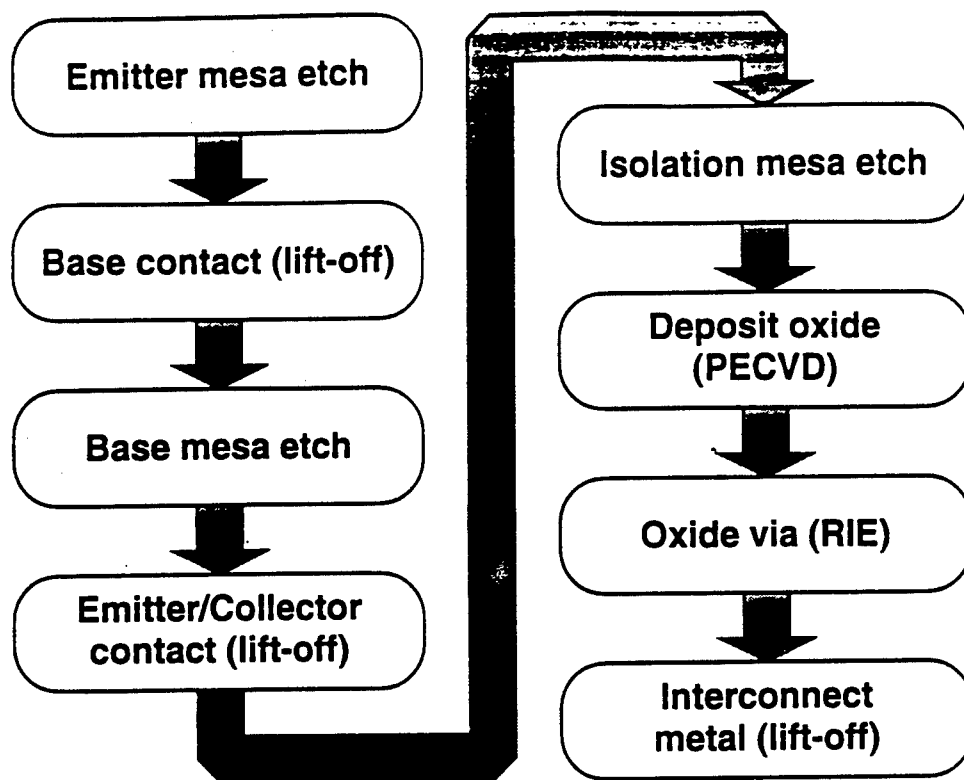


Figure 2.2: Fabrication sequence and device layout for the OPHBT mask set. The device shown here has an emitter diameter of $28\text{ }\mu\text{m}$ and an optical access window diameter of $12\text{ }\mu\text{m}$. Emitter area is over $600\text{ }\mu\text{m}^2$.

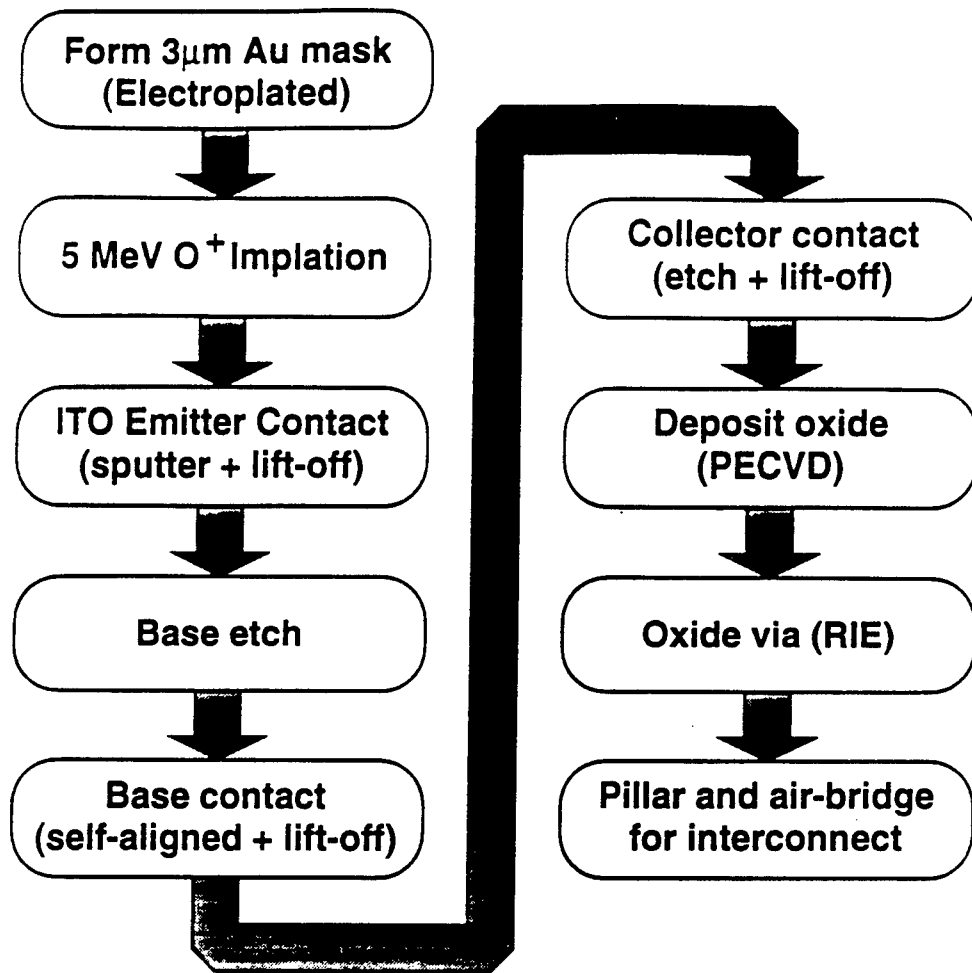


Figure 2.3: Fabrication sequence for ITO-HBT devices

using transparent indium-tin-oxide (ITO) which is described in detail in section 4.2.2. A diagram illustrating the fabrication process sequence is shown in Fig. 2.3 and the device layout is shown in Fig. 2.4.

Device isolation is achieved with a single dose high energy O^+ implantation (5 MeV , $O^+ = 1.7 \times 10^{15} \text{ cm}^{-2}$) using $3 \text{ } \mu\text{m}$ thick electro-plated Au masks and followed by an appropriate anneal (RTA at 560° C in Ar for 20 seconds). After defining the emitter contacts with patterned image-reversal photoresist, a 6 nm indium layer is deposited by evaporation. This is followed by a 250 nm

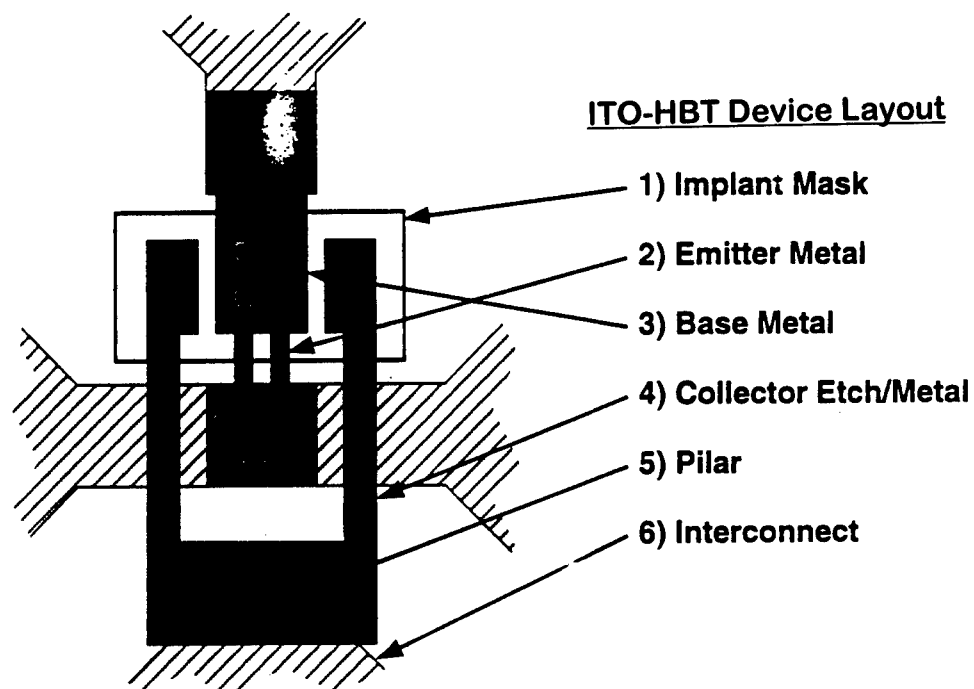


Figure 2.4: Mask set and layout for ITO-HBT device. The device shown here has two $2\mu\text{m} \times 10\mu\text{m}$ fingers for a total emitter area of $40\mu\text{m}^2$. Optical access is *through* the emitter contact which must use a transparent conductor as the contact material.

layer of ITO deposited by RF sputtering. Fabrication of the emitter contacts is accomplished using an acetone and ultrasound lift-off process. RTA annealing for 30 seconds at 450° C completes formation of the ITO ohmic contacts. A wet chemical etch using $\text{NH}_4\text{OH} : \text{H}_2\text{O}_2 : \text{H}_2\text{O}$ is performed to reach the base layer. The ITO emitter fingers are used as the etch mask. A Pd/Zn/Pd/Au ohmic contact is deposited by evaporation for the self-aligned base metalization. The emitter ITO is covered by photoresist to block metal deposition during this process. The Ni/Ge/Au/Ti/Au collector contacts are made using a similar etching and lift-off process. Finally, coplanar transmission line patterns suitable for microwave probing are defined, and connection to the devices was completed with an electroplated Au air-bridge.

2.5 Integrated Waveguide-HBT Fabrication

The waveguide-HBT mask setup makes conventional metal emitter HBTs with fully self aligned base contacts. Light access is achieved via a surface waveguide which is incorporated into layers beneath the device. This process can be used for fabricating either GaAs or InP based devices as device isolation is from a mesa etch instead of ion implantation. This process is also used with no modifications to fabricate the monolithic microwave integrated circuits (MMICs) described in Chap. V. A diagram illustrating the fabrication process sequence is shown in Fig. 2.5 and the device layout is shown in Fig. 2.6.

Fabrication of the InP-based devices described in Chap. V begins with the emitter contacts. The emitter is defined using an image-reversal photoresist mask with an undercut profile suitable for a lift-off process. Ti/Pt/Au (50/50/150 nm) ohmic contacts were deposited by electron beam evaporation

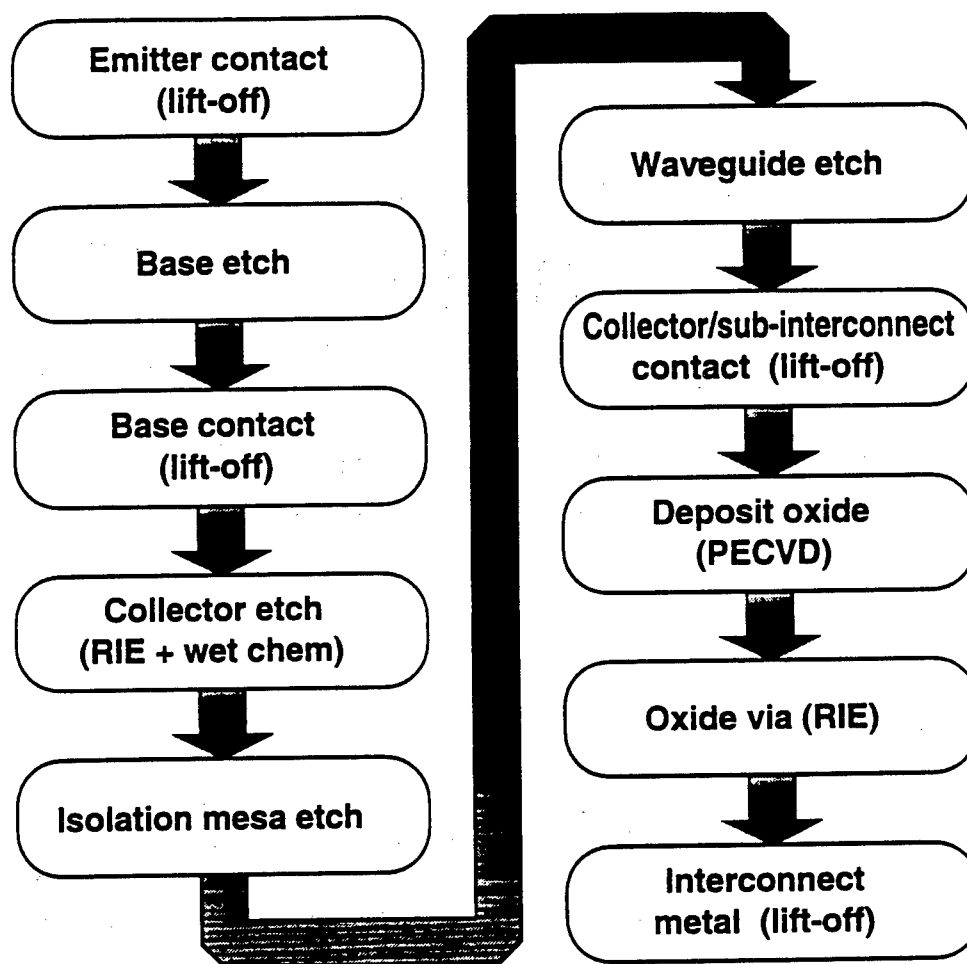


Figure 2.5: Fabrication sequence for waveguide-HBT devices

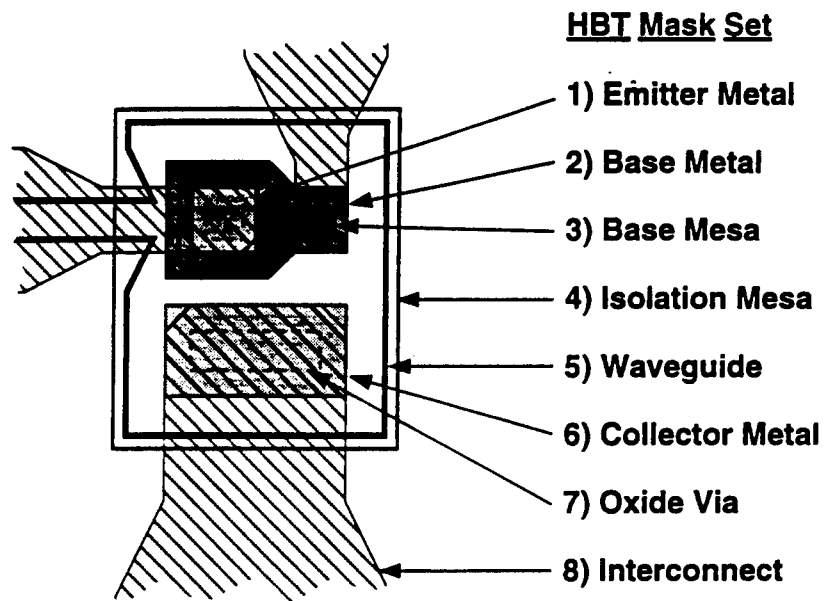


Figure 2.6: Mask steps and layout for waveguide-HBT device. The device shown here has a $5\mu\text{m} \times 5\mu\text{m}$ square emitter for a $25\mu\text{m}^2$ emitter area. Optical access is achieved through the surface waveguide which is incorporated into layers beneath the device.

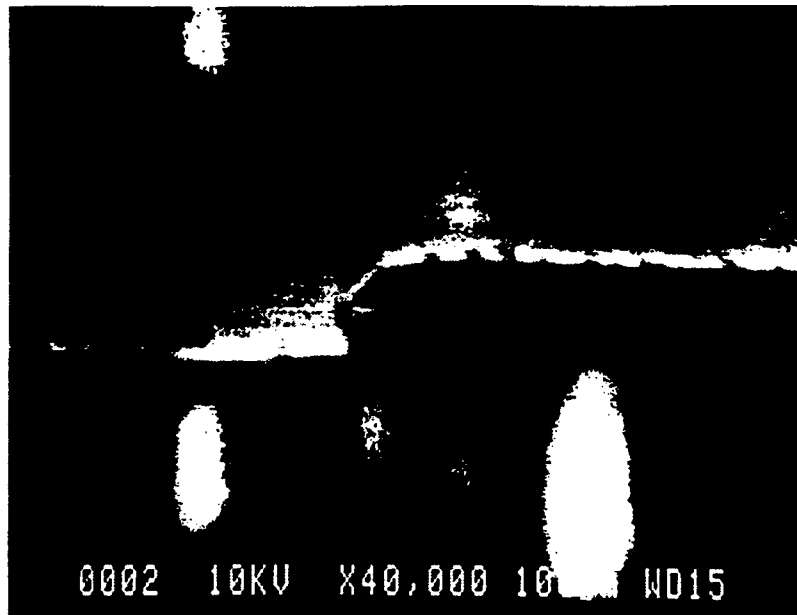


Figure 2.7: Scanning electron micrograph of etch profile for selective InAlAs etch. Two distinct slopes are clearly visible for the 100 nm InGaAs cap layer and the 150 nm InAlAs emitter.

and contact definition was completed using an acetone lift-off process. Using the emitter metalization as the etch mask, a selective etch process to reach the base layer was done in a three step wet chemical etch process. First, the 100 nm InGaAs contact layer and 50 nm of the InAlAs emitter were removed using a 80 second etch in $\text{H}_3\text{PO}_4:\text{H}_2\text{O}_2:\text{H}_2\text{O}$ (1:1:40). Then the etch to the base layer was completed using $\text{HCl}:\text{H}_2\text{O}$ (3:1) which etches InAlAs selectively over InGaAs [23]. This was followed by a very short InGaAs etch to remove the undoped spacer layer. A scanning electron micrograph of the etch profile is shown in Fig. 2.7. The necessary undercut profile is clearly evident where the InAlAs etch undercut the InGaAs layer.

A photoresist lift-off process was used to define the base ohmic contacts. Ti/Pt/Au/Ti (50/50/100/10 nm) was used for the self-aligned base metalization. The additional Ti layer is to protect the contact metals during a subsequent

RIE etch step.

After protecting the exposed base-emitter junction with photoresist, the base contact was used as the mask for the mesa etch through the collector. The 690 nm collector etch was completed in two steps: The first 500 nm was removed in a directional RIE etch and the remaining 190 nm using the $\text{H}_3\text{PO}_4:\text{H}_2\text{O}_2:\text{H}_2\text{O}$ wet chemical etchant. This method prevents excessive undercutting of the base contact metalization during the deep etch. The endpoint of the etch was determined using electrical probing to determine the surface breakdown voltage of the etched surface.

After depositing Ti/Pt/Au for the collector ohmic contact, the isolation mesa etch was performed to remove the sub-collector layer. The optical waveguide was then fabricated using a 0.8 μm deep wet chemical etch step. While the deep wet etch did result in undercutting of the 3 μm photoresist etch mask by about 0.5 μm , the resultant 2 μm waveguide still supports a guided mode. RIE etching is not effective for removing the InAlAs waveguide material.

Device processing was completed by depositing a 1 μm PECVD SiO_2 layer, performing the RIE oxide via etch, and deposition of the thick (2 μm) interconnect metalization.

2.6 Waveguide Modulator Fabrication

The Laser-Modulator process creates a single mode ridge waveguide structure with high frequency electrical contacts to both a top contact layer and a buried contact layer. This is important for high speed devices grown on semi-insulating substrates where a backside contact is not available. The contact pads are suitable for microwave probing with a 200 μm pitch "ground-signal"

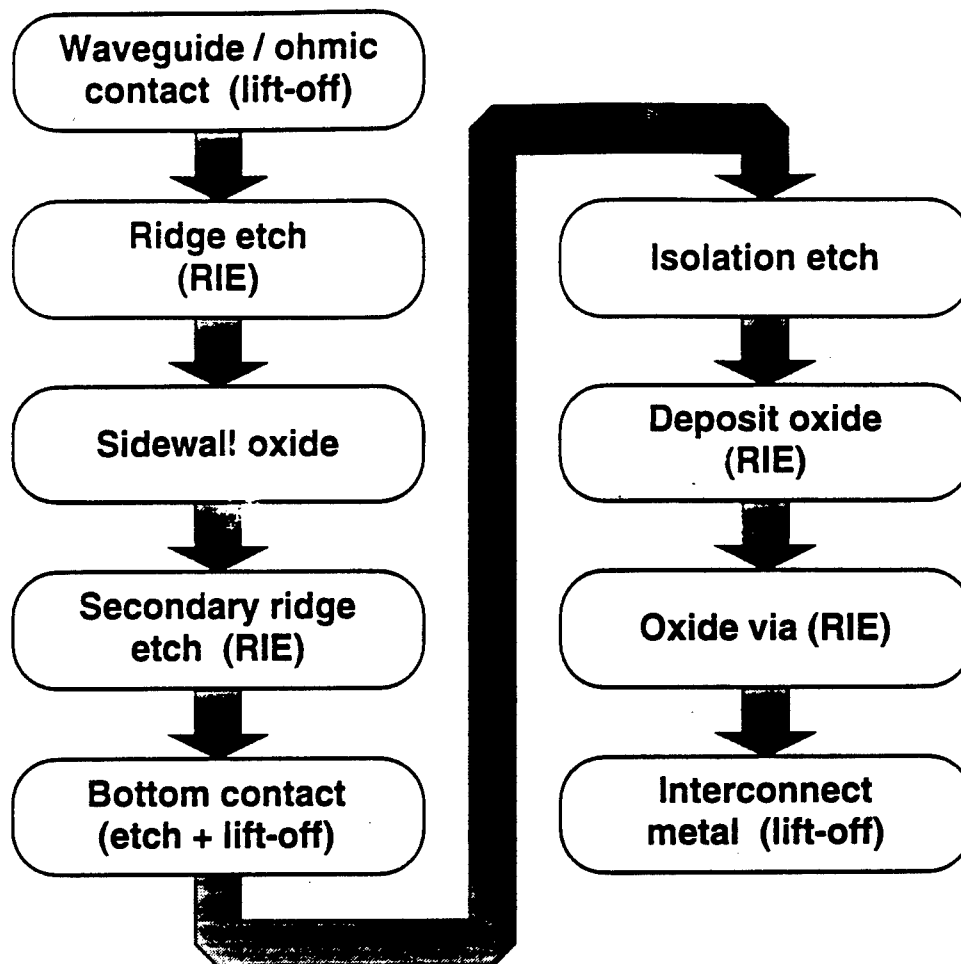


Figure 2.8: Fabrication sequence for waveguide modulator

probe. This mask set is effectively used for fabrication of either semiconductor lasers or optical waveguide modulators. The ridge width is $3\ \mu\text{m}$. The total active device width is $20\ \mu\text{m}$ with a standard process or $5\ \mu\text{m}$ with the double-ridge process. A diagram illustrating the fabrication process sequence is shown in Fig. 2.8 and the device layout is shown in Fig. 2.9.

The fabrication of a GaAs-based modulator proceeds as follows: First, the top ohmic contact is deposited, patterned and annealed. Ni/Ge/Au/Ti/Au/Ti is used as the top contact. The additional Ti layer serves to protect the Au

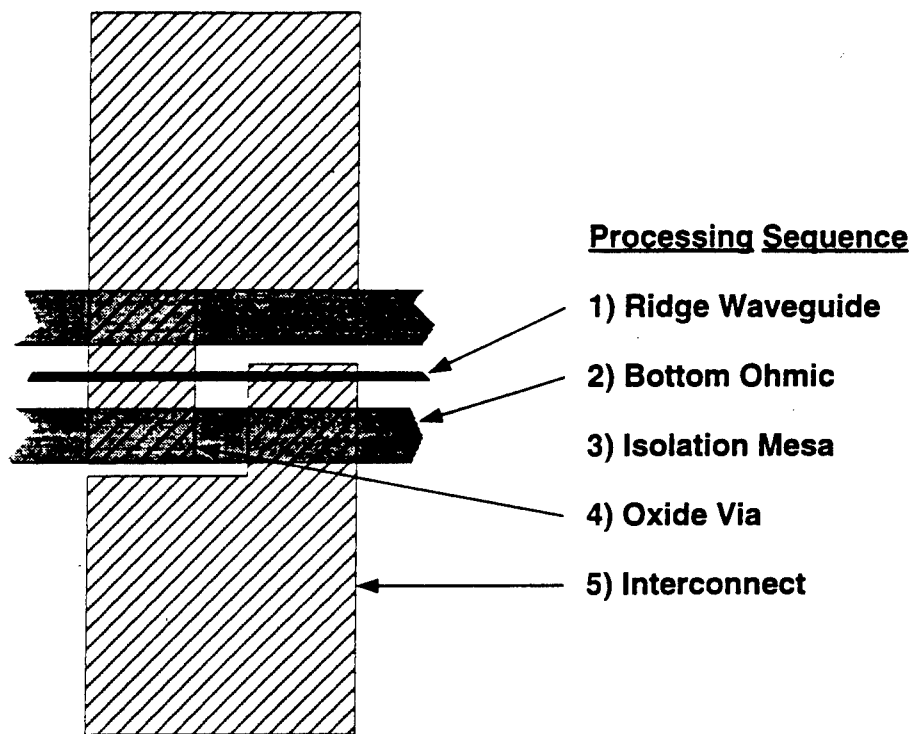


Figure 2.9: Mask steps and layout for waveguide modulator. The ridge width is $3\text{ }\mu\text{m}$. The total active device width is $20\text{ }\mu\text{m}$ with a standard process or $5\text{ }\mu\text{m}$ with the double-ridge process.

layer during the subsequent RIE etch processes. A $0.5\text{ }\mu\text{m}$ ridge etch is then performed using a combination of RIE and wet chemical etching with the n -ohmic contact serving as the etch mask. Then a thick sidewall oxide mask is formed by deposition of $1\text{ }\mu\text{m}$ thick conformal PECVD oxide followed by a directional RIE etch. This leaves $1\text{ }\mu\text{m}$ oxide sidewalls which are then used as a mask in the secondary ridge etch. RIE is used for the deep secondary ridge etch. This etch goes through the active device layers and stops in the lower cladding layer. The secondary ridge etch is optional. A wet chemical etch to the bottom contact layer is performed next using a photoresist etch mask which doubles as the lift-off mask for the deposition of the bottom n -ohmic contact. After performing an isolation mesa etch, a $1\text{ }\mu\text{m}$ thick PECVD SiO_2 pad oxide is deposited. Device processing is then completed with an RIE oxide via etch and deposition of thick metal interconnect pads.

CHAPTER III

PROPERTIES OF HETEROJUNCTION BIPOLAR TRANSISTORS WITH MULTI-QUANTUM WELL COLLECTOR REGIONS

3.1 Introduction

This chapter presents work on the study of a novel device — a heterojunction bipolar transistor (HBT) with a multi-quantum well (MQW) region incorporated into the undoped collector region. In dark conditions, the MQW-HBT has the same characteristics as a standard HBT. However, with optical excitation near the GaAs band-gap energy, these devices have the potential for generating optically induced oscillations without the need for the electrical feedback network commonly required for microwave oscillators. The theoretical basis for this phenomena and some experimental results of our work on the MQW oscillators are presented below.

3.2 Oscillations From MQW Devices

3.2.1 The Quantum Confined Stark Effect

The absorption spectrum of a quantum well is greatly modified in the presence of a transverse electric field. In particular, the intersubband transition energy and excitonic binding energy are reduced with the application of an electric field. Figure 3.1 shows the basic effects responsible for the quantum confined Stark effect (QCSE). As can be seen, when an electric field is applied, the intersubband transition energy is reduced due to a shift from parallel square wells to offset triangular wells. This shift has a strong effect on the excitonic transition energy \mathcal{E}_{ph} , which can be represented as [35]

$$\mathcal{E}_{ph} = \mathcal{E}_{gw} + \mathcal{E}_e + \mathcal{E}_h - \mathcal{E}_{ex} , \quad (3.1)$$

where \mathcal{E}_{gw} is the bandgap in the well region, \mathcal{E}_e and \mathcal{E}_h are the electron and hole subband energies, and \mathcal{E}_{ex} is the excitonic binding energy. With the application of moderate electric fields, several of the components of Eqn. 3.1 are affected. There is a small change in \mathcal{E}_{gw} due to the Stark effect in the well material. Due to the modification of the envelope functions, there is a significant reduction in the subband energies \mathcal{E}_e and \mathcal{E}_h . This results in a shift of the absorption spectrum to lower energies. Both the heavy hole and light hole resonances experience the shift. In addition to this effect, the excitonic binding energy, \mathcal{E}_{ex} , is slightly reduced due to the separation of the electron and hole wavefunctions. However, the QCSE is primarily characterized by the intersubband effect as the change in excitonic binding energy is an order of magnitude smaller [36].

Figure 3.2 shows the tunability in the absorption spectrum as the applied electric field is increased. The large peak is due to the heavy-hole (HH) to first

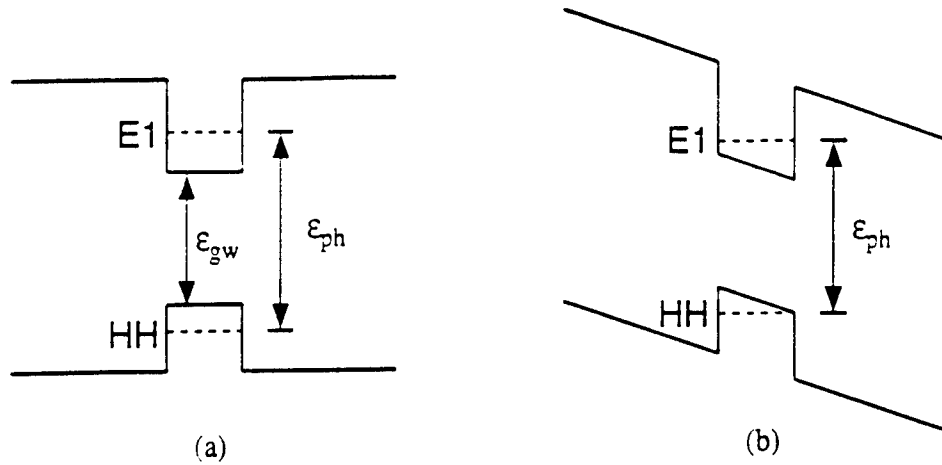


Figure 3.1: Bandstructure of quantum wells illustrating the quantum confined Stark effect: (a) Shows quantum well and transition energy under equilibrium condition. (b) Under an applied electric field the confined excitonic transition energy is reduced.

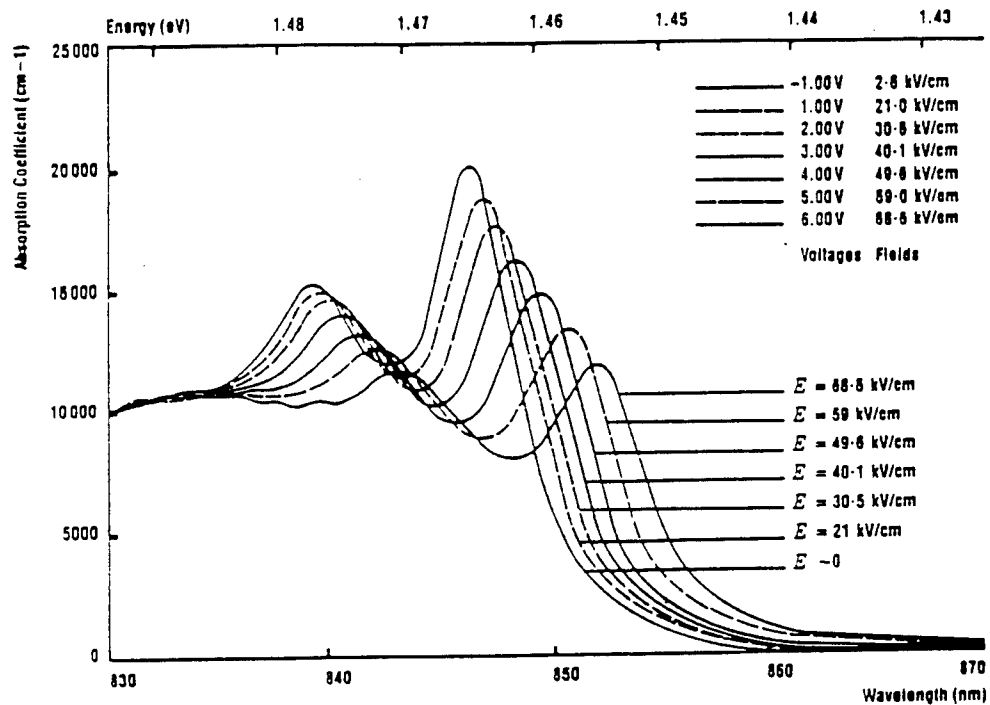


Figure 3.2: Absorption spectra at various electric fields for a 50 period $\text{Al}_{0.32}\text{Ga}_{0.68}\text{As} / \text{GaAs}$ MQW structure with 10.5 nm wells and 9.5 nm barriers. (from Lengyel *et al.* [34])

electron state (E1) excitonic absorption in the quantum well. The secondary peak arises from the light-hole (LH) to E1 exciton. The shift in the absorption peak has a quadratic dependence on applied field [37] which is represented by [36]

$$E_1 = \frac{1}{24\pi} \left(\frac{15}{\pi^2} - 1 \right) \frac{m^* \epsilon^2 E^2 W^4}{\hbar^2}, \quad (3.2)$$

where E is the applied electric field and W is the width of the quantum well. The tuning effect combined with the large peak in the room-temperature absorption spectrum is what makes the QCSE so useful. Note that this effect can be enhanced by including multiple quantum-wells (MQW) in the same device.

If a fixed wavelength of light is used, increasing the electric field across the quantum well will have the effect of “scanning” the shifting absorption spectrum across the single frequency. The absorption vs. applied field relationship would exhibit a similar profile to the curves in Fig. 3.2. Most importantly, if the absorption takes place in a photodetector or phototransistor, there will be at least one range of electric field values where the photocurrent decreases as the applied field is increased, or

$$\frac{\delta V_{\text{applied}}}{\delta I_{\text{photo}}} < 0. \quad (3.3)$$

At this bias point, the device exhibits negative differential resistance (NDR). Therefore, small signal voltage excitations applied to this device will be amplified. While this NDR effect would cause undesirable instabilities in amplifiers, it has been utilized to create novel optoelectronic logic [38] and memory [39] devices. It is also potentially useful for building oscillators [40].

3.2.2 NDR Oscillator

In a standard series RLC circuit configuration, the total impedance of the circuit as a function of frequency is expressed as

$$Z(j\omega) = R + j\omega L + \frac{1}{j\omega C} . \quad (3.4)$$

At the frequency

$$\omega_o = \frac{1}{\sqrt{LC}} , \quad (3.5)$$

the imaginary component of $Z(j\omega)$ goes to zero and the loop is said to be in *resonance*. The time evolution of an underdamped RLC circuit after excitation at frequency ω_o is expressed by

$$v(t) = Ae^{-\alpha t} \cos \omega_o t , \quad (3.6)$$

where α is called the damping coefficient and is defined as $\alpha = \frac{R}{2L}$. Equation 3.6 describes an system with exponentially decreasing oscillations where the damping is proportional to the series resistance R of the RLC loop.

If the device exhibiting NDR was incorporated into a series RLC circuit, the damping coefficient α would become negative. Under these conditions, Eqn. 3.6 describes a circuit where oscillation *build up* with time instead of experiencing damping. Since a real system cannot support an exponential increase for very long, device non-linearities will quickly slow the exponential growth and the system will reach a condition of steady state oscillation. This is the basis for the NDR oscillator. Since the NDR effect in MQW devices is optically induced, oscillators exploiting this effect could be switched on and off by switching the excitation light source on and off.

3.3 Multiple-Quantum-Well HBT

To properly take advantage of the quantum confined Stark effect, control over the electric field strength across the quantum wells must be achieved. In a bipolar junction transistor, the strongest electric fields are found in the base-collector depletion region due to the 2–8 V reverse bias applied across the junction in normal operation. The magnitude of this field is easily controlled by changing the collector bias voltage while the transistor is in forward active mode. In light of these considerations, an MQW-HBT structure was designed with the multiple quantum well region in the collector. The collector region was left undoped to ensure that all the quantum wells will be in the base-collector depletion region where photo-generation of carriers will have the largest effect on device operation. Photo-generated holes from photon absorption in the quantum wells will be swept into the base by the high electric field and have the effect of adding to the base current. This photocurrent will then be amplified by transistor action which will lead to greater QCSE effects than would be achieved in a simple *p-i-n* diode structure.

3.3.1 Device Fabrication

The MQW-HBT structure shown in Table 3.1 was grown by molecular beam epitaxy. The “OPHBT” device process described in section 2.3 was used to fabricate the transistors. Wet chemical etching was employed for the emitter, base, and isolation mesa etches. A Ni/Ge/Au/Ti/Au metalization scheme with thicknesses of 25/32.5/65/20/200 nm was deposited by evaporation for the emitter and collector *n*-ohmic contacts. For the *p*-ohmic contacts, an evaporated metalization of Pd/Zn/Pd/Au (10/10/20/100 nm) was used. A hot-plate anneal for

Layer	Composition	Thickness	Doping (cm^{-3})
Cap	GaAs	20 nm	$n = 5 \times 10^{18}$
Emitter	$\text{Al}_{.3}\text{Ga}_{.7}\text{As}$	250 nm	$n = 5 \times 10^{17}$
Base	$\text{Al}_x\text{Ga}_{1-x}\text{As}$ ($x=0.1-0.0$)	100 nm	$p = 1 \times 10^{19}$
Transition	GaAs	60 nm	$n = 5 \times 10^{16}$
MQW Collector	GaAs	9 nm	undoped
20 periods	$\text{Al}_{.2}\text{Ga}_{.8}\text{As}$	8 nm	undoped
Subcollector	GaAs	500 nm	$n = 5 \times 10^{18}$
Substrate	GaAs		semi-insulating

Table 3.1: Layer structure of MQW-HBT

40 seconds at 400° C was used to complete the formation of the ohmic contacts. A SiO_2 layer was deposited by PECVD and oxide via holes were etched using an RIE etch process. Device fabrication was completed with the deposition of a thick Ti/Al/Ti/Au (50/800/50/200 nm) interconnect metalization.

3.3.2 MQW-HBT Performance

DC Characteristics

At DC bias conditions, current-voltage relationships were measured for both dark and illuminated conditions. A temperature tunable AlGaAs laser diode (SDL-5412) operating between 840 nm and 860 nm was used as the light source. Light access to the fabricated devices was through the 4 μm diameter hole in the center of the emitter contact metalization. The incident power on the device was about 300 μW . Current/voltage measurements of the

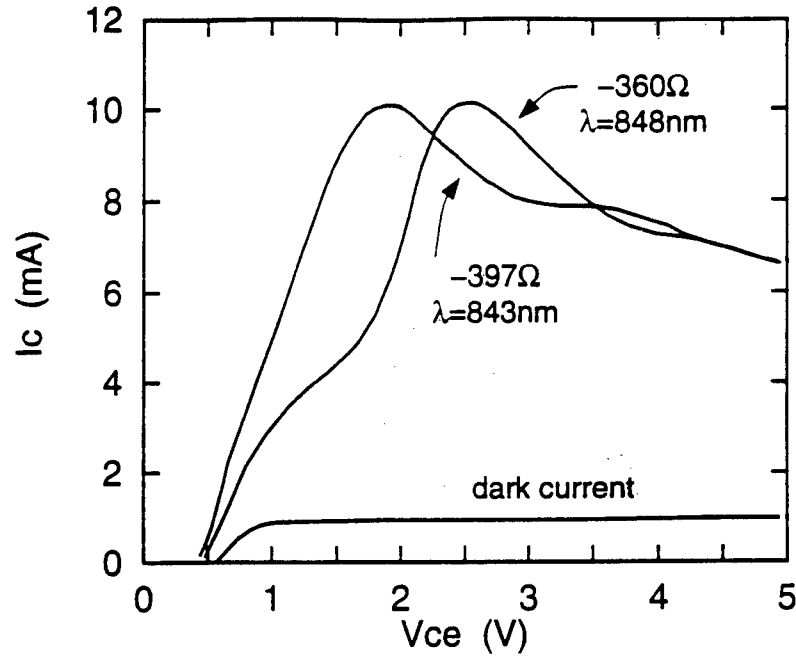


Figure 3.3: Current-Voltage relationship of MQW-HBT showing a strong negative differential resistance effect. The external base current is $50 \mu\text{A}$ and the incident optical intensity is about $300 \mu\text{W}$.

illuminated transistors clearly show the characteristic excitonic peaking and NDR due to the QCSE. As expected, the optically induced peak in the I-V curve was shown to shift as the wavelength of the light was varied. Figure 3.3 shows I-V curves for two different wavelengths of light illumination along with a dark curve. The maximum NDR observed was -397 at $\lambda = 843 \text{ nm}$.

Optical Impulse Response

To investigate the photoresponse of the MQW-HBTs, short optical excitation pulses from a mode-locked dye laser ($\lambda = 853 \text{ nm}$) pumped with a Nd:YAG laser were used. The nominal pulse width of the dye laser pulses was 7 ps with a repetition rate of 76 MHz . The response of the phototransistor showed a full width at half maximum (FWHM) of $\tau = 60 \text{ ps}$, as shown in Fig. 3.4. This

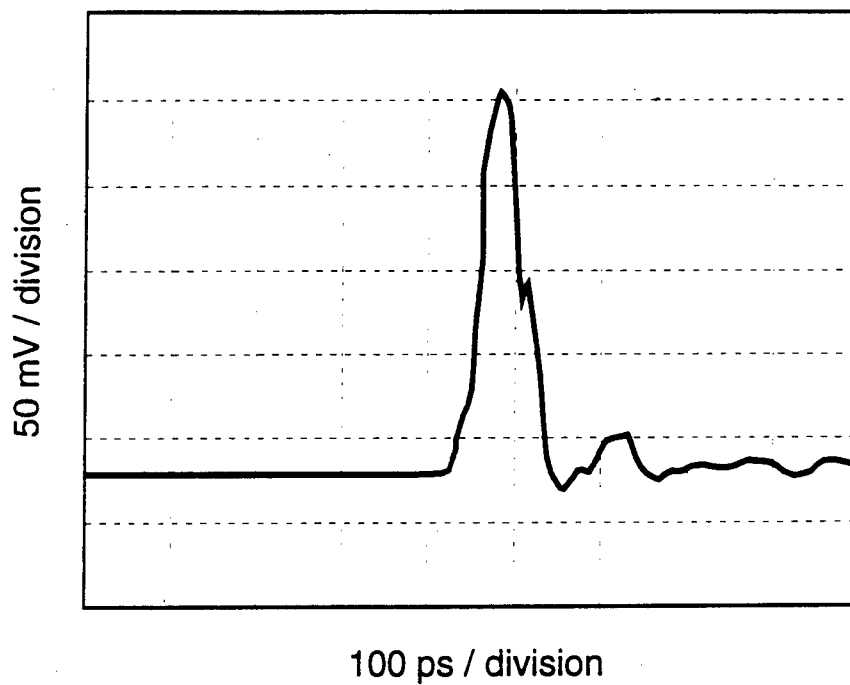


Figure 3.4: Optical impulse response of MQW-HBT. The detected response shows a *FWHM* of 60 ps. The deconvolved impulse response is 48 ps.

measurement is somewhat broadened due to the 7 ps optical pulse width and the 35 ps impulse response of the sampling head of the oscilloscope. The actual device response can be extracted using Eqn. A.19, (see App. A)

$$\tau_{\text{device}} = \sqrt{\tau_{\text{meas}}^2 - \tau_{\text{pulse}}^2 - \tau_{\text{head}}^2}, \quad (3.7)$$

$$\tau_{\text{device}} = \sqrt{(60\text{ps})^2 - (9\text{ps})^2 - (35\text{ps})^2}, \quad (3.8)$$

$$\tau_{\text{device}} = 48\text{ps}. \quad (3.9)$$

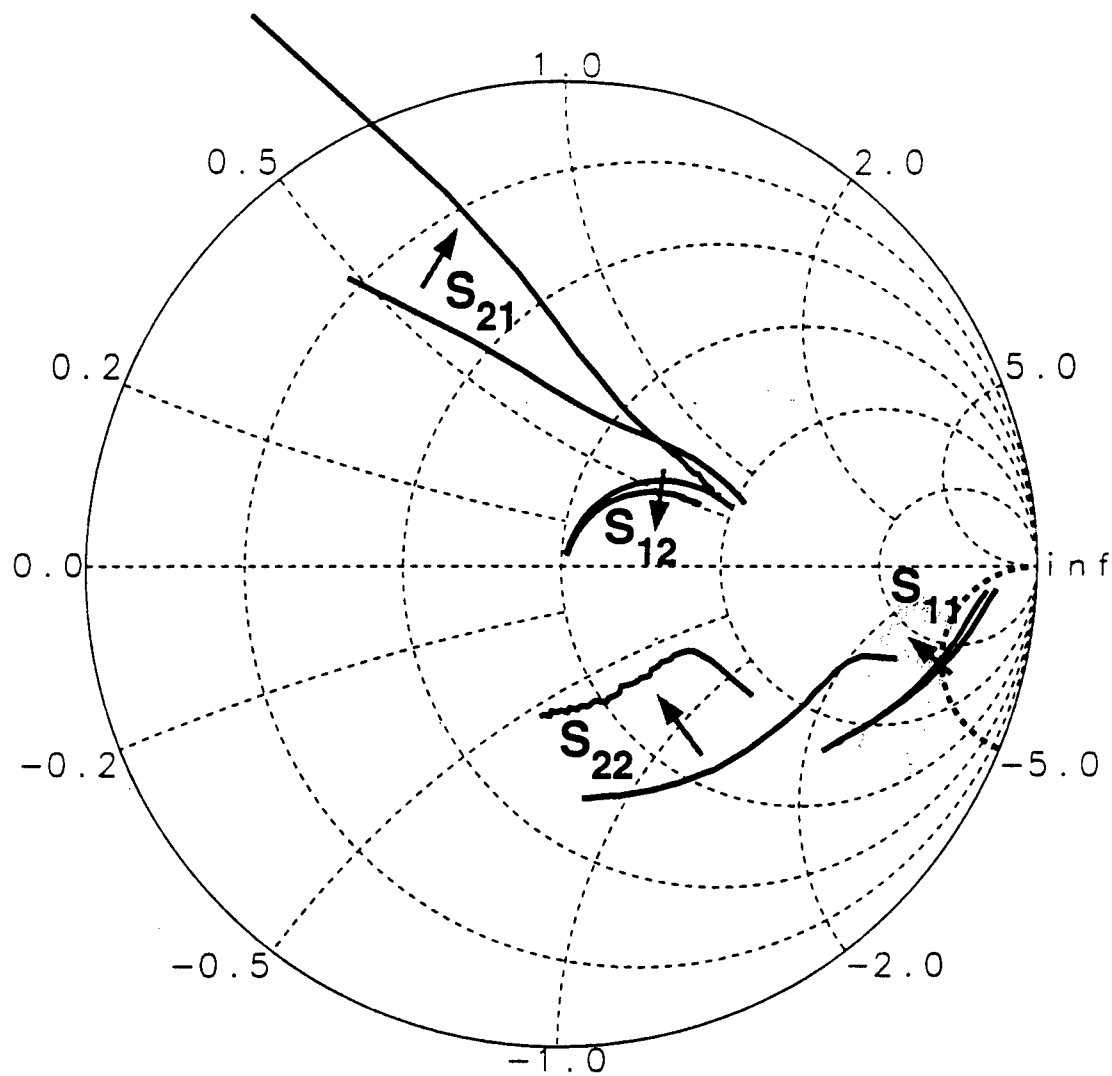
From the deconvolved *FWHM* of 48 ps, Eqn. A.25 is used to estimate the cutoff frequency:

$$f_{3\text{dB}} = \frac{2 \ln 2}{\pi} (48 \text{ ps})^{-1}, \quad (3.10)$$

$$f_{3\text{dB}} = 9.2 \text{ GHz}. \quad (3.11)$$

RF Characteristics

For microwave characterization of the fabricated MQW-HBT devices, an HP 8510 Network Analyzer connected to a Cascade probe station was used for on-wafer scattering parameter (S-parameter) measurements. Light from the tunable AlGaAs laser diode was delivered to the device via a single mode optical fiber and positioned using a Cascade fiber optic probe. The optical power incident on the device was again about 300 μW . The S-parameters of the HBT in common-emitter configuration were measured from 45 MHz to 8 GHz at fixed base and collector bias conditions ($I_B = 80 \mu\text{A}$ and $V_{CE} = 2.5 \text{ V}$). This bias point corresponds to the center of the NDR region on The collector current I_C was measured to be 1.3 mA and 4.5 mA under dark and illuminated conditions respectively. the I-V curve. The measured S-parameters with and without light are shown in Fig. 3.5.



Frequency 0.25 to 8.0 GHz

Figure 3.5: S-parameters of MQW-HBT under both illuminated and dark conditions. The transistor was biased at $V_{CE} = 2.5$ V and $I_B = 80$ μ A. Collector currents were 1.3 mA and 4.5 mA under dark and illuminated conditions respectively. The arrows show the direction the curves moved with the application of light. High frequency NDR would be indicated by S_{22} being outside the unit circle.

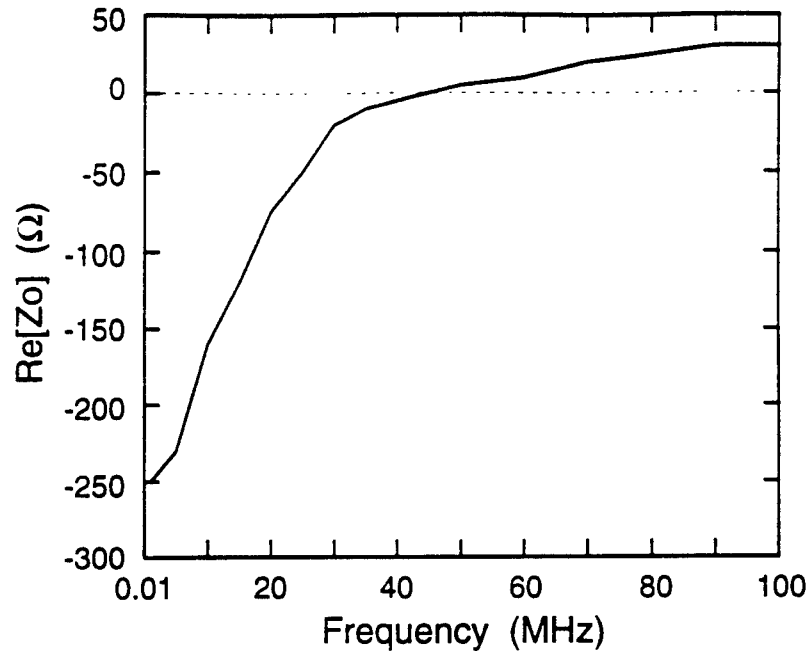


Figure 3.6: Low frequency impedance measurements of MQW-HBT. The quenching of NDR at about 45 MHz is clearly seen.

Although optical absorption has a significant effect on the S-parameters, the measurements show that NDR is not present for all tested frequencies. NDR would be indicated by the parameter S_{22} having a magnitude greater than 1. This would put it outside the boundary of the unit circle on the Smith chart.

To verify that this measurement was not in error, the HBT was tested with an HP 4194A Impedance/Gain Phase Analyzer at the same bias and illumination conditions, but over a lower frequency range. Figure 3.6 shows the real part of the output impedance from 10 KHz to 100 MHz. This measurement shows that NDR is indeed present at low frequencies as observed in the I-V measurements. However, at about 45 MHz the real part of the output impedance becomes positive. A microwave oscillator based on NDR will not be

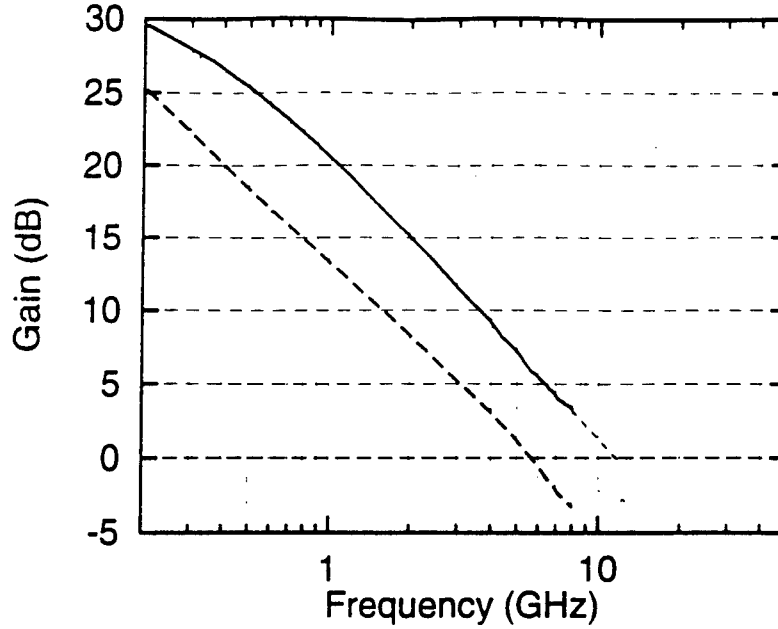


Figure 3.7: Measured current gain h_{21} (—) and power gain G_{max} (- - -) of MQW-HBT. At bias conditions $I_C = 2.3$ mA and $V_{CE} = 5.5$ V, the current gain cutoff frequency (f_T) and maximum frequency of oscillation (f_{max}) were found to be 11.7 GHz and 5.8 GHz respectively.

possible using this device.

3.4 Optical Control of Conventional HBT Oscillators

Although NDR is not present at microwave frequencies, the MQW-HBT is still functional as a heterojunction phototransistor (HPT) [41]. For a 20 μm emitter diameter HBT with a 4 μm optical access window, the short circuit current gain (h_{21}) and the maximum available power gain (G_{max}) were computed from S-parameter measurements and are shown in Fig. 3.7. With a current gain cut-off frequency (f_T) of 11.7 GHz and a maximum frequency of oscillation (f_{max}) of 5.8 GHz, the transistor can be used for making a low GHz optically controlled oscillator using a conventional feedback arrangement [42].

3.4.1 Oscillator Design

To design a conventional oscillator, the optical NDR feature that would be so helpful must be disregarded. A feedback network must be devised to induce NDR at the output terminal.

To design the feedback network, the program *Libra* by the software company EEsof was employed. The S-parameters measured for the HBT were used as input to a computer model which simulated the connection of two passive reactive elements to the base and emitter terminals. The collector terminal was specified as the output terminal. The two element values were then modified to optimally fit the following conditions: [43]

$$Re [Z_o] < -1.2R_L , \quad (3.12)$$

$$\left| \frac{\delta Re [Z_o]}{\delta Z_{ij}} \right| \rightarrow small , \quad (3.13)$$

$$\left| \frac{\delta Im [Z_o]}{\delta Z_{ij}} \right| \rightarrow small , \quad (3.14)$$

and

$$\frac{\delta Im [Z_o]}{\delta \omega} \rightarrow LARGE . \quad (3.15)$$

Equation 3.12 ensures that the feedback induced NDR is sufficient to ensure startup oscillations with the applied load R_L (commonly $R_L = 50$). For the oscillators designed, $Re [Z_o]$ was set to values less than -70 to allow for compensation of additional losses in the fabricated circuit. Equations 3.13 and 3.14 ensure that feedback from the load doesn't effect the free-running oscillation frequency. Equation 3.15 optimizes for highest Q factor. Once these optimization have been performed, we have a network that can be made into an oscillator with the addition of a simple impedance matching network.

After designing an oscillator for operation at 3 GHz, the optimal component values determined by the *Libra* simulation were converted into microstrip elements so that the circuit could be fabricated. The dimensions of the microstrip elements were determined using *Libra* and a microstrip circuit mask was created using the program *PUFF* [44]. The mask was printed directly onto transparency film using a standard personal computer laser printer (HP LaserJet IIP). After transferring the pattern to a photoresist etch mask, the circuit was etched into an 1 mm epoxy microstrip board and the HBT was wire-bonded into the circuit.

To test the microstrip oscillator, the circuit was biased externally through bias tees at the same bias condition as used for the original S-parameter measurements. The same AlGaAs laser diode was used to illuminate the HBT through an optical fiber. A spectrum analyzer was then hooked up to the oscillator circuit's output to check for oscillations. With the HBT biased at $V_{CE} = 5$ V and $I_C = 4.5$ mA, oscillations were observed at 2.65 GHz. The output power level was measured to be -5 dBm ($320 \mu\text{W}$).

3.4.2 Direct Optical Injection Locking

To perform optical injection locking experiments, amplified RF power from a sweep generator was superimposed over the DC bias current of a Sharp LT015MF0 AlGaAs laser diode to produce high-frequency modulated light. The output wavelength of the laser was 830 nm. The modulated light was focused directly onto the HBT emitter window. The oscillator output was monitored on a spectrum analyzer.

When the oscillator was unlocked but the frequency of the injected signal

(f_{inj}) was close to the oscillating frequency (f_{osc}), the oscillator output spectra contained many sidebands as shown in Fig. 3.8. This is the same effect that is observed in microwave injection locking, which has been theoretically explained by Armand [45]. Once f_{inj} was tuned to within the locking range, the side bands disappeared and the phase noise in the output spectrum reduced markedly as the oscillation frequency locked itself to the injected signal. After the oscillator locks to the injected signal, the oscillation frequency will follow f_{inj} as long as it stays within the locking bandwidth. Figure 3.9 shows the output spectrum of the direct optically injection locked oscillator at both limits of the injection locking range. The maximum injection locking bandwidth was found to be 5.6 MHz. The injection locking range as a function of the RF generator power used to drive the laser diode is shown in Fig. 3.10 along with a similar curve from a microwave injection locking experiment performed on the same oscillator. In both cases, the locking range (ω_{max}) follows the predicted square root dependence of Eqn. 1.1 which is repeated here for clarity.

$$\omega_{max} = \frac{\omega_o}{2Q} \sqrt{\frac{P_{inj}}{P_0}}, \quad (3.16)$$

where ω_o is the free running oscillation frequency. P_{inj} and P_0 are the injected power and oscillator output power.

The quality factor, Q , of the oscillator can then be estimated by noting that a locking range of 4.3 MHz was observed when the microwave injection locking power was $15.5 \mu\text{W}$. The output power of the oscillator during this experiment was $100 \mu\text{W}$ so we determine Q as follows:

$$4.3 \text{ MHz} = \frac{2.65 \text{ GHz}}{2Q} \sqrt{\frac{15.5 \mu\text{W}}{100 \mu\text{W}}} \quad (3.17)$$

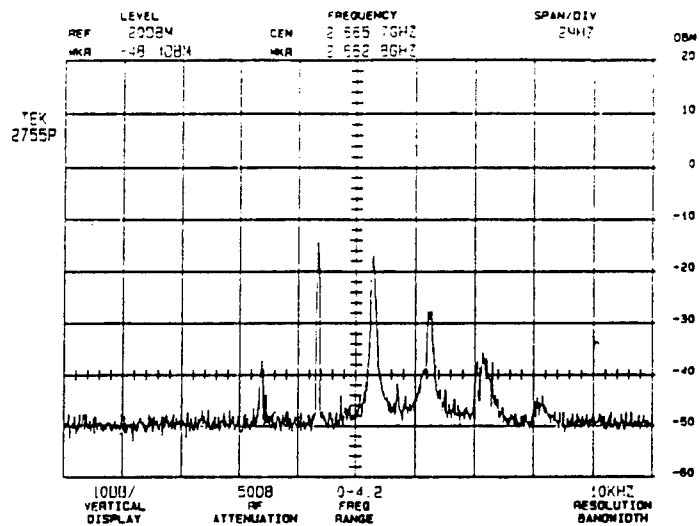


Figure 3.8: Output spectrum of unlocked HBT oscillator showing multiple sidebands

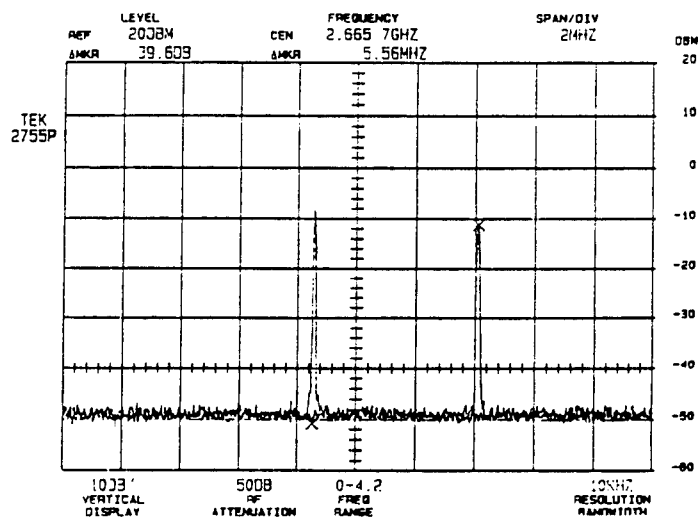


Figure 3.9: Output spectrum of direct optically injection locked HBT oscillator at both limits of the injection locking range. The injection locking bandwidth is 5.6 MHz.

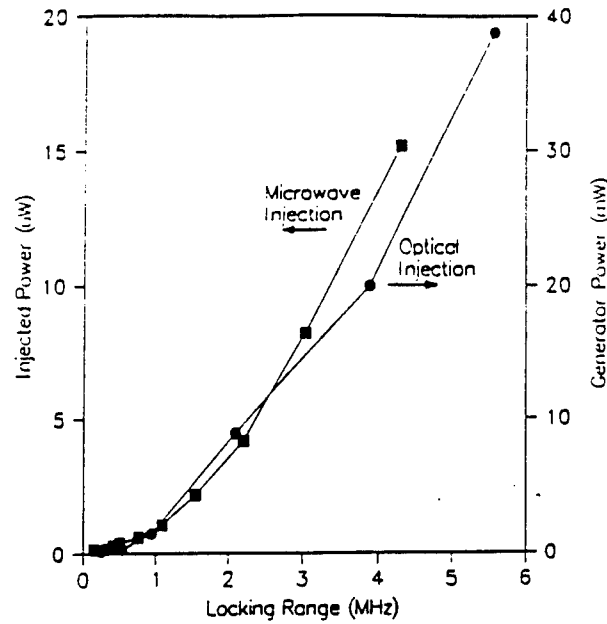


Figure 3.10: Microwave and optical injection locking ranges as a function of generator power

and, therefore,

$$Q = 121. \quad (3.18)$$

3.4.3 Optical Tuning

By varying the DC bias current of the laser, the optical illumination intensity was varied. It was observed that increasing the optical intensity caused an increase in the oscillation frequency. A frequency tuning range of 5 MHz was observed. This effect is explored further in Chapter IV.

3.5 NDR Response in a p-i(MQW)-n Diode

Since previous studies [40] indicated that the NDR effect should be able to produce oscillators at frequencies much higher than 45 MHz, further study of this structure was required. The investigated HBT was a N-p-n device.

Because of this, transistor action is controlled by the flow of holes in the device. Since the photo-generated holes have low mobility as compared to electrons, the speed of hole escape from the wells and transit to the base layer is possibly limiting the NDR response.

In theory, a P-n-p MQW-HBT device should avoid this problem because photo-generated electrons will be used as the control charges. Since the electron mobility in GaAs is about 20 times larger than the hole mobility, a twenty-fold increase in NDR response may be possible. However, this may not be realizable in practice because the P-n-p HBT relies on the injection of the slower holes into the collector and their subsequent transfer across the base-collector depletion region. Therefore, transit time limited effects can be expected to be degraded in this structure. The competition between these two effects will serve to confuse the analysis. It would be better to first study the NDR behavior of the MQW region in the absence of the extra complexity of the HBT structure.

To this effect, a p-*i*(MQW)-n diode structure was designed and tested. As shown in Table 3.2, the diode has a 30 period $\text{Al}_{0.2}\text{Ga}_{0.8}\text{As}/\text{GaAs}$ multi-quantum well region with 10 nm wells and 8 nm barriers. The total thickness of the *i* region is 0.54 μm . The device was fabricated using the same OPHBT mask set as for the MQW-HBT, with the exception that the mesa etch for device isolation was performed during the collector etch step and the mesa-isolation mask was never used. Consequently, the metalization for the collector contact was deposited on the substrate.

To study the NDR behavior of the p-*i*(MQW)-n diode, 850 nm light from an AlGaAs diode laser was coupled into the device via the Cascade fiber op-

Table 3.2: Layer structure of the p-i(MQW)-n photodiode

Layer	Composition	Thickness	Doping (cm^{-3})
p-contact	$\text{Al}_{0.05}\text{Ga}_{0.95}\text{As}$	100nm	$p = 2 \times 10^{18}$
	$\text{Al}_x\text{Ga}_{1-x}\text{As}$	50nm	$n = 5 \times 10^{16}$
MQW i-region	GaAs	10nm	undoped
30 periods	$\text{Al}_{0.2}\text{Ga}_{0.8}\text{As}$	8nm	undoped
	$\text{Al}_x\text{Ga}_{1-x}\text{As}$	30nm	$n = 1 \times 10^{18}$
n-contact	GaAs	300nm	$n = 1 \times 10^{18}$

tic probe. As shown in Fig. 3.11, the current/voltage relationship of the p-i(MQW)-n shows the expected NDR response. The maximum NDR was found to be -6427 . This is a factor of 20 higher than the NDR observed with the MQW-HBT. This is the expected result as the current gain of $h_{fe} = 20$ will increase the *negative differential conductance* by a factor of 20 when the MQW is incorporated into the HBT structure.

To study the high-frequency NDR behavior of the p-i(MQW)-n diode, the HP 8510 Network Analyzer was again employed. The diode was biased at 4 V corresponding to the condition of maximum NDR. One-port S-parameter measurements were then performed from 50 MHz to 10 GHz.. The plot of the measured data is shown in Fig. 3.12. No high-frequency NDR is observed since the S_{11} reflection coefficient is inside the unit circle for the entire range of the measurement.

This result suggests that the quenching of the NDR at high frequencies in the MQW-HBT structure was not due to problems arising from the HBT

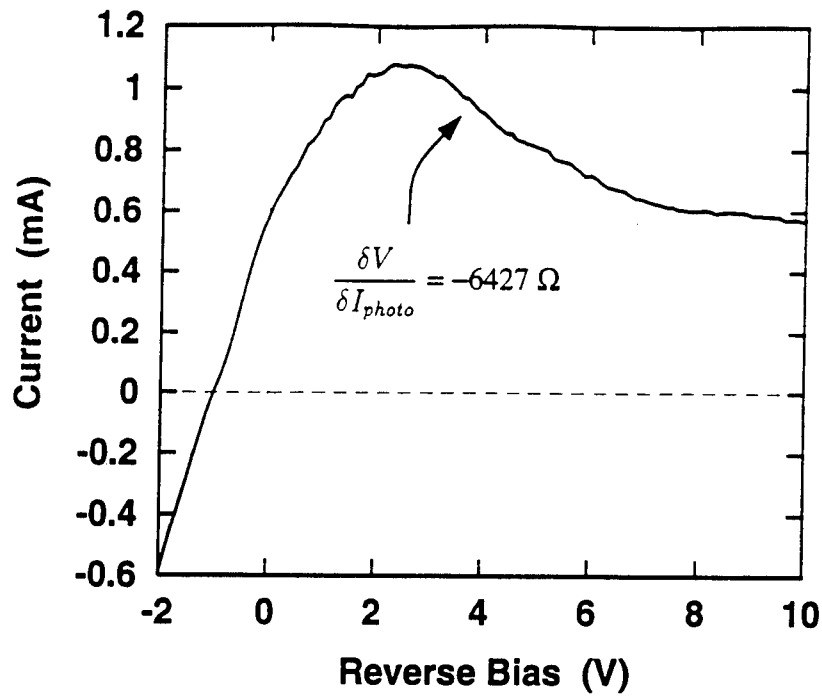


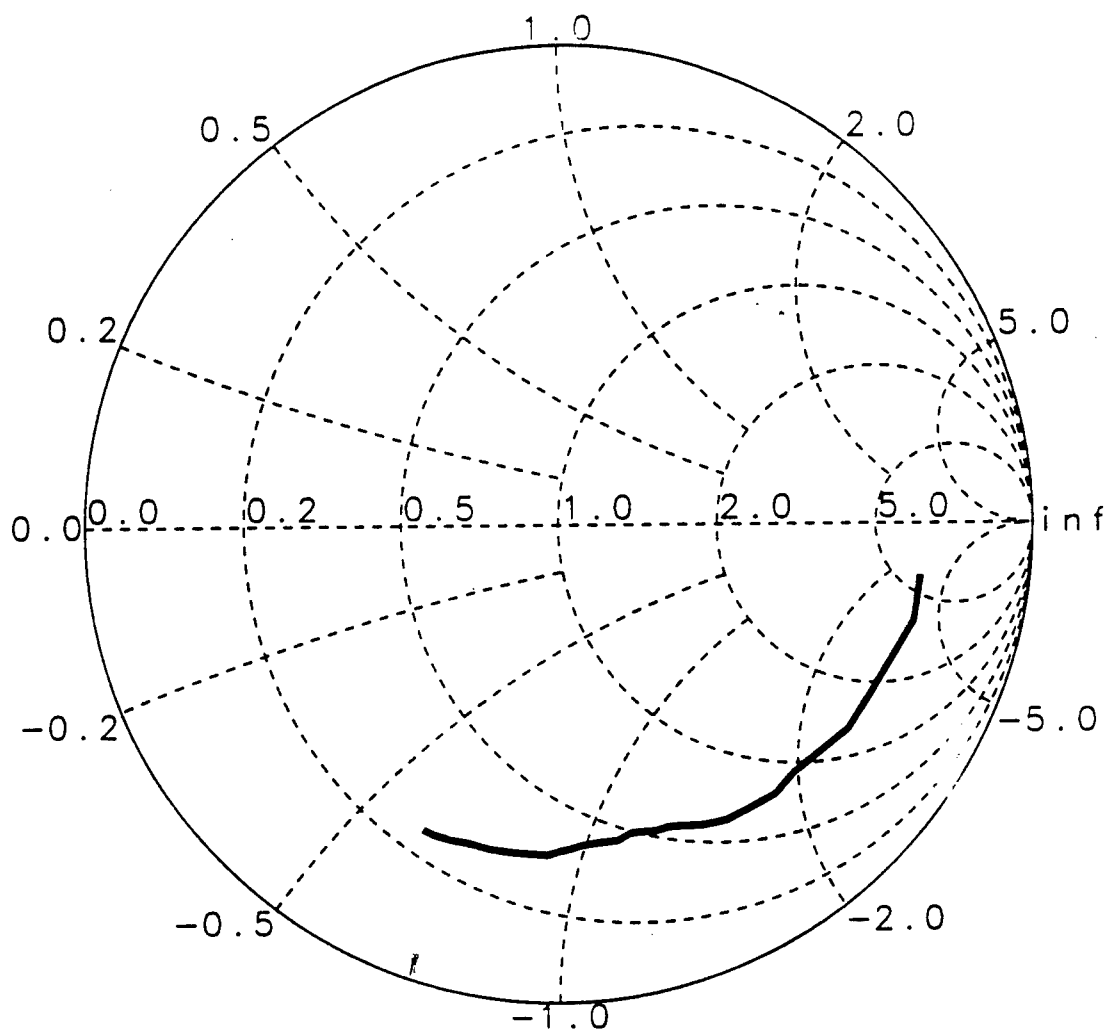
Figure 3.11: I/V response of p-i(MQW)-n photodiode under illumination by 845 nm light

device operation. Since the same absence of high frequency NDR is observed in a simple p-i(MQW)-n structure, a more fundamental problem exists. It appears that further study of this issue will be necessary.

3.6 Summary

The incorporation of a multi-quantum well region in the collector of an HBT has led to a useful phototransistor exhibiting tunable spectral absorption response and optically induced negative differential resistance (NDR). The current gain of the device serves to increase the NDR effect produced by QCSE absorption in the multi-quantum well region. High negative resistance values of -397 were observed from this device.

This NDR effect was shown to be quenched at frequencies near 50 MHz,



Frequency: 0.25 to 10.0 GHz

Figure 3.12: S_{11} of p-i(MQW)-n photodiode under $\lambda = 850$ nm illumination. The transistor was biased at 4 V which corresponds to the position of maximum NDR in DC measurements. No high-frequency NDR is observed.

although the optical impulse response of the transistor indicates the device can be used as a phototransistor at speeds up to 9 GHz. Studies of p-i(MQW)-n devices also showed the NDR quenching effect, indicating that the effect is not caused by a screening effect from the injected electrons in the MQW-HBT collector. Further study of this structure will be required before the NDR effect can be utilized at microwave frequencies.

The MQW-HBT devices exhibited a current gain cut-off frequency (f_T) of 11.7 GHz and a maximum frequency of oscillation (f_{max}) of 5.8 GHz. These values were adequate for making a low-GHz microwave oscillator. The MQW-HBT was subsequently used to demonstrate direct optical tuning and injection locking of an AlGaAs/GaAs HBT oscillator at 2.65 GHz. A tuning range of up to 5 MHz and an injection locking range of 6 MHz have been achieved in this experiment. However, the large device areas and the lack of a self-aligned base contact prevent this device structure from being used for higher frequency HBT applications.

CHAPTER IV

DESIGN AND FABRICATION OF HETEROJUNCTION BIPOLAR TRANSISTORS WITH TRANSPARENT EMITTER CONTACTS

4.1 Introduction

Even with the most optimum layer structures, modern high-performance HBT devices require special fabrication layouts in order to operate at their full potential. One problem is the thin base layers used. The thin base ($t_B < 1\mu\text{m}$) is used to minimize transit time for electron diffusion across the base, and the base layer is highly doped to prevent base punch-through and Early effects. However, base sheet resistances can still be high enough to degrade device performance. A multi-fingered emitter structure with interdigitated base contact electrodes is commonly used to circumvent this problem. Narrow fingers serve to reduce the current crowding effects that occur when large base currents cause a resistive voltage drop across the a wide emitter region. The self-aligned base contact is used to reduce the base resistance by making the separation between the emitter and the base contact small. The emitter structure is designed with a small overhang and then used as a shadow mask for the base contact deposition. With this approach, the distance between the

base contact and the emitter is limited only by the overhang achieved on the emitter mesa etch.

To improve the performance of the optically controlled oscillators, the high-frequency response of the transistors must be improved. It is desirable to have an HBT with optical access that uses the standard high-performance device structure. However, there is a significant obstacle to realizing direct optical coupling with self-aligned HBT devices — the metalizations for the emitter and base ohmic contacts block light access to the transistor's active regions as shown in Fig. 4.1. While Chap. III reports the successful use of emitter structures which allow light to pass through the center of a ring-shaped emitter metalization, the trade-offs involved with this method result in either limiting high frequency performance due to a large emitter size, or reducing optical responsivity due to a small optical access window. A better solution would be to use a standard high speed device structure with self-aligned contacts, but with an emitter and/or base contact material that is *optically transparent*. This device is illustrated in Fig. 4.2. Indium-tin-oxide was chosen as a suitable transparent conducting material.

4.2 Indium Tin Oxide

Sn-doped In_2O_3 , commonly referred to as indium-tin-oxide (ITO), is a *n*-type transparent semiconducting oxide which has been in commercial use since the 1970's. ITO films have been used for a multitude of applications including liquid crystal displays, solar cells and photodiodes [46]–[50].

ITO is optically transparent for the wavelengths used with GaAs optoelectronic devices. The upper limit on wavelength for good optical transmittance is

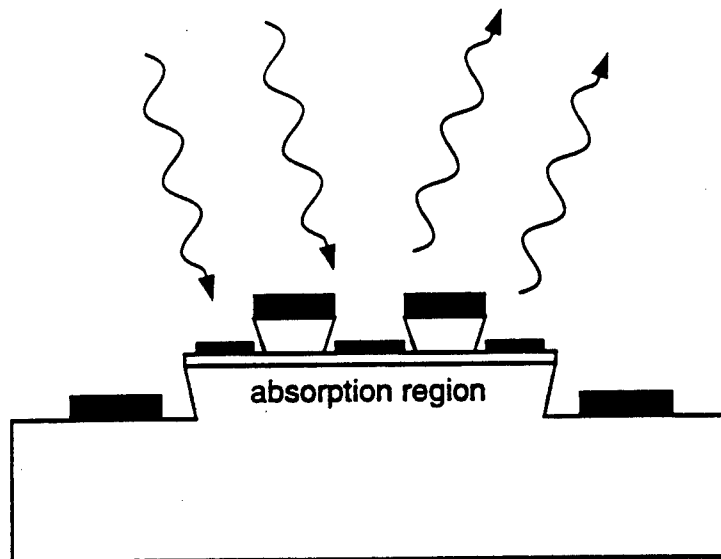


Figure 4.1: Cross section of a conventional self-aligned HBT structure showing how the emitter and base metalizations block all light access through the top of the device.

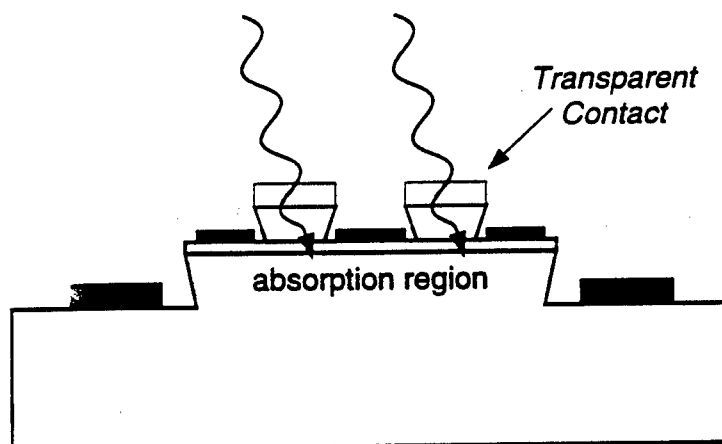


Figure 4.2: Cross section of a self-aligned HBT with transparent emitter contacts. Light is able to pass through the emitter and be properly absorbed in the base-collector depletion region.

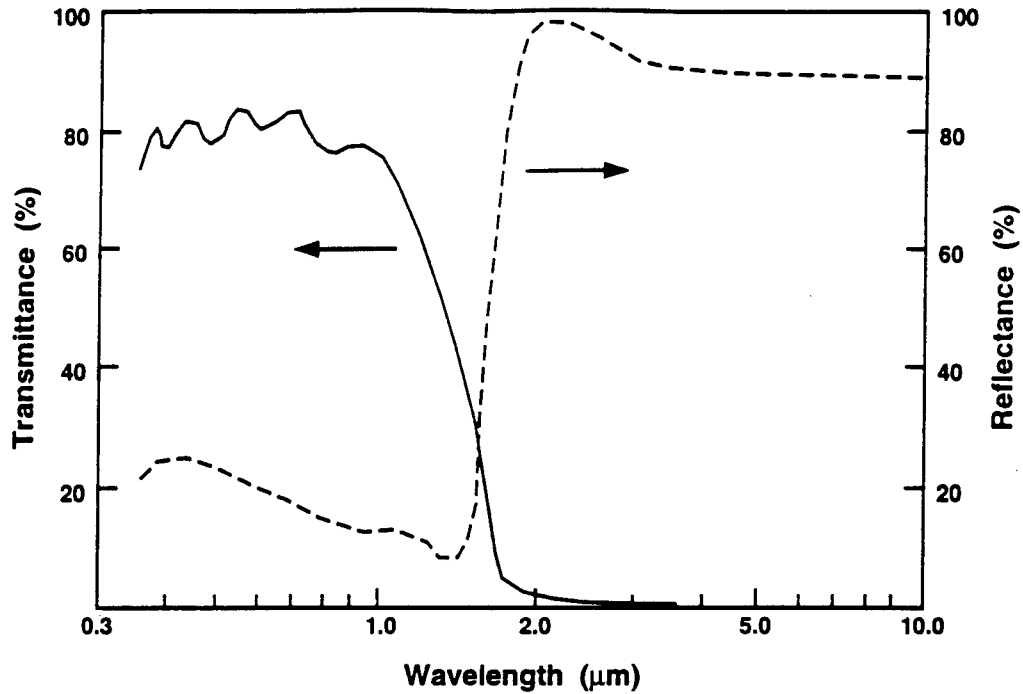


Figure 4.3: Spectral dependence of transmittance T (—) and reflectance R (---) of ITO thin film on glass (after Shanthi *et al.* [51])

$\lambda = 1 \mu\text{m}$, as shown in Fig. 4.3. Optical measurements on In_2O_3 single crystals [52] show a direct band-to-band electronic transitions at 3.75 eV, so the lower limit on wavelength for transparency is $\lambda = 330 \text{ nm}$.

ITO has a conductivity of $\rho = 2 \times 10^4 \text{ }^{-1}\text{cm}^{-1}$ at room temperature [53]. This compares to $4 \times 10^5 \text{ }^{-1}\text{cm}^{-1}$ for Au and $2 \times 10^3 \text{ }^{-1}\text{cm}^{-1}$ for heavily doped poly-Si. ITO has a refractive index of $n = 2$, so, in addition to its favorable electrical qualities, it can be effectively used as *both* a transparent conductor and an anti-reflective coating.

ITO films can be deposited using evaporation, chemical vapor deposition (CVD), or sputtering [54]. Buffered hydrofluoric acid (BHF) can be used for etching large patterns into ITO. For small features, ITO can be reliably etched using reactive ion etching (RIE). A methane/hydrogen (CH_4/H_2) plasma will

provide good selectivity between etching of ITO and GaAs [55]. Alternately, if thin films are deposited by sputtering or evaporation, small features can be patterned into ITO using a standard photoresist lift-off process. We have been able to fabricate small features with dimensions down to 1 μm using photoresist lift-off patterning.

4.2.1 ITO as a Transparent Emitter Contact

When placed in direct contact with *n*- or *p*-type GaAs, a Schottky contact is formed between the ITO and the semiconductor. The barrier height between ITO and *n*-type GaAs has been measured to be 0.67 V [56]. While this effect has been utilized to produce highly efficient Schottky photodiodes [48], non-ohmic contacts would degrade the performance of HBT devices.

Berger *et al.* [57] found that with a similar transparent conductor, cadmium-tin-oxide (CTO), the use of a semi-transparent pre-layer of either In or Ag allowed formation of ohmic contacts to InGaAs. Similarly, Tu *et al.* [58] employed CTO with a Ag pre-layer to obtain ohmic contacts to *p*-type GaAs. The primary application of CTO is for long wavelength opto-electronic devices. CTO is studied because it has good optical transmittivity at 1.55 μm . For wavelengths below 1 μm , ITO is preferred due to its higher conductivity.

Previous attempts to create In_2O_3 ohmic contacts to GaAs were promising but incomplete. Cunningham *et al.* [56] used In doped In_2O_3 to form an ohmic contact to *n*-type GaAs. After a 4 minute 700° C anneal, the In was found to diffuse from the In: In_2O_3 into the semiconductor and a semi-ohmic behavior under reverse bias operation was observed. However, the forward bias current still had the standard exponential dependence on voltage. Also, the long anneal

at such a high temperature would allow undesirable dopant diffusion within the semiconductor device layers.

For this work, an ITO ohmic contact has been developed and optimized for *n*-type GaAs with a typical specific contact resistance on the order of 10^{-4} cm². In pre-layers along with an appropriate annealing sequence are used to allow the formation of ohmic contacts.

4.2.2 Optimization of ITO Ohmic Contact to *n*-GaAs

The ITO films used for this work were deposited by RF magnetron sputtering of a 91% In₂O₃ : 9% SnO₂ composite target onto unheated substrates. The sputter target was constructed by Johnson & Mathey Co. The sputtering was performed in a 7 mTorr Ar ambient at a RF power level of 450 W. Before flowing the Ar ambient for sputtering, long chamber pump-downs were performed to ensure that no appreciable amount of O₂ was residual in the chamber. The presence of even a small partial pressure of oxygen in the sputtering chamber causes a degradation in film conductivity [59].

To prevent formation of a rectifying contact to *p*- or *n*-type GaAs, a 5–10 nm layer of silver or indium was deposited by electron beam evaporation before sputtering the ITO. This thin pre-layer is practically transparent and serves as an intermediary layer that helps form ohmic contacts. Indium is used for ITO/*n*-GaAs contacts while Ag is used for ITO/*p*-GaAs contacts. After the post-deposition annealing, the In layer is suspected of forming a thin surface layer of InGaAs which will more easily form an ohmic contact with ITO due to its lower bandgap. The silver prelayer in ITO/*p*-GaAs contacts prevents formation of a *p*-*n* junction between the *p*-GaAs and the ITO film which is inherently an

n-type semiconductor. In both cases, the semiconductor must be heavily doped ($N > 1 \times 10^{18}$) to achieve the ohmic behavior.

Post-deposition rapid thermal annealing (RTA) is required to remove structural defects and improve the electrical and optical characteristics of the film. For a 30 second RTA anneal, the ITO film characteristics were found to vary depending on the annealing temperature. Figure 4.4 shows the temperature dependence of sheet resistance and of $\lambda = 830$ nm optical transmittance. While optical transmittance is shown to increase with temperature for the entire range of the test (up the 500° C), the sheet resistance shows a minimum value of 1.3 / \square at $T = 460^\circ$ C. At 460° C, the transmittance is 82% which is only slightly lower than the maximum observed transmittance of 89%. Figure 4.5 shows the specific contact resistance as a function of anneal temperature. The minimum resistivity of 4.24×10^{-4} cm² is seen for an anneal at $T = 450^\circ$ C. However, since film transmittance is significantly lower for this anneal temperature, a $T = 460^\circ$ C anneal was selected for use in the actual device fabrication. The contact resistivity at this temperature is only slightly higher with $R_C = 4.3 \times 10^{-4}$ cm².

4.3 ITO-HBT Design and Fabrication

The layer structure for the HBT devices is shown in Table 4.1. Note that the GaAs emitter cap layer is made very thin since GaAs will act as an absorbing layer for light directed through the top of the device. A transparent higher bandgap AlGaAs layer was not used because contact resistivity would be increased. The HBT structure was grown on a semi-insulating GaAs substrate using a Varian Gen II MBE machine.

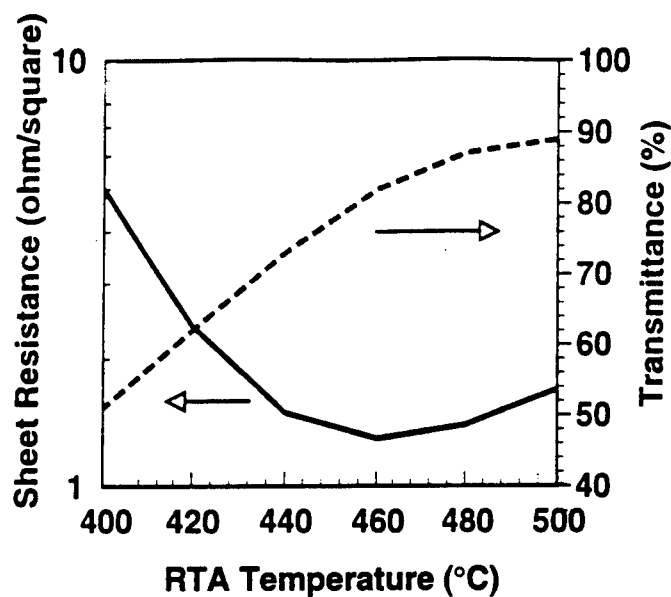


Figure 4.4: Sheet resistance and $\lambda = 830$ nm transmittance of a 200 nm ITO film with a 6 nm In prelayer after a 30 second RTA anneal. Optimum transmittance is seen for $T > 480^\circ\text{C}$, while the sheet resistance has a minimum at $T = 460^\circ\text{C}$.

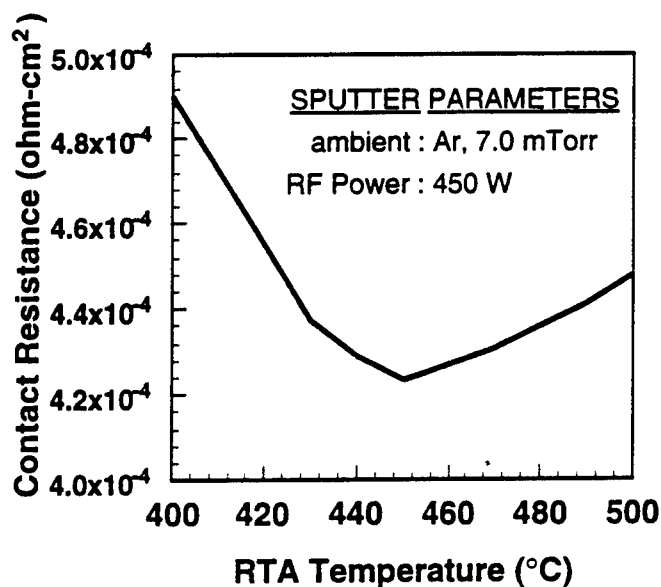


Figure 4.5: Specific contact resistance to n -type GaAs of a 200 nm ITO film with a 6 nm In prelayer after a 30 second RTA anneal. A minimum contact resistance of $4.2 \times 10^{-4} \text{ cm}^2$ is obtained with a 450°C anneal.

Table 4.1: Layer structure of AlGaAs/GaAs ITO-HBT

Layer	Composition	Thickness	Doping (cm^{-3})
Cap	GaAs	20 nm	$n = 5 \times 10^{18}$
Emitter	$\text{Al}_{0.25}\text{Ga}_{0.75}\text{As}$	$0.3 \mu\text{m}$	$n = 5 \times 10^{17}$
Base	GaAs	$0.1 \mu\text{m}$	$p = 1 \times 10^{19}$
Collector	GaAs	$0.6 \mu\text{m}$	$n = 2 \times 10^{16}$
Sub-collector	GaAs	$0.5 \mu\text{m}$	$n = 5 \times 10^{18}$
Substrate	GaAs		semi-insulating

Although ITO could be used for both the emitter and base contacts to allow maximum light access, ITO is only used for the emitter contact in the HBT devices. This is because the contact resistance between ITO and p -type GaAs is higher than that of n -type GaAs. Base resistance is a primary factor in limiting the high frequency performance of the HBT. The maximum frequency of oscillation, f_{max} , is approximated by [60]

$$f_{max} \simeq \sqrt{\frac{f_T}{8\pi R_B C_{BC}}}, \quad (4.1)$$

where R_B the base resistance, f_T is the current gain cutoff frequency, and C_{BC} the base-collector capacitance. It is evident that to maximize f_{max} , R_B must be kept as low as possible. Consequently, a standard metallic ohmic contact was used for the base contact.

The HBT structure was grown by MBE and self aligned devices with $2\mu\text{m} \times 10\mu\text{m}$ emitter fingers and interdigitated base contacts were fabricated [61]. Device fabrication followed the process described in section 2.4. A scanning electron micrograph of a fabricated ITO-HBT device is shown in Fig. 4.6.

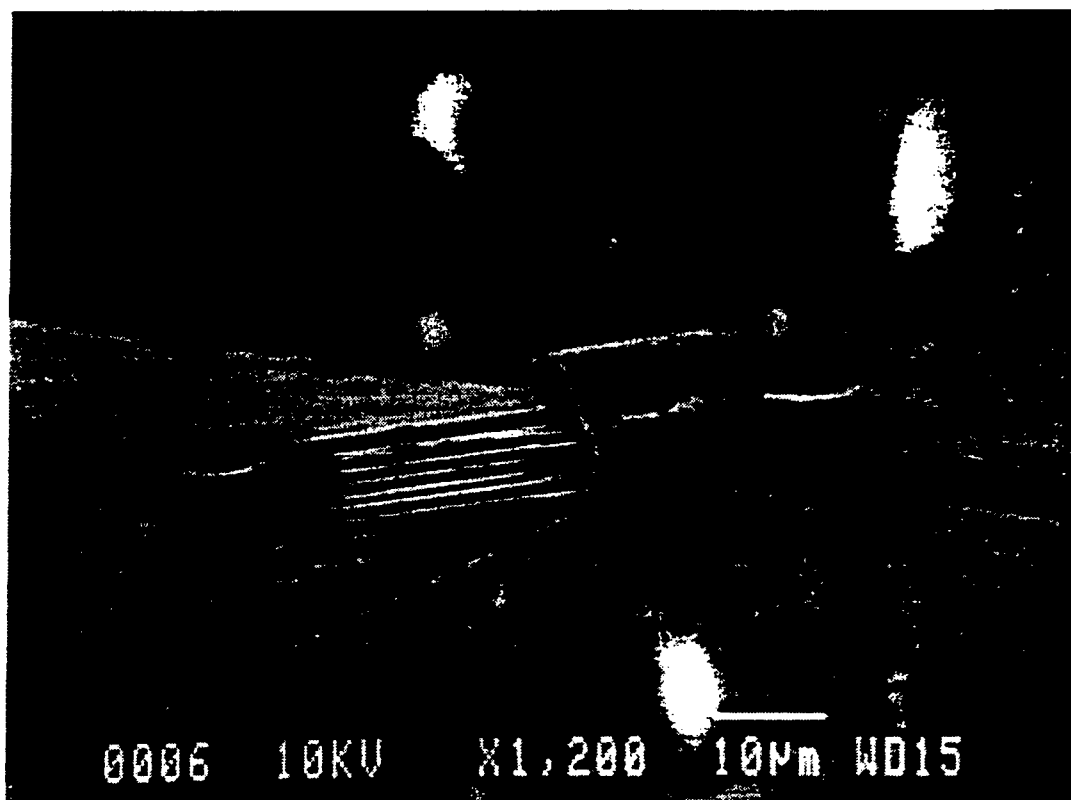


Figure 4.6: Scanning electron micrograph of a fabricated ITO-HBT device. The pictured device has a 3 finger emitter structure with $2\mu\text{m} \times 10\mu\text{m}$ fingers.

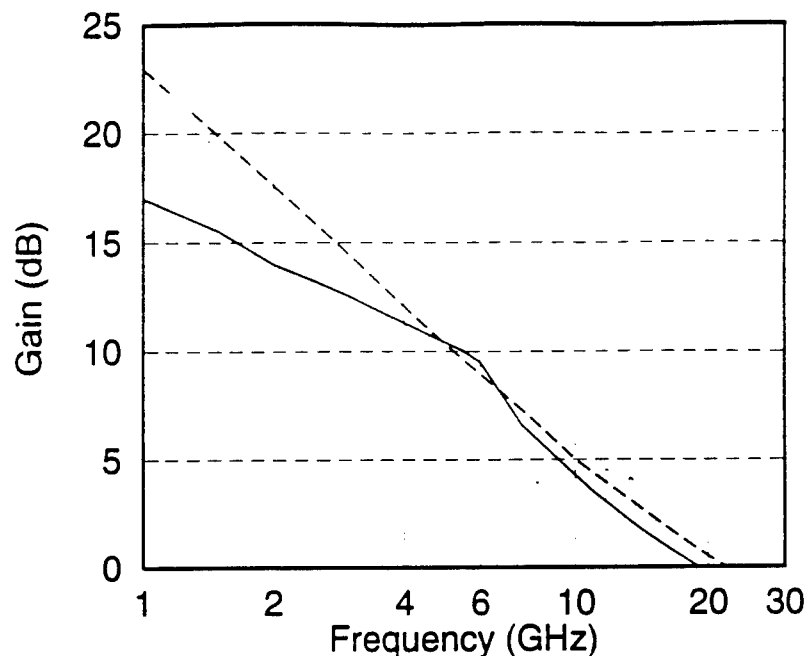


Figure 4.7: Measured current gain h_{21} (---) and power gain G_{max} (—) of ITO-HBT. At bias conditions $I_C = 10$ mA and $V_{CE} = 3$ V, the current gain cutoff frequency (f_T) and maximum frequency of oscillation (f_{max}) were found to be 19 and 21 GHz respectively.

4.3.1 ITO-HBT Performance

DC and RF Characteristics

DC characterization was performed using an HP 4145 Semiconductor Parameter Analyzer. Common-emitter DC measurements showed uniform current gains (h_{fe}) of 10–20 and junction ideality factors of 1.01 and 1.43 for the base-collector and emitter-base junctions, respectively.

Microwave performance of the devices was measured from 45 MHz – 26.5 GHz using an HP 8510 network analyzer. The short circuit current gain (h_{21}) and the maximum available power gain (G_{max}) were computed from the measured S-parameters and are shown in Fig. 4.7. At bias conditions $I_C = 10$ mA and $V_{CE} = 3$ V, the current gain cutoff frequency (f_T) and maximum frequency of

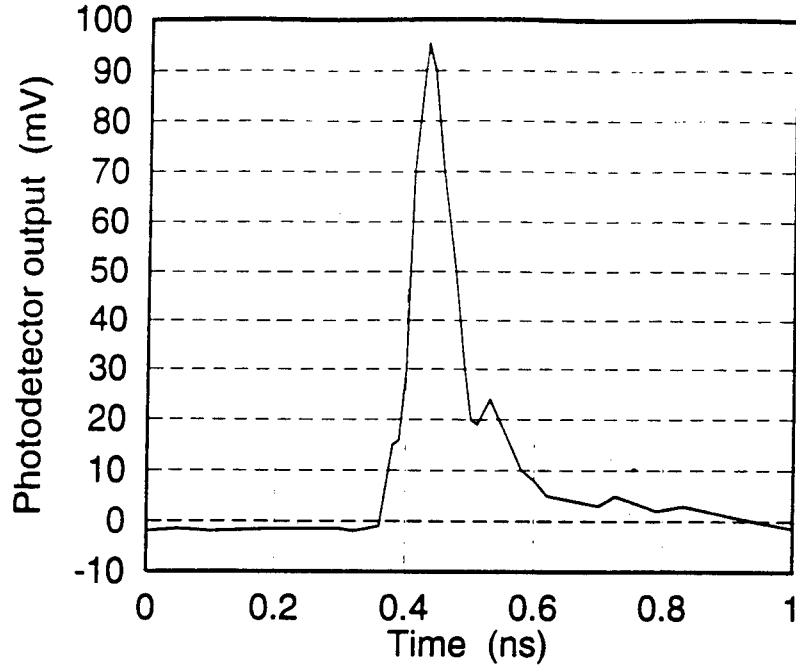


Figure 4.8: Optical impulse response of ITO-HBT. The detected response shows a *FWHM* of 80 ps. The deconvolved impulse response is 71 ps.

oscillation (f_{max}) were found to be 19 and 21 GHz respectively.

Optical Impulse Response

To investigate the photoresponse of the HBTs, short optical excitation pulses from a mode-locked dye laser ($\lambda = 853$ nm) pumped with a Nd:YAG laser were used. The nominal pulse width of the dye laser pulses was 7 ps with a repetition rate of 76 MHz. The response of the phototransistor at $V_{CE} = 4$ V and $I_B = 50$ μ A showed a full width at half maximum (*FWHM*) of $\tau_{meas} = 80$ ps, as shown in Fig. 4.8. Taking into account the optical pulse width ($\tau_{pulse} = 7$ ps) and the *FWHM* of the sampling head response ($\tau_{head} = 35$ ps), intrinsic device response time is can be extracted using Eqn. A.19. (see App. A)

$$\tau_{device} = \sqrt{\tau_{meas}^2 - \tau_{pulse}^2 - \tau_{head}^2}, \quad (4.2)$$

$$\tau_{\text{device}} = \sqrt{(80\text{ps})^2 - (7\text{ps})^2 - (35\text{ps})^2} , \quad (4.3)$$

$$\tau_{\text{device}} = 71\text{ps} . \quad (4.4)$$

From the impulse response, the phototransistor bandwidth can be approximated using Eqn. A.25,

$$f_{\text{photo}} = \frac{2 \ln 2}{\pi} (\tau_{\text{device}})^{-1} . \quad (4.5)$$

The highest frequency that the device will work as a photo-transistor is thus estimated to be 6.2 GHz.

4.3.2 Effect of Light Absorption

To study the high frequency characteristics of the HBTs under optical illumination, light with wavelength $\lambda = 830$ nm from a AlGaAs laser diode was directed through the transparent ITO contacts of the device via a fiber optic probe system. S-parameter measurements were then performed. The devices were externally biased in a common emitter configuration with a constant base current $I_{B(\text{ext})}$ and collector voltage V_{CE} . It was found that increasing the incident optical power P_{inc} caused a corresponding increase in collector current I_C . This effect is consistent with the photo-generated holes acting to increase the device's total base current I_B .

To determine if adding to the base current is the primary effect of optical absorption, S-parameter measurements were performed at several different optical power levels (P_{inc}) but with $I_{B(\text{ext})}$ adjusted such that I_C remained constant for all measurements. Assuming current gain remains unchanged under illumination, holding I_C constant implies that the total base current I_B also remains constant. Figure 4.9 compares the measured S-parameters of a two-

finger $5\mu\text{m} \times 20\mu\text{m}$ emitter HBT with constant I_C but with two different I_B : P_{inc} combinations. As can be seen, the S-parameters show no difference in the device's high-frequency characteristics all the way out to 20 GHz. This verifies that the principle effect of optical absorption is to increase the base current.

The optically generated base current ($I_{B(\text{opt})}$) and the extrinsic quantum efficiency (η_{ex}) of the photo-absorption process can be determined as

$$I_{B(\text{opt})} = q\eta_{ex} \frac{P_{inc}}{hc/\lambda} \quad (4.6)$$

and, therefore,

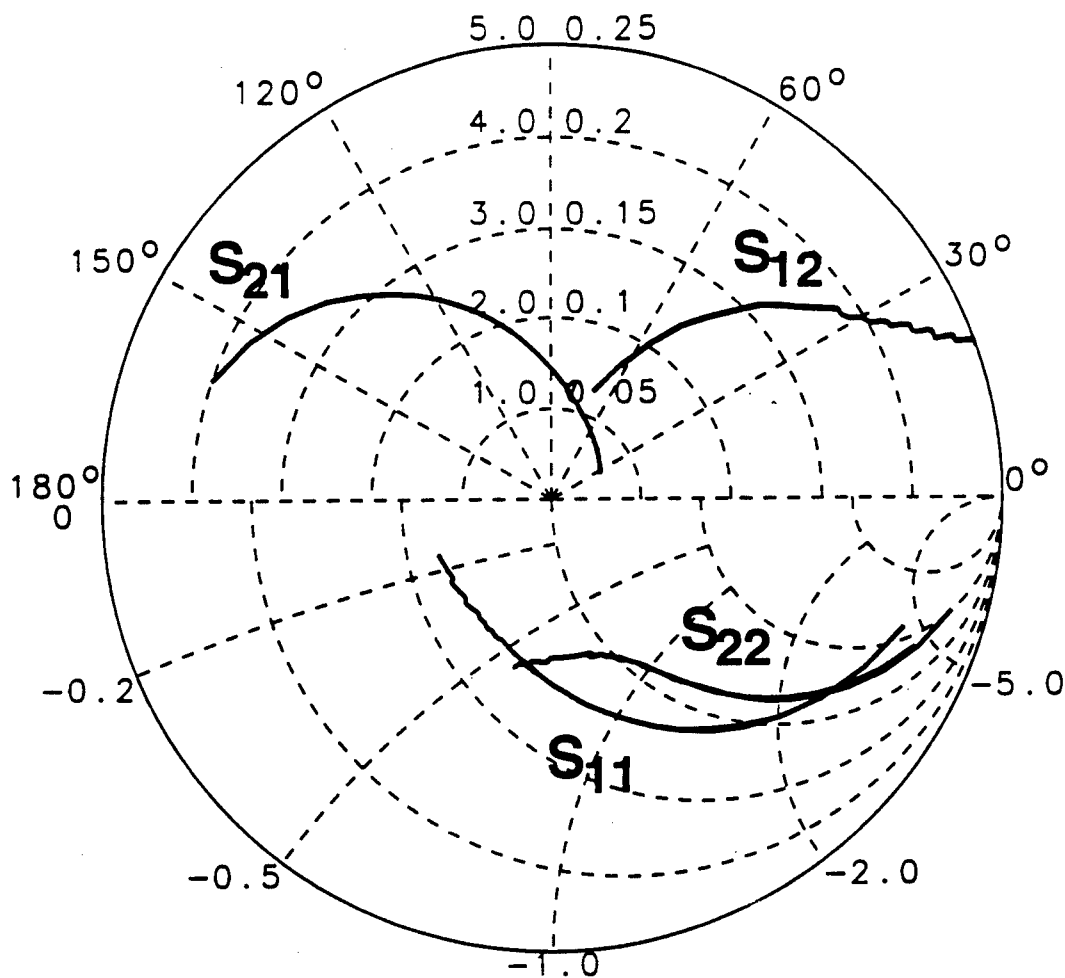
$$\eta_{ex} = \frac{hc}{q\lambda} \left(\frac{I_{B(\text{opt})}}{P_{inc}} \right), \quad (4.7)$$

where P_{inc} is the incident optical power and λ is the wavelength of the incident light. The extrinsic quantum efficiency was found to be $\eta_{ex} = 0.27$ and was constant for measurements at different bias and illumination conditions. This agrees with the predicted efficiency considering that 50% of the light is blocked by the base metalization, transmittance through the ITO was measured at 85%, and the surface reflection at the air to ITO/GaAs interface (refractive index n for ITO is ~ 2) is approximately 30%. This leaves 30% of the incident light available for photo-absorption which is consistent with the above figure. Efficiency can be improved to a maximum of 40% by designing the thickness of the ITO layer such that the ITO forms an anti-reflecting layer.

The optical gain is defined as

$$G = \frac{hc}{q\lambda} \left(\frac{I_{ph}}{P_{inc}} \right), \quad (4.8)$$

where I_{ph} is the optically generated component of the collector current. For the measured device, a maximum optical gain of $G = 9.0$ was observed.



Frequency: 0.5 – 20 GHz

Figure 4.9: S-parameters of ITO-HBT under both illuminated and dark conditions. Both measurements were performed with bias conditions of $V_{CE} = 4\text{V}$ and $I_C = 10.5\text{mA}$. The dark measurement was performed with all base current supplied electrically, $I_B = 0.374\mu\text{A}$. The illuminated measurement had incident optical power of $P_{inc} = 3\mu\text{W}$, and the base current lowered to $I_B = .318\mu\text{A}$ so that the collector current remained the same. The two curves are indistinguishable all the way to 20 GHz which indicates that the effect of light absorption is the same as increasing the device base current.

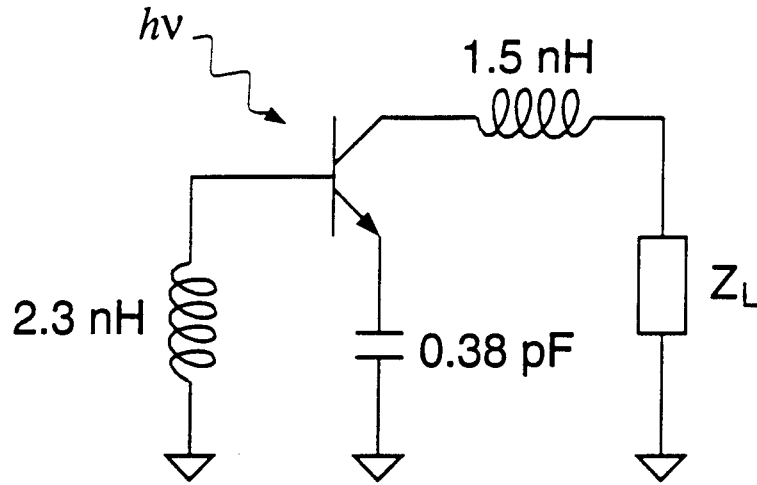


Figure 4.10: Diagram of ITO-HBT oscillator circuit

4.4 Optical Control of ITO-HBT Microwave Oscillators

A 6 GHz oscillator was designed based on the measured S-parameter data for the HBTs. The feedback network for the oscillator consisted of an inductive load of $L = 2.4$ pH connected to the base and a capacitive load of $C = 0.40$ pF connected to the emitter. An inductive matching network was designed between the collector terminal and the 50 Ω load. A diagram of the oscillator circuit is shown in Fig. 4.10. Circuits were built on 15 mil Duroid substrates using microstrip lines for distributed feedback elements and impedance matching. For each oscillator circuit, one transistor was wire bonded onto the microstrip board. The HBT was biased externally through bias tees. It was found that at $V_{CE} = 5$ V and $I_C = 4.5$ mA, free running oscillations at 5.68 GHz were observed with a maximum output power of 7.6 mW. This corresponds to a DC to RF power conversion efficiency of 34%.

4.4.1 Optical Injection Locking

Direct optical injection locking experiments were performed by focusing the output of an 830 nm laser diode onto the ITO contacts of the ITO-HBT [62]. The light was modulated by superimposing a high power RF signal at 5.68 GHz over the diodes DC bias current.

Direct optical injection locking was observed by modulating the superimposed RF power to the laser diode at frequencies near the free-running oscillation frequency. When the oscillator was unlocked but with the injected signal (f_{inj}) close to the oscillating frequency ($f_{opr} = 5.68$ GHz), the oscillator output spectra contained multiple single-sided sidebands similar to those shown in Fig. 3.8. This phenomena is consistent with the expected behavior of unlocked oscillators [45]. When f_{inj} was tuned to within the locking range, all sidebands disappeared and phase noise was significantly reduced.

Figures 4.11 and 4.12 respectively show the free running and optically injection locked output spectra of the oscillator. The maximum locking range observed for direct optical injection locking was 2.5 MHz and FM noise suppression was found to be 17 dB at a 10 KHz offset.

In this experiment, the available locking range was limited by the modulation capabilities of the laser diode. At the locking frequencies near 6 GHz, the modulation depth of the laser light was very small. To determine the actual microwave power induced by the modulated optical signal, a microwave injection locking experiment was performed on the same oscillator. With microwave injection, a locking range of 10 MHz was observed with an injection locking signal at a power level of -10 dBm. The Q factor of the oscillator can be estimated by using Adler's equation (see Eqn. 1.1) for injection locking

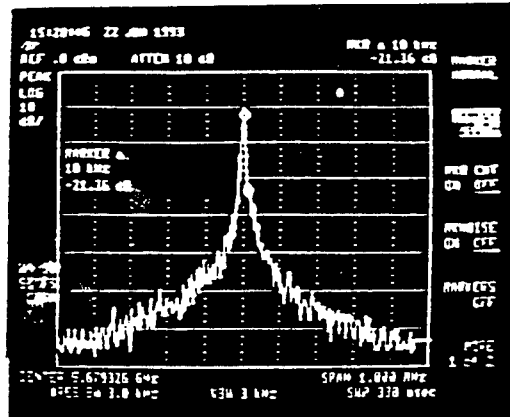


Figure 4.11: Free running output spectrum of ITO-HBT oscillator

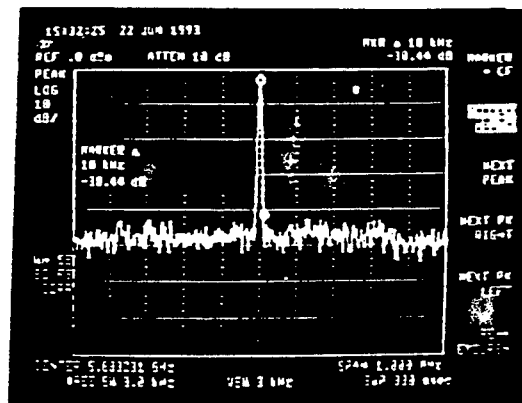


Figure 4.12: Output spectrum of optically injection locked ITO-HBT oscillator

bandwidth:

$$\omega_{max} = \frac{\omega_o}{2Q} \sqrt{\frac{P_{inj}}{P_0}} \quad (4.9)$$

$$10 \text{ MHz} = \frac{5.86 \text{ GHz}}{2Q} \sqrt{\frac{0.1 \text{ mW}}{1 \text{ mW}}} \quad (4.10)$$

which gives

$$Q = 92.7 \quad (4.11)$$

Now, by using the Eqn. 4.9 with the calculated value of Q and the measured optical injection locking range, the actual microwave power created by absorption of modulated light is estimated to be -22 dBm or $6.25 \mu\text{W}$. It is expected that a more efficient optical modulation scheme would greatly improve the optical injection locking bandwidth. Also, by designing oscillators with lower Q factors, higher optical injection locking ranges can be realized.

4.4.2 Optical Tuning

Optical tuning experiments were performed by focusing the output of the 830 nm laser diode through the transparent ITO contacts of the HBT and then adjusting the optical power level by changing the current through the laser. Optical tuning effects were monitored by viewing the oscillator's output spectrum on a spectrum analyzer. It was found that increasing the incident optical power from 0 to $16 \mu\text{W}$ caused a corresponding increase in oscillation frequency of 20 MHz . A maximum optical tuning range of 25 MHz was observed [63].

4.5 Modeling of Device and Circuit Parameters

The oscillation frequency can be approximated as the resonant frequency of the RLC loop created by the base inductor, emitter capacitor, and the

impedance across the base and emitter terminals of the HBT which is both resistive and capacitive. Following the analysis in Sec. 3.2.2, this resonant frequency is

$$f_{osc} \cong \frac{1}{2\pi\sqrt{L_b C_{eff}}}, \quad (4.12)$$

where L_b is the inductance connected to the base and C_{eff} is the series combination of the internal device capacitance and the external emitter capacitance. It is evident that, to study the optical tuning behavior of the oscillators, the behavior of the impedance presented at the HBT's base terminal must be explored.

The small signal equivalent circuit model for the HBT is shown in Fig. 4.13. The forward biased base-emitter junction is represented by two elements: R_{je} is the resistance of the junction, C_{je} is the junction capacitance which is primarily a diffusion capacitance. The reverse biased base-collector junction is represented by a depletion capacitance C_{jc} and an isolation resonance R_{jc} .

The equivalent circuit parameters were optimized for a best match to measured S-parameter data taken at several different optical power levels. The extracted values were then compared to determine which elements are most affected by the photo-generation of carriers within the device. The extracted element values for the transistor in the dark condition are shown with the diagram in Fig. 4.13. Table 4.2 highlights the values that were found to change under illumination. A primary effect of the light absorption is a decrease in the base-emitter junction resistance R_{je} which is the expected result when the current through a p-n junction is increased. Also, the diffusion capacitance C_{je} is shown to decrease, corresponding to a decrease in incremental charge

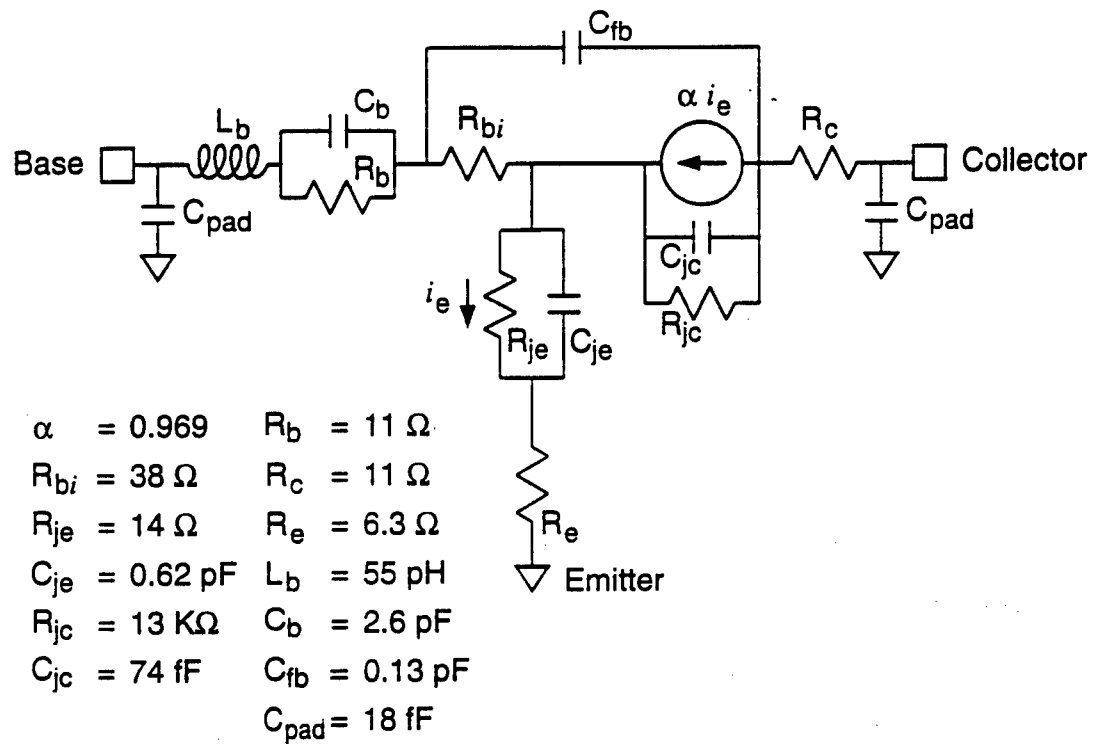


Figure 4.13: ITO-HBT equivalent circuit model and element values with no device illumination

Table 4.2: Variation of equivalent circuit parameters under several different incident optical power levels. Values not listed do not change appreciably with P_{inc} .

P_{inc}	α	R_{je}	C_{je}	C_{jc}
0 μ W	0.969	14.0	0.62 pF	74 fF
3 μ W	0.971	13.5	0.57 pF	77 fF
6 μ W	0.974	13.1	0.53 pF	80 fF
9 μ W	0.976	12.9	0.50 pF	82 fF
12 μ W	0.977	12.7	0.47 pF	85 fF

storage with increased junction current. This effect is not well understood, but could be partly due to a re-adjustment of the emitter-base junction parameters due to the photogenerated holes. The other values were found to have only minor changes.

The optical tuning effects can now be correctly modeled. The circuit between the emitter and base terminals is adequately modeled as a series resistance and capacitance when considered at a fixed frequency of 6 GHz. In this case, R_{equiv} increases from 33.42 to 33.04 and C_{equiv} decreases from 1.032 pF to 1.013 pF as the incident optical power is increased from 0 to 12 μ W. The device capacitance, C_{equiv} , is then considered in series with the external inductor ($L = 2.4$ pH) and capacitor ($C = 0.40$ pF) of the oscillator feedback network. Using Eqn. 4.12, The estimated oscillation frequency is found to change from 6.0507 GHz to 6.0665 GHz for the incident optical power level change of 0 to 12 μ W. This represents an increase of 16 MHz which is in very good agreement with the observed frequency tuning.

4.6 Alternate ITO Schemes

It is evident from device modeling that the primary limiting factor in the ITO-HBT is the high resistance of the ITO ohmic contact. To improve the contact resistance of the ITO contact, I explored the possibility of using more conventional contact materials for the ITO pre-layer. Of particular interest was the use of a germanium-gold pre-layer.

4.6.1 Germanium-Gold Contacts

The germanium-gold alloy has become the most widely used metalization for *n*-type ohmic contacts to GaAs. Contact resistivities in the mid 10^{-7} cm^2 range are commonly achieved using this metalization system.

Ge/Au is deposited in proportions to create a eutectic alloy. This corresponds to the mixture which has the lowest melting point temperature. For the Ge/Au alloy, the eutectic is formed with 88% Au and 12% Ge by weight which has a melting point of 360° C. When heated to temperatures above 360° C, the Ge/Au alloy begins to melt and a reaction takes place between the Au and the gallium at the GaAs surface. Gallium is dissolved into the metal leaving vacancies which are then filled by germanium from the Ge/Au alloy. Germanium in a gallium site forms an *n*-type dopant. After the annealing process, the surface layer of the GaAs becomes doped at concentrations exceeding $2 \times 10^{19} \text{ cm}^{-3}$ and a low resistance tunneling contact is created [15]. The diffusion depth of Ge into the surface is dependent on the thickness of the applied Au and Ge layers. Commonly, the combined Ge/Au thickness is 100 nm which results in a 200 nm diffusion of Ge [64].

In practice, several additional materials are used in addition to the Ge/Au.

Commonly, the full metalization sequence is Ni/Ge/Au/Ti/Au. Ni serves as a wetting agent which prevents "balling up" of the metal [65]. The top Au layer is made thick (150–250 nm) and is used to reduce the sheet resistance of the contact. The Ti layer is a barrier layer which prevents the top Au layer from changing the Ge/Au ratio in the lower contact area.

4.6.2 Experimental Ge/Au/Ti/ITO Ohmic Contact

Since the primary purpose of using an ITO contact is to create a transparent contact, the Ge/Au prelayer must be made thin enough to remain semi-transparent. The tested contact used a pre-layer of Ge/Au/Ti applied in thicknesses of 7 nm, 14 nm, and 4 nm respectively. The Ge and Au layer thickness are correctly proportioned to form the eutectic. The Ti layer was added to act as a barrier to prevent interdiffusion between the Ge/Au and the ITO.

Test contacts were fabricated on n^+ -GaAs in the standard TLM pattern formation. Pattern definition was achieved using a photoresist mask with a suitable undercut profile for lift-off processing. The Ge, Au, and Ti layers were first deposited by evaporation, then 200 nm of ITO was deposited using RF magnetron sputtering as described in section 4.2.2. After an acetone lift-off procedure, the Ge/Au/Ti/ITO contacts were RTA annealed at varying temperatures to determine the annealing conditions for optimum contact resistivity.

Figure 4.14 shows the specific contact resistance as a function of RTA annealing temperature for a 30 second anneal. A minimum contact resistance of $4 \times 10^{-5} \text{ cm}^2$ is found at an anneal temperature of 400° C. This temperature the same as the optimum annealing temperature for the standard

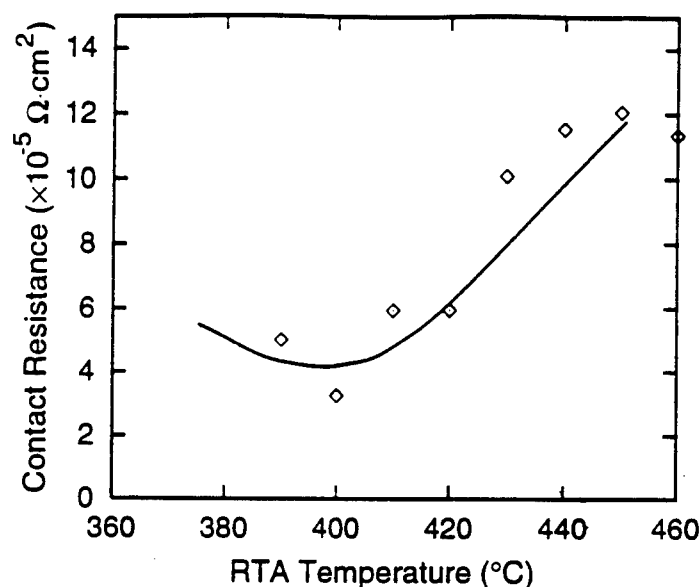


Figure 4.14: Specific contact resistance of ITO with a Ge/Au/Ti prelayer following a 30 second RTA anneal. The contact resistance is improved by one order of magnitude over the In/ITO contact.

Ni/Ge/Au/Ti/Au contacts. This indicates that the Ge/Au contact is indeed forming a low resistance contact as predicted. Furthermore, the measured contact resistivity is a full order of magnitude lower than that measured for the In/ITO contact developed previously.

Unfortunately, as shown in Fig. 4.4, ITO's transmittance after a 400° C anneal is only 50%, and the transmittance of the 25 nm metal pre-layer was measured to be near 40%. Therefore, this contact only allows 20% of the incident light to pass. This would reduce the optical responsivity of the HBT by a factor of 4. Furthermore, although the contact resistivity has been improved by one order of magnitude, it is still two orders of magnitude worse than that of the standard metal ohmic contact. To make a very high speed HBT, standard metal contacts need to be used, and a different method for light access must be found.

4.7 Summary

This chapter has described the development and successful use of a transparent contact HBT for an optically controlled microwave oscillator. The transparent contact material used was $\text{Sn:In}_2\text{O}_3$, commonly referred to as indium-tin-oxide or ITO. With the use of an In prelayer, an ohmic contact to n -type GaAs was developed and optimized. A specific contact resistivity of $4.2 \times 10^{-4} \text{ cm}^2$ was observed with an ITO/In/ n -GaAs ohmic contact. Further studies of the ITO contact found that with the use of a Ge/Au prelayer, contact resistance is lowered by an order of magnitude at the expense of optical transmittance.

Using In/ITO as a transparent emitter contact, self aligned HBTs were fabricated with DC current gains of 20–30 and high frequency cutoff frequencies of $f_T = 19 \text{ GHz}$ and $f_{max} = 21 \text{ GHz}$. Using these devices, optically controlled microwave oscillators operating near 6 GHz with up to 10 mW of output power were built and tested. Direct optical control experiments showed an optical tuning range c. 25 MHz and an optical injection locking range of 2.5 MHz. The ITO-HBT has proven to be very promising for use in optically controlled microwave circuits operating at low microwave frequencies.

CHAPTER V

HIGH-FREQUENCY HETEROJUNCTION BIPOLAR TRANSISTORS WITH GUIDED-WAVE OPTICAL INPUT

5.1 Introduction

Although the work reported in Chap. IV has shown that HBT technology utilizing transparent ITO emitter ohmic contacts is viable for use in microwave frequency optical control applications, the higher emitter contact resistance restricts the use of the ITO-HBT to low-gigahertz applications. For higher frequencies it is important to use conventional metal-emitter HBT devices. As these devices do not allow for through-the-top light input, optical control systems using metal-emitter HBTs require an alternate optical signal input scheme.

Backside Illumination

In InP-based designs, there is the possibility of supplying the control light directly through the substrate. The InP substrate, with a bandgap of $E_g = 1.35$ eV, is transparent to light of wavelength $\lambda > 0.9 \mu\text{m}$. Since, the InP-based opto-electronic devices of greatest interest are designed for operation

at wavelengths between 1.3–1.55 μm , substrate absorption is not a problem. There are several disadvantages to backside illumination, however. First, it is more difficult to align and focus light into the desired absorbing area of small devices. Additionally, the absorption coefficient of $\text{In}_{.53}\text{Ga}_{.47}\text{As}$ for 1.5 μm light is less than 10^4 cm^{-1} [66]. With the 0.5 μm thick absorption region common in HBT devices, less than 40% of the available light will be absorbed. (Naturally, this is also a problem for top-illuminated structures). Fukano *et al.* [67] designed an InP/InGaAs HBT structure with a reflecting top electrode so that the back-illuminated light would pass through the absorbing region twice and the optical responsivity would be increased. However, in addition to placing restrictions on the device layout such that the top mirror will be effective, this method does nothing to alleviate the alignment difficulty.

For $\text{AlGaAs}/\text{GaAs}$ -based devices, backside illumination is much more difficult. The GaAs substrate represents the lowest bandgap material in the system and will be strongly absorbing to optical illumination intended for $\text{AlGaAs}/\text{GaAs}$ devices. Backside illumination is only possible if the substrate is physically removed beneath the device. This “via-hole” technique has been successfully used for large area optical modulators [38, 39]. However, for the devices to remain attached to the substrate, the device area must be large enough that the opened hole doesn’t completely undercut the device. Since high-speed HBT’s have dimensions on the order of 10–20 μm and the substrate via-hole etch must etch through 100+ μm , this technique would be very difficult to reliably integrate into an HBT process

Side Illumination

After eliminating top and bottom illumination, the only remaining direction is to bring the control light in through the side. This method overcomes the problem with the short optical interaction lengths. With side illumination, over 90% of the input light will be absorbed in a distance of only 5 μm . Since a *small* HBT has lateral dimensions of 10 μm or greater, the optical interaction length is more than adequate.

Wake *et al.* [68] have reported an edge coupled InP/InGaAs phototransistor in which light is input through the side of the device. To achieve this, the semiconductor wafer was cleaved directly through the device and light was focused right onto the side of the transistor. While this method was successful, it has little practical value for integrated structures. Since the transistor is directly on the edge of the wafer, electrical interconnects are a serious problem and incorporation into a monolithic circuit is nearly impossible.

The ideal solution would be to construct an optical waveguide on the surface of the semiconductor wafer to deliver light to the HBT. This waveguide could safely go under passive microstrip circuit elements so integration with monolithic microwave integrated circuits (MMICs) is possible. This chapter describes the successful implementation of an integrated waveguide-HBT device.

5.2 Direct Optical Access via an Optical Waveguide

I have developed a novel HBT structure which allows direct optical access without compromising the device operation. The employed method is to supply

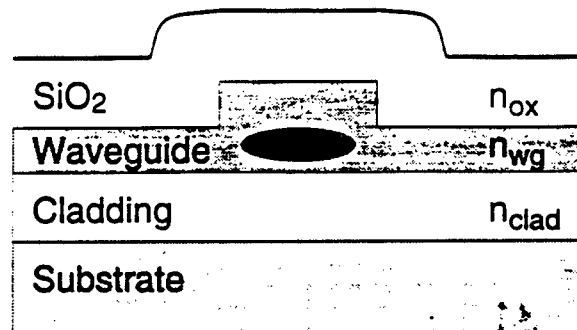
the control light into the bottom of the device through a waveguide that is integrated into the device structure. Figures 5.1 (a) and (b) show diagrams illustrating the waveguide and optical path in the waveguide-HBT structure.

An important feature to notice here is that all of the semiconductor layers for the waveguide are located beneath the device. There are several advantages to this method. Since the waveguide processing is not performed until after fabrication of the HBT device has been completed, standard self-aligned fabrication methods with metal contacts can be used for optimum performance of the HBT device. With the waveguiding layers located beneath the active device layers, the device designer is given full flexibility to implement any desired performance enhancing features into the HBT layer design. The electrical operation of the device is unaffected since the waveguide layers are undoped and their electrical behavior is the same as that of the substrate. One other important feature is that the fabrication of the waveguide only requires one additional mask alignment and etching step. There are no problems with integrating the waveguide into monolithic circuit designs. The only restriction placed on the device design is that the sub-collector layer must be made of a material which is transparent to the light that is intended to be absorbed in the base-collector depletion region.

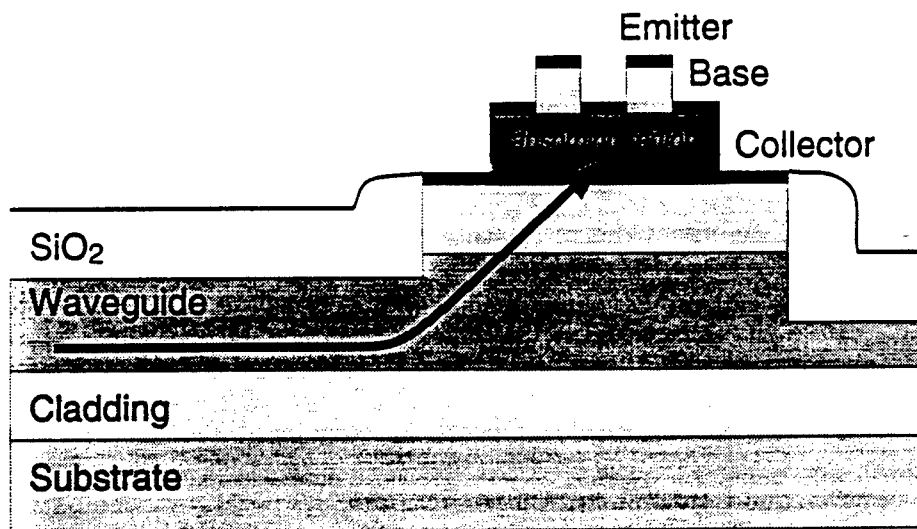
5.3 Waveguide-HBT Design

5.3.1 AlGaAs / GaAs Waveguide-HBT

Design of an AlGaAs/GaAs waveguide-HBT starts with the design of the waveguide. From Fig. 5.2 we see that $\text{Al}_x\text{Ga}_{1-x}\text{As}$ has increasing refractive indices for decreasing values of Al ratio x . To form the integrated waveguide,



(a)



(b)

Figure 5.1: Diagrams of waveguide-HBT showing how an optical waveguide is used to inject light directly into HBT: (a) Cross sectional view of the waveguide showing the location of the optical mode; (b) Side view showing propagation of light from waveguide into device.

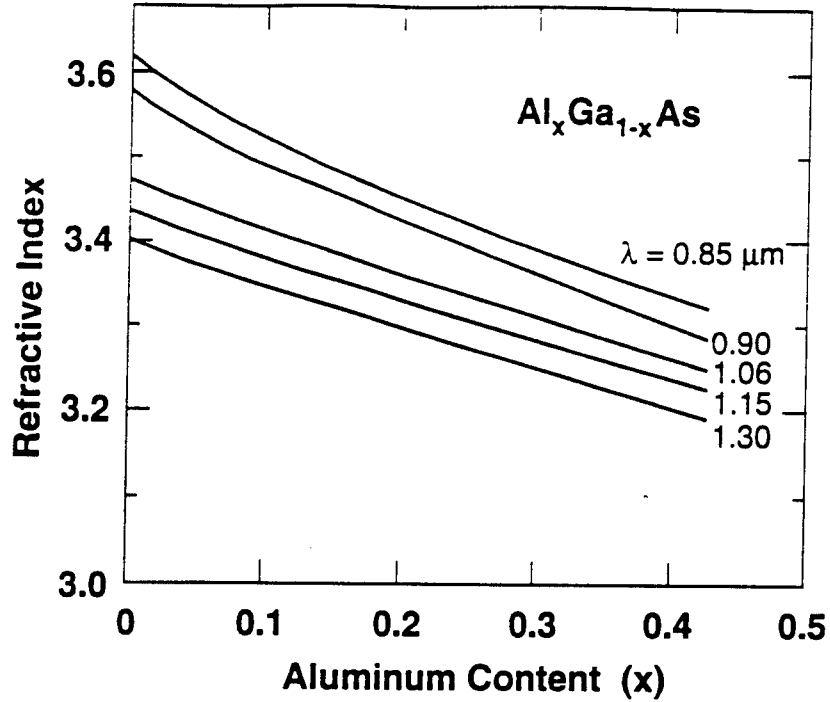


Figure 5.2: Refractive indices of direct bandgap $\text{Al}_x\text{Ga}_{1-x}\text{As}$ at several different wavelengths

$\text{Al}_{0.2}\text{Ga}_{0.8}\text{As}$ with refractive index $n_{wg} = 3.45$ at $\lambda = 850 \text{ nm}$ was chosen for the waveguiding layer. $\text{Al}_{0.4}\text{Ga}_{0.6}\text{As}$ with refractive index $n_{cl} = 3.34$ was chosen for the lower cladding layer. The thicknesses of the waveguide and cladding layers were determined by iteratively performing computer simulations of the optical mode profiles in the waveguide.

Once the waveguide has been designed, the HBT structure is added with only a couple of modification from a standard structure. First, sub-collectors in AlGaAs/GaAs HBTs are commonly made of highly doped GaAs to minimize bulk resistivity and because ohmic contacts to GaAs are superior to contacts made to AlGaAs . Since optical absorption in the sub-collector would prevent the input light from reaching the base-collector depletion region, the sub-collector layer must be made transparent by using a higher bandgap material.

However, the refractive index of the sub-collector cannot be lower than the refractive index of the waveguide or else light will remain confined in the waveguide layer as it travels under the device. $\text{Al}_{0.1}\text{Ga}_{0.9}\text{As}$ satisfies both requirements. It is transparent to light of wavelength $\lambda > 0.8\mu\text{m}$ and its refractive index of $n = 3.52$ is greater than that of the $\text{Al}_{0.2}\text{Ga}_{0.8}\text{As}$ waveguide. A thin layer of n^+ -GaAs is used between the $\text{Al}_{0.1}\text{Ga}_{0.9}\text{As}$ sub-collector and the undoped GaAs collector to allow for the fabrication of low-resistance ohmic contacts.

The remaining layers in the waveguide-HBT design consist of unmodified high-performance HBT layers. The complete design of the AlGaAs/GaAs waveguide-HBT is shown in Table 5.1.

One important aspect of this design is that narrow bandgap absorbing GaAs is only found in the base and undoped collector layers. The sub-collector, waveguide and cladding layers are all higher bandgap AlGaAs. All $\text{Al}_x\text{Ga}_{1-x}\text{As}$ layers have a minimum 10% aluminum content and consequently are transparent to light with wavelengths $\lambda > 800\text{nm}$ while GaAs will absorb light satisfying $\lambda < 870\text{nm}$. Due to the fact that the undoped collector will be completely depleted in normal device operation, light of proper wavelength will be absorbed only in the base and the base-collector depletion region. This is desirable since in this mode of operation, all of the photo-generated holes have the potential to contribute to the HBT's base current.

Optical mode profiles

Optical mode simulations of the waveguide are required to address two important issues. First, it is desirable to propagate single optical modes in

Table 5.1: Layer structure of AlGaAs/GaAs waveguide-HBT

Layer	Composition	Thickness	Doping (cm^{-3})
Cap	GaAs	100nm	$n^+ = 5 \times 10^{18}$
	$\text{Al}_{0.3}\text{Ga}_{0.7}\text{As}$	50nm	$n^+ = 5 \times 10^{18}$
Emitter	$\text{Al}_{0.3}\text{Ga}_{0.7}\text{As}$	100nm	$n = 2 \times 10^{17}$
spacer	GaAs	10nm	undoped
Base	GaAs	80nm	$p^+ = 1 \times 10^{19}$
Collector	GaAs	$0.4\mu\text{m}$	$p = 1 \times 10^{16}$
Contact Layer	GaAs	$0.1\mu\text{m}$	$n^+ = 5 \times 10^{18}$
Sub-Collector	$\text{Al}_{0.1}\text{Ga}_{0.9}\text{As}$	$0.7\mu\text{m}$	$n^+ = 5 \times 10^{18}$
Waveguide	$\text{Al}_{0.2}\text{Ga}_{0.8}\text{As}$	$0.6\mu\text{m}$	undoped
Cladding	$\text{Al}_{0.4}\text{Ga}_{0.6}\text{As}$	$1.0\mu\text{m}$	undoped
Substrate	GaAs		semi-insulating

the waveguide region to minimize signal distortion and provide sufficient optical confinement. Second, since the GaAs substrate below the lower cladding layer is absorbing and has a higher refractive index than the waveguide and cladding layers, it is very important that the guided optical mode have negligible coupling with the substrate. The number of supported optical modes and the mode coupling with the substrate can both be studied with a waveguide optical mode simulator.

A computer simulation of the optical mode profile in the waveguiding region is shown in Figs. 5.3. The position of the optical mode in the waveguide structure is shown in the inset. The waveguide is shown to support a single optical mode. The simulation estimates that the intensity of the optical mode drops five orders of magnitude from the peak value before reaching the substrate. Consequently, substrate losses are expected to be minimal.

Once the waveguide opens up under the HBT device, however, there are five supported optical modes as shown in Fig. 5.4. Since the waveguide layer is no longer bordered by a lower index upper cladding, the light will no longer be constrained in the one layer. Furthermore, since the upper layer is now $\text{Al}_{0.1}\text{Ga}_{0.9}\text{As}$ with a higher refractive index, a ray optics analysis predicts that the light will deflect up into the device absorption regions. A detailed study of the optical coupling from the waveguide into the device will be presented in section 5.4.

5.3.2 InAlAs / InGaAs Waveguide-HBT

The design of an InAlAs/InGaAs waveguide-HBT is somewhat more complicated than the AlGaAs/GaAs design. With the ternary $\text{In}_x\text{Al}_{1-x}\text{As}$ and

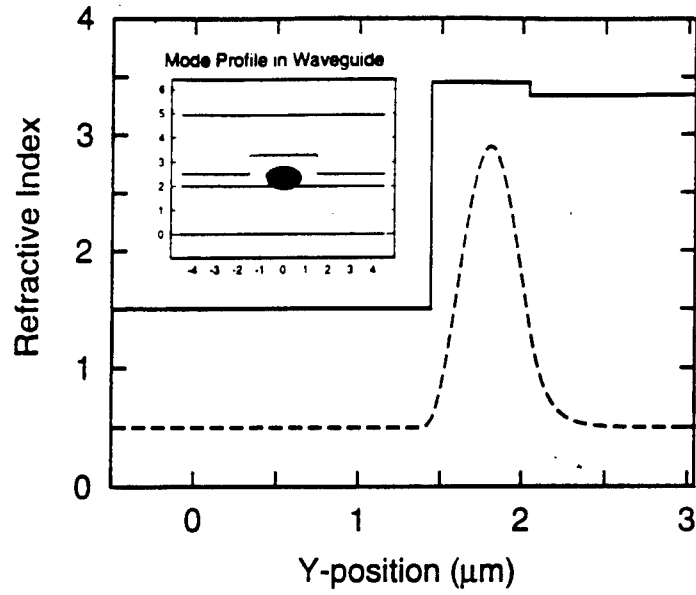


Figure 5.3: Refractive index profile in y-direction of single mode waveguide for direct light injection into AlGaAs/GaAs waveguide-HBT. The corresponding optical mode is also shown. The inset shows the position of the optical mode within the ridge waveguide.

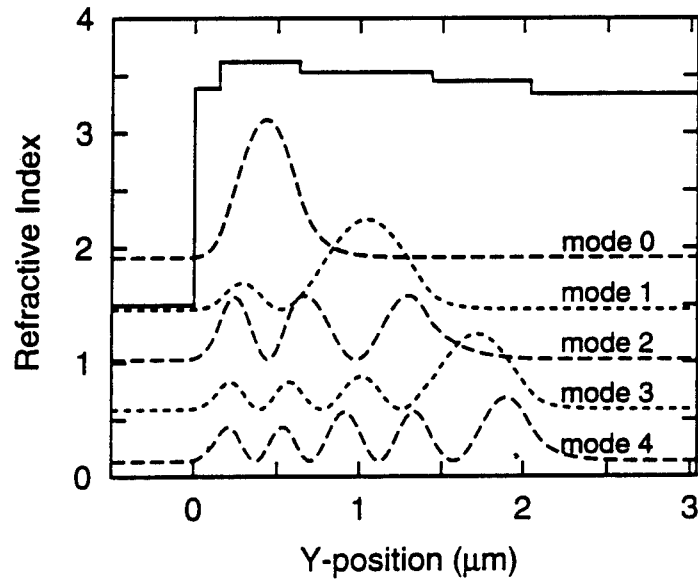


Figure 5.4: Refractive index profile in y-direction after waveguide opens up under AlGaAs/GaAs waveguide-HBT device. This structure supports five optical modes as shown.

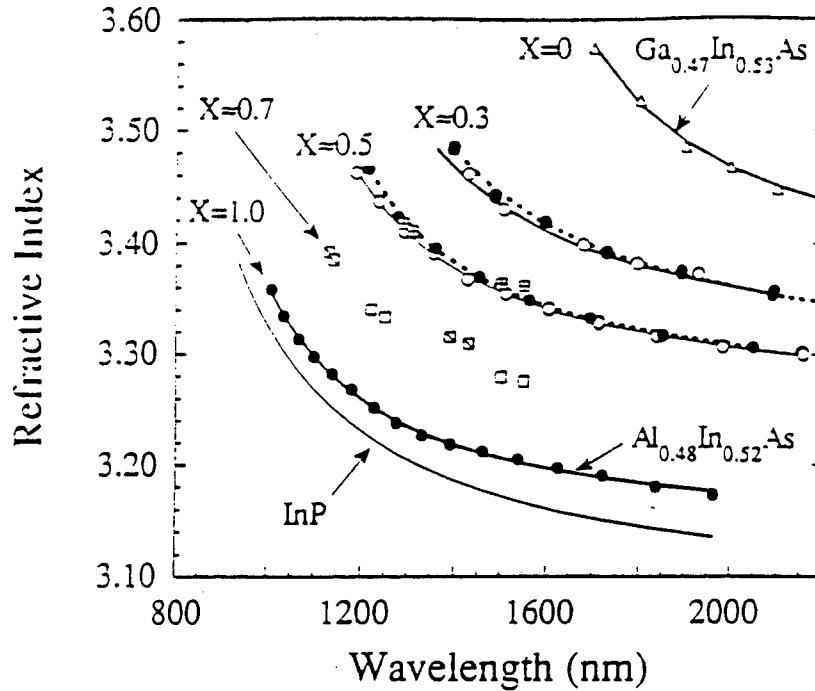


Figure 5.5: Refractive indices of $(\text{In}_{0.52}\text{Al}_{0.48}\text{As})_x(\text{In}_{0.53}\text{Ga}_{0.47}\text{As})_{1-x}$ and InP as a function of wavelength for several different composition ratios (from Mondry *et al.* [69])

In_xGa_{1-x}As systems, there are only two distinct material compositions that are lattice matched to the InP substrate: In_{0.52}Al_{0.48}As and In_{0.53}Ga_{0.47}As. The AlGaAs/GaAs waveguide-HBT required the use of four different materials. Fortunately, the InP substrate is a wide band gap material which is transparent to the light used for the HBT. Therefore, InP can also be used in the optical layer design. From Fig. 5.5 we see that at $\lambda = 1.55 \mu\text{m}$ the refractive indices of In_{0.53}Ga_{0.47}As, In_{0.52}Al_{0.48}As and InP are 3.6, 3.2 and 3.17 respectively.

Since the refractive index of InAlAs is higher than the refractive index of InP, the waveguide can be formed using InAlAs for the waveguide layer with the InP substrate serving as the lower cladding layer. The thickness of the waveguide layer was determined by iteratively performing computer simulations of the optical mode profile until a well defined single optical mode

Table 5.2: Layer structure of InAlAs/InGaAs waveguide-HBT. Note that the InP substrate is used as the lower cladding layer.

Layer	Composition	Thickness	Doping
Cap	In _{0.53} Ga _{0.47} As	100 nm	$n = 1 \times 10^{19}$
	In _{0.52} Al _{0.48} As	50 nm	$n = 1 \times 10^{19}$
Emitter	In _{0.52} Al _{0.48} As	150 nm	$n = 8 \times 10^{17}$
spacer	In _{0.53} Ga _{0.47} As	15 nm	$p = 2 \times 10^{18}$
Base	In _{0.53} Ga _{0.47} As	90 nm	$p = 2 \times 10^{19}$
Collector	In _{0.53} Ga _{0.47} As	600 nm	$n = 1 \times 10^{16}$
Contact Layer	In _{0.53} Ga _{0.47} As	100 nm	$n = 2 \times 10^{18}$
Sub-Collector	In _{0.52} Al _{0.48} As	250 nm	$n = 1 \times 10^{19}$
Waveguide	In _{0.52} Al _{0.48} As	1.4 μm	undoped
Substrate	InP		semi-insulating

was found.

Once the waveguide has been designed, the HBT structure is added with similar modifications as required for the AlGaAs/GaAs structure. InAlAs is used instead of InGaAs for the sub-collector to allow the light to pass through this layer without experiencing absorption. Also, a thin InGaAs layer is added between the InAlAs sub-collector and the undoped InGaAs collector to allow for fabrication of low-resistance ohmic contacts. The remaining layers in the waveguide-HBT design consist of unmodified high-performance HBT layers. The complete design of the InAlAs/InGaAs waveguide-HBT is shown in Table 5.2

A feature that is shared with the AlGaAs/GaAs structure is that the narrow bandgap absorbing InGaAs is only found in the base and undoped collector layers where light absorption is desired. The sub-collector, waveguide and cladding layers are all made of higher bandgap InAlAs and InP. The range of wavelengths which can be used with this device is bounded by the 0.74 eV bandgap of $\text{In}_{.53}\text{Ga}_{.47}\text{As}$ and the 1.35 eV bandgap of InP which encompasses the wavelength range of $0.92\mu\text{m} < \lambda < 1.67\mu\text{m}$. Note, however, that the single mode nature of the waveguide is not guaranteed over this entire wavelength range.

Optical mode profiles

A computer simulation of the optical mode profile in the waveguiding region is shown in Figs. 5.6. The waveguide is shown to support a single optical mode. The confinement of this mode is not as good however. At a depth of $1\mu\text{m}$ into the InP lower cladding, the mode intensity only drops to 10% of its peak value. However, this is acceptable since the InP substrate is thick and does not absorb the guided light. The position of the optical mode in the waveguide structure is shown in the inset.

Once the waveguide opens up under the HBT device there are three supported transverse optical modes as shown in Fig. 5.7. Since the waveguide layer is no longer bordered by a lower index upper cladding, the light will no longer be constrained in the one layer. Unfortunately, since the sub-collector has the same refractive index as the waveguide, the light will not be deflected up as strongly as with the AlGaAs/GaAs design. This prediction is supported by the fact that three optical modes shown in Fig. 5.7 do not overlap as strongly

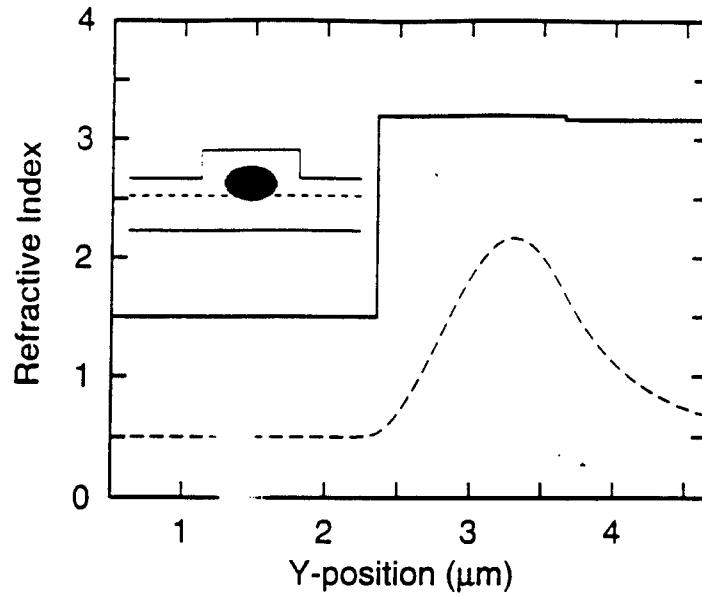


Figure 5.6: Refractive index profile in y-direction of single mode waveguide for direct light injection into InAlAs/InGaAs waveguide-HBT. The corresponding optical mode is also shown. The inset shows the position of the optical mode within the ridge waveguide.

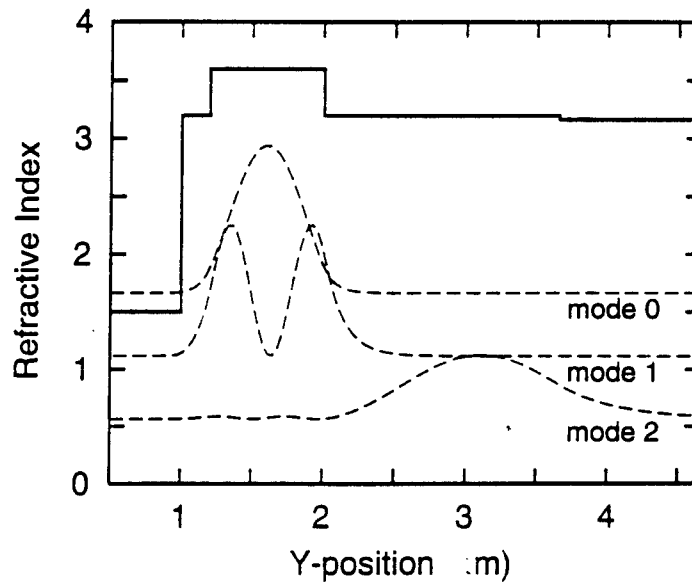


Figure 5.7: Refractive index profile in y-direction after waveguide opens up under InAlAs/InGaAs waveguide-HBT device. This structure supports three optical modes as shown.

as seen in Fig. 5.4. A detailed study of the optical coupling from the waveguide to the device is presented below.

5.4 Simulation of Optical Pulse Propagation

We now study how an optical pulse propagating in the waveguide as a single optical mode couples into the HBT structure. Optimum optical coupling requires that *all* light entering from the waveguide be absorbed in the base-collector depletion region. Since the lateral dimensions of the HBT device are kept small ($< 20\mu\text{m}$) to reduce capacitances and allow high-frequency operation, the input light must be coupled into the collector and be absorbed within a comparable distance. Computer simulations can be used to study the propagation of light through the complex waveguide-HBT structure.

A time-domain optical wave propagation simulator was used to determine how much light will be absorbed within the dimensions of the fabricated waveguide-HBT device [70]. This program was developed by my colleague Dr. Igor Vurgaftman. The program simulates the propagation of a wave packet through a medium of spatially varying refractive indices. The absorption of light in selected regions is also correctly modeled. As such, the program is able to simulate the propagation of light from the waveguide into the transistor and the transit distance required for total absorption.

AlGaAs / GaAs Waveguide-HBT

Figures 5.8 and 5.9 show the simulated propagation of a wave packet that is injected into the AlGaAs/GaAs waveguide-HBT transistor from the single-mode waveguide. The initial mode profile was determined from the simulated

waveguide mode profile shown in Fig. 5.3. As such, it corresponds to the profile of the optical mode immediately before the light leaves the waveguide and enters the region below the HBT. The plots demonstrate the transverse profile of the optical wave as a function of the propagation distance. Although the program simulates the propagation of a two-dimensional wave-packet, the two-dimensional profile is not good for showing time-evolution histories. The displayed profile is an average over the entire wave packet to allow one-dimensional profiles to be displayed.

In Fig. 5.8, absorption in the GaAs base and collector has been disabled so that the mode coupling behavior can be observed. The optical wave is seen to oscillate between the modes characteristic of the initial waveguide and those of the HBT structure. It is interesting to note which of the optical modes from Fig. 5.4 are evident in this simulation. Modes 2, 3 and 4 are easily identified in the propagated mode simulation. This is expected since these three modes have the strongest overlap with the initial mode profile from the waveguide.

Figure 5.9 shows the same simulation but with optical absorption in the GaAs base and collector regions properly modeled. The absorption coefficient used, $\alpha = 5 \times 10^3 \text{ cm}^{-1}$, is the estimated value for absorption of 850 nm light in GaAs [35]. The results show that almost all of the input light is absorbed within a 10 μm distance after entering the device. Thus, this result obtained with the aid of the numerical simulator demonstrates the feasibility of the proposed AlGaAs/GaAs waveguide-HBT.

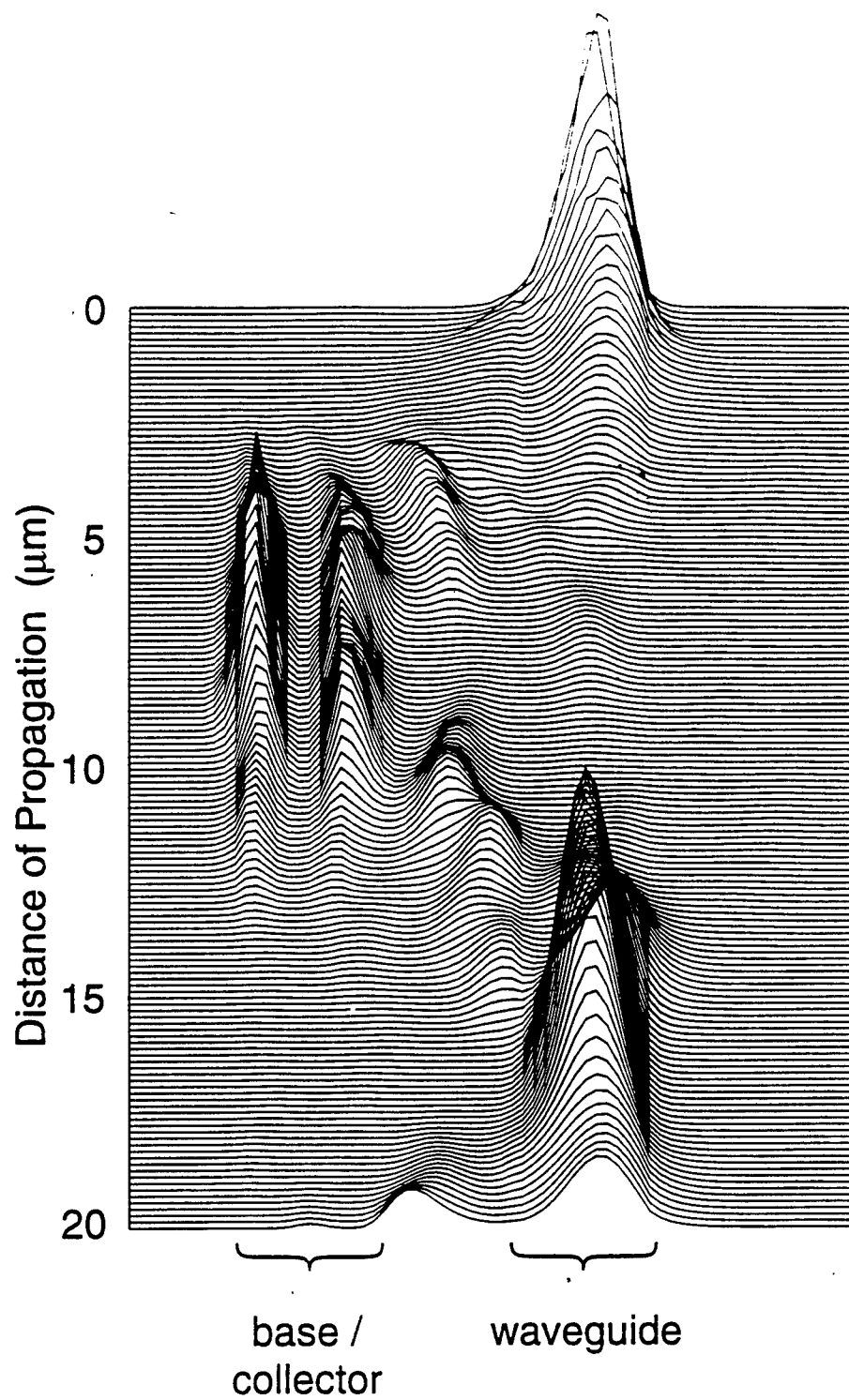


Figure 5.8: Wavepacket propagation in AlGaAs/GaAs waveguide-HBT structure with no simulation optical absorption. The coupling of light between the various waveguide modes is evident.

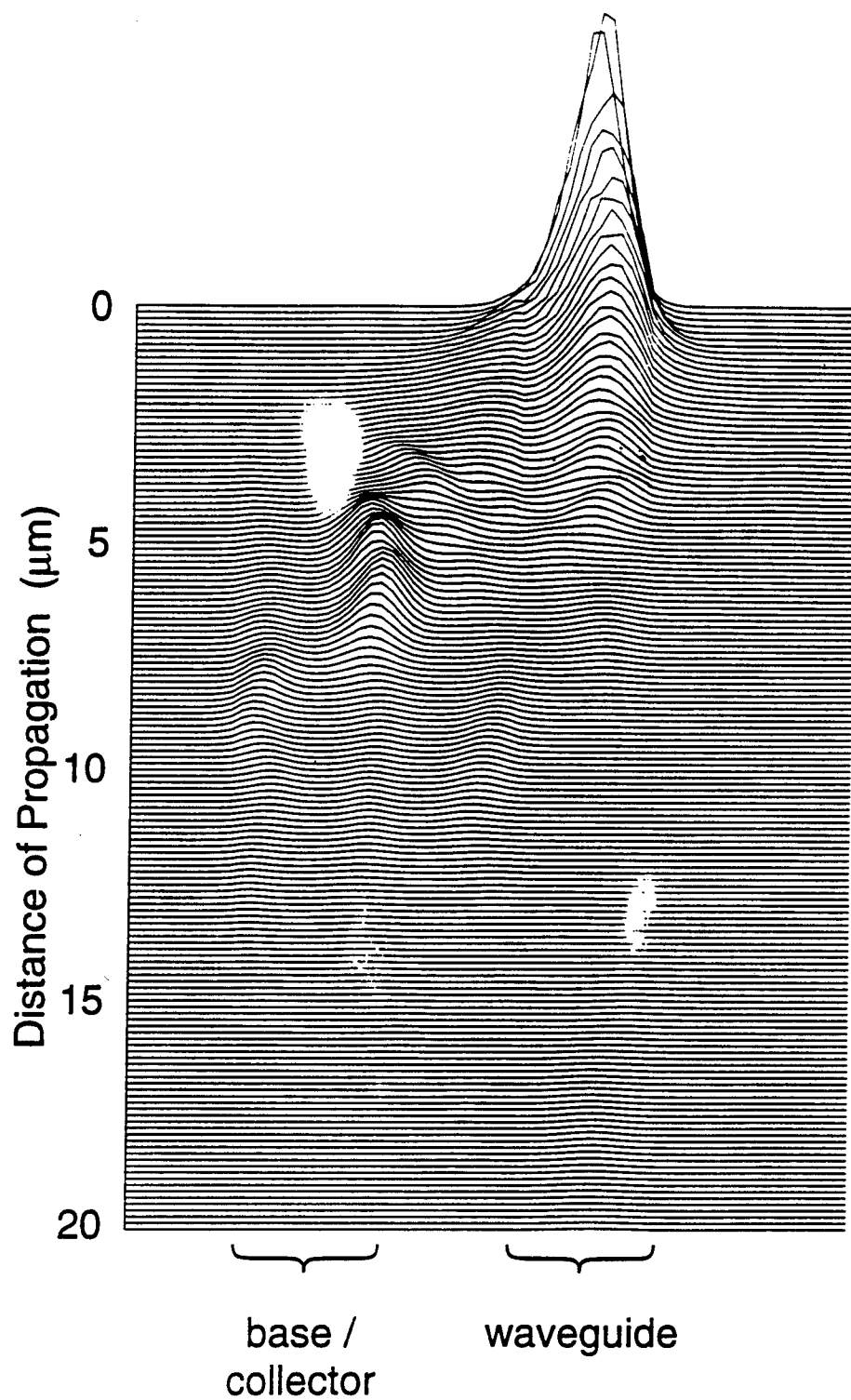


Figure 5.9: Wavepacket propagation with appropriate optical absorption to simulate actual AlGaAs/GaAs waveguide-HBT device. Almost all input light is shown to be absorbed within $10\ \mu\text{m}$ of entering the device.

InAlAs / InGaAs Waveguide-HBT

Figures 5.10 and 5.11 show the simulated propagation of a wave packet that is injected into the InAlAs/InGaAs waveguide-HBT transistor from the single-mode waveguide. The initial mode profile was determined from the simulated waveguide mode profile shown in Fig. 5.6.

In Fig. 5.10, absorption in the InGaAs base and collector has been disabled so that the mode coupling behavior can be observed. Unlike the fast oscillating mode behavior observed in the AlGaAs/GaAs device, here we see a gradual coupling from the waveguide mode into the mode designated "mode 1" in Fig. 5.7. This is the expected result since the overlap between the device and waveguide modes is very small in this device.

Figure 5.11 shows the same simulation but with optical absorption in the InGaAs base and collector regions properly modeled. The absorption coefficient used, $\alpha = 4 \times 10^3 \text{ cm}^{-1}$, is the estimated value for absorption of $1.55 \mu\text{m}$ light in InGaAs [35]. The results show that 56% of the input light is absorbed over the $15 \mu\text{m}$ interaction length of the actual device. This simulation shows that the proposed InAlAs/InGaAs waveguide-HBT device is also suitable for optical control applications.

5.5 Fabrication and Performance of InAlAs / In-GaAs Waveguide-HBT

The InAlAs/InGaAs waveguide-HBT structure as shown in Table 5.2 was grown by molecular beam epitaxy (MBE). Self-aligned HBTs were fabricated using the process described in section 2.5. A scanning electron micrograph of the fabricated waveguide-HBT is shown in Fig. 5.12. The $2 \mu\text{m}$ optical

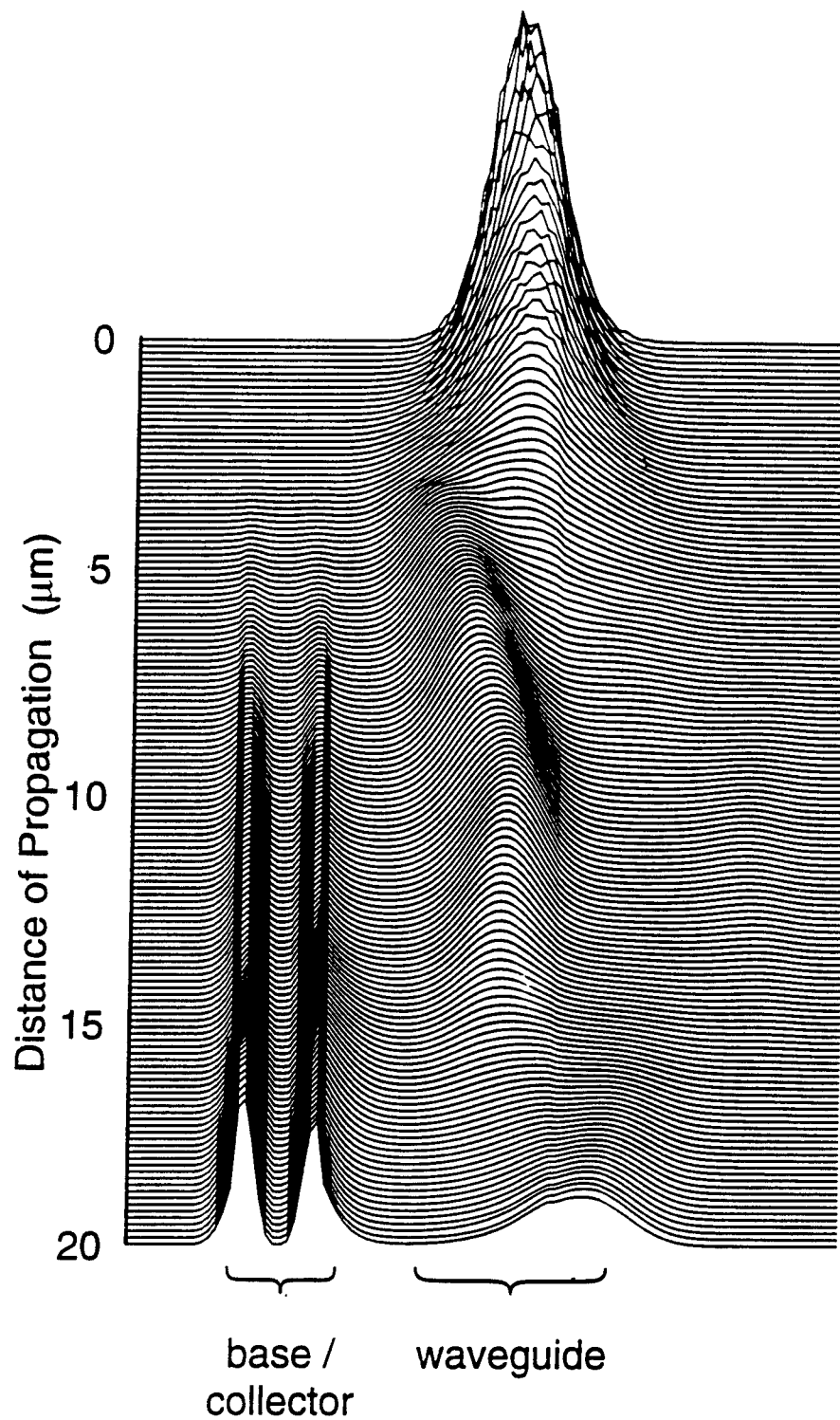


Figure 5.10: Wavepacket propagation in InAlAs/InGaAs waveguide-HBT structure with no simulation optical absorption. The coupling of light between the various waveguide modes is not as efficient as structures having a sub-collector layer with an intermediate refractive index.

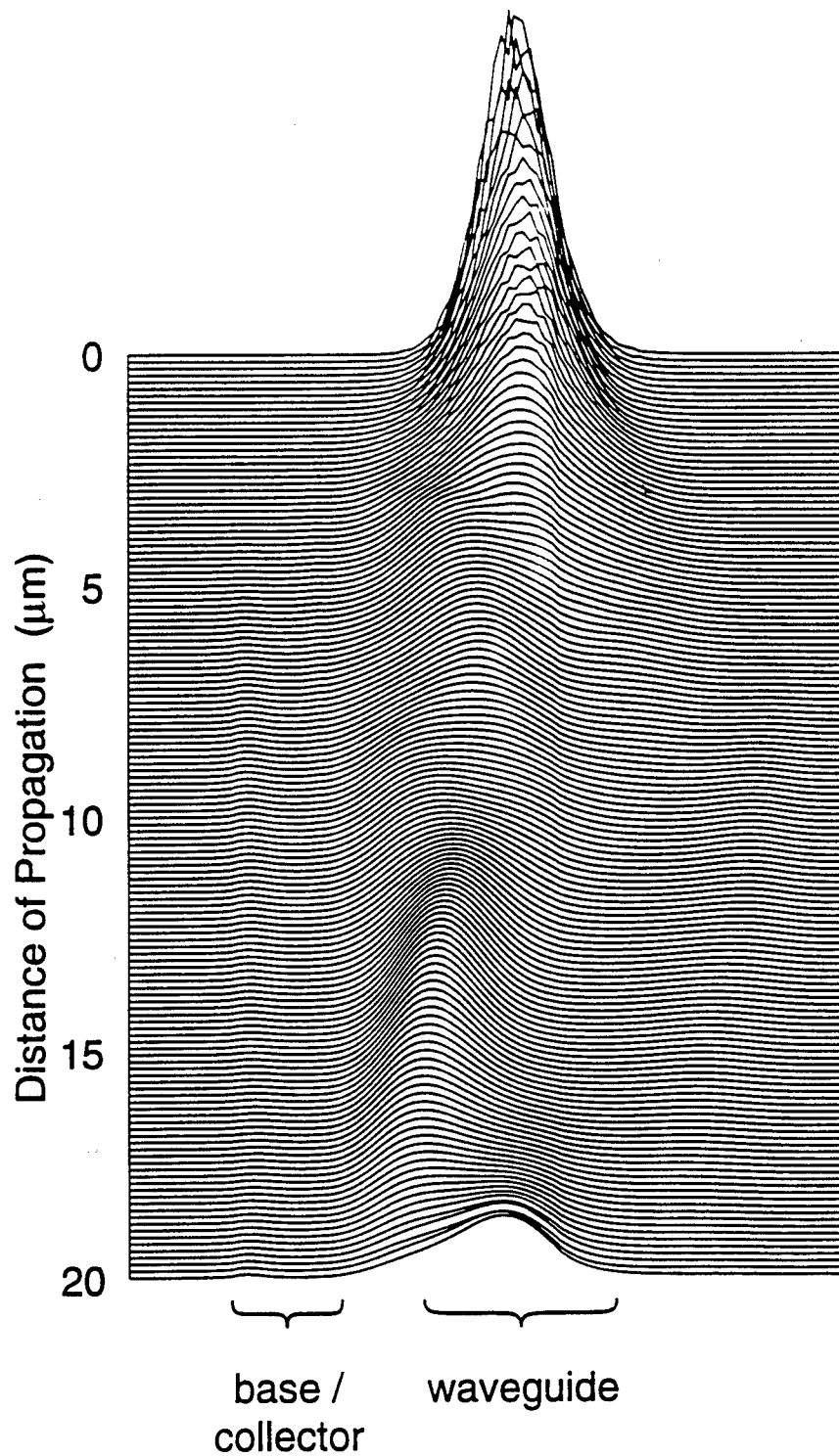


Figure 5.11: Wavepacket propagation with appropriate optical absorption to simulate actual InAlAs/InGaAs waveguide-HBT device. 56% of the input light is shown to be absorbed over the 15 μm interaction length of the actual device.

waveguide feeding directly under the $5\mu\text{m} \times 5\mu\text{m}$ square emitter is clearly visible. A close up the cleaved waveguide facet is shown in Fig. 5.13. Here we see the etch profile of the $0.8\mu\text{m}$ phosphoric acid etch and the semi-conformal oxide deposition.

DC and RF Characteristics

DC characterization was performed using an HP 4145 Semiconductor Parameter Analyzer. Common-emitter DC measurements showed maximum current gains (h_{fe}) of 15-25 and junction ideality factors of 1.04 and 1.78 for the base-collector and emitter-base junctions, respectively.

Microwave performance of the devices was measured from 50 MHz – 25.5 GHz using an HP 8510 network analyzer. The short circuit current gain (h_{21}) and the maximum available power gain (G_{max}) were computed from the measured S-parameters and are shown in Fig. 5.14. At bias conditions $I_C = 5.5\text{ mA}$ and $V_{CE} = 2\text{ V}$, the current gain cutoff frequency (f_T) and maximum frequency of oscillation (f_{max}) were found to be 32 and 48 GHz respectively. This represents a significant improvement over the performance of previous HBTs with through-the-top optical input. Figure 5.15 shows the dependence of the cutoff frequencies on collector current I_C .

It is fully expected that the cutoff frequencies can be increased into the 100 GHz range with further material and process development. The MBE grown layer structures used for these devices had a non-ideal surface morphology due to roughness in the growth interface after growth of the thick InAlAs waveguide layer.

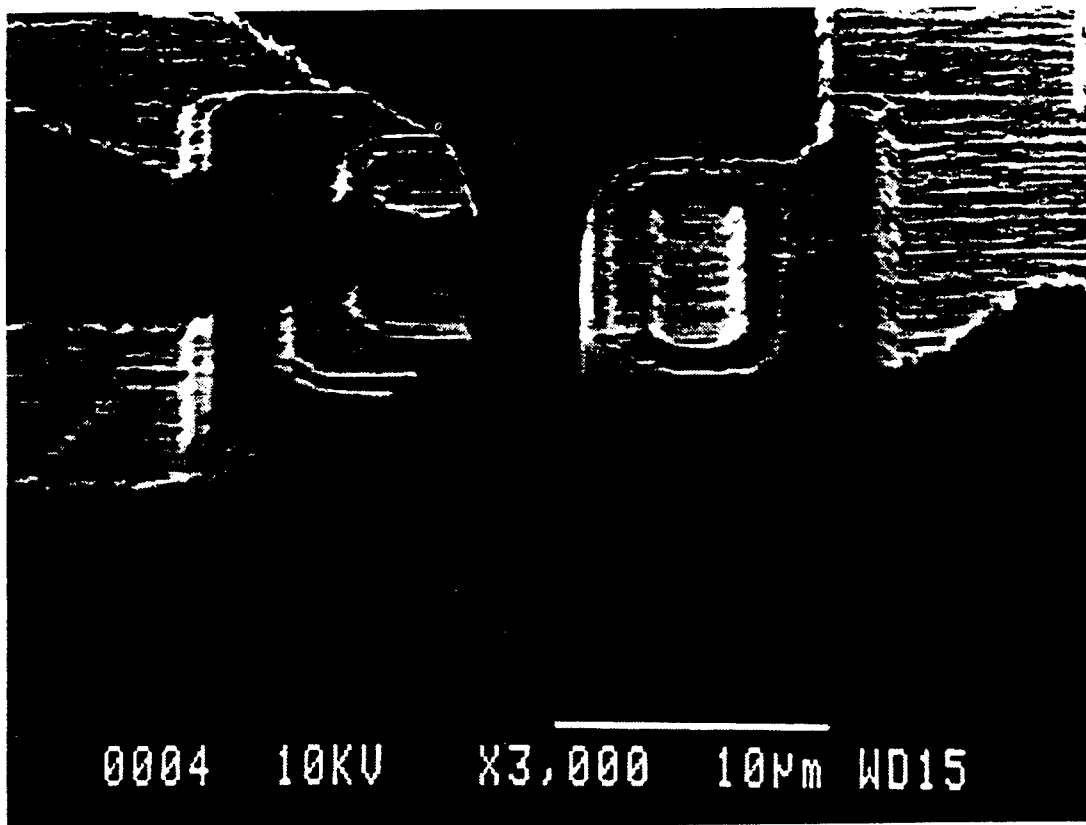


Figure 5.12: Scanning electron micrograph of fabricated waveguide-HBT device. The emitter area is $5\mu\text{m} \times 5\mu\text{m}$ with a total optical interaction length of $15\mu\text{m}$.

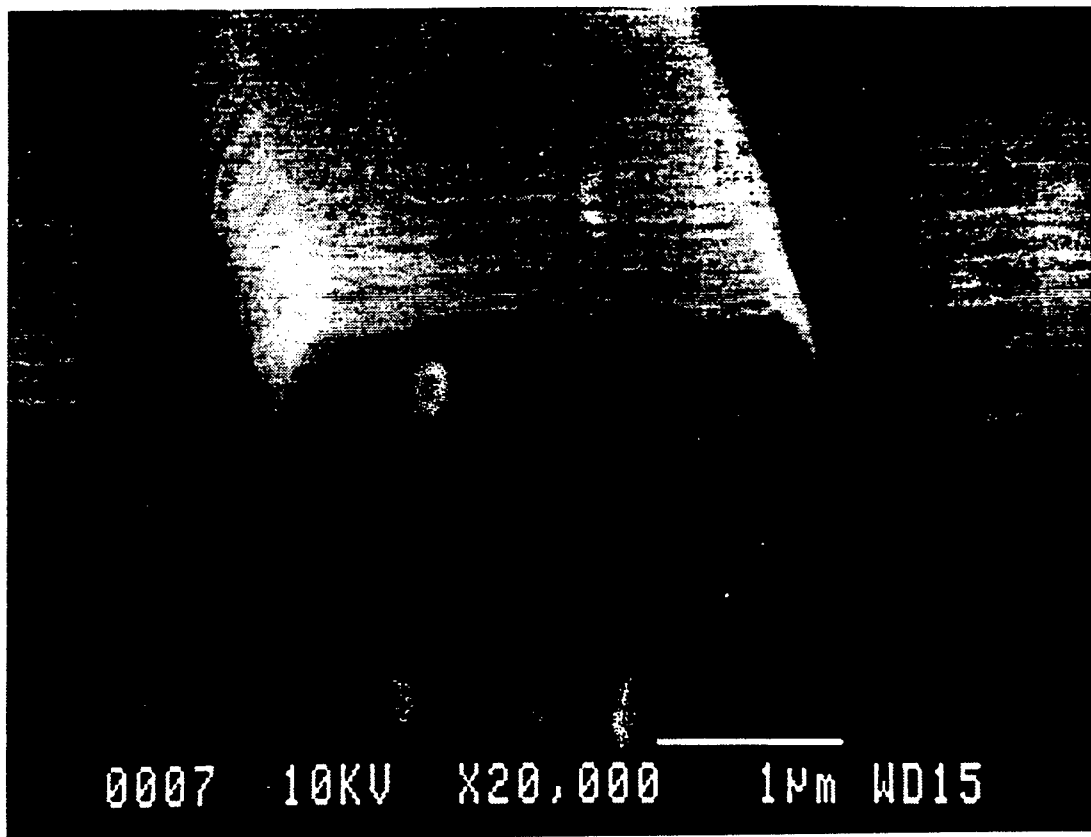


Figure 5.13: Scanning electron micrograph of cleaved facet showing cross section of the integrated waveguide. The ridge width is seen to be $2\text{ }\mu\text{m}$.

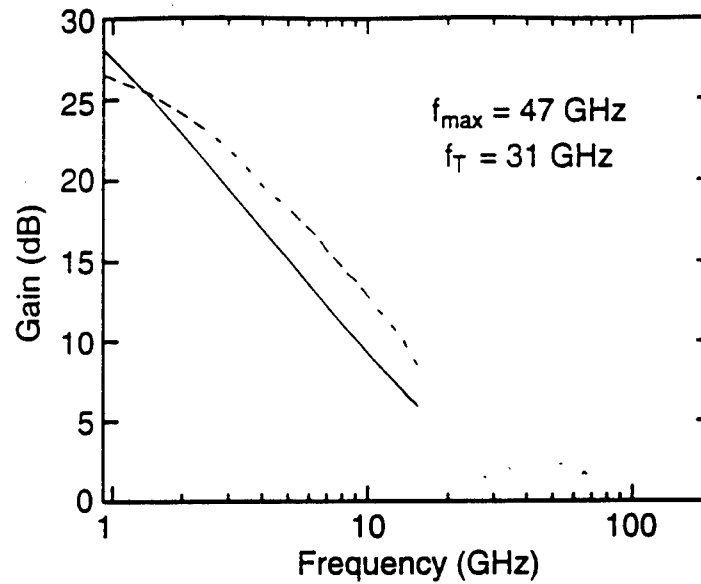


Figure 5.14: Measured current gain h_{21} (—) and power gain G_{max} (- - -) of InAlAs/InGaAs waveguide-HBT. At bias conditions $I_C = 5.5$ mA and $V_{CE} = 2$ V, the current gain cutoff frequency (f_T) and maximum frequency of oscillation (f_{max}) were found to be 32 and 48 GHz respectively.

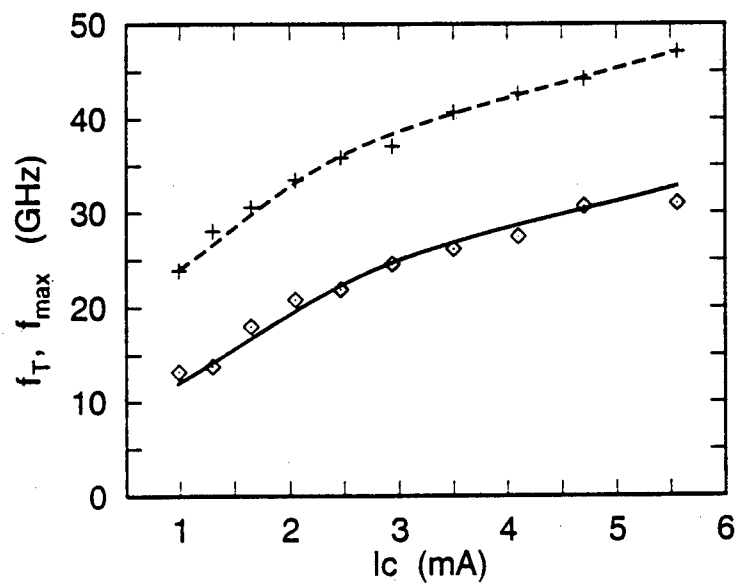


Figure 5.15: f_T (\diamond) and f_{max} (+) as a function of collector current I_C for InAlAs/InGaAs waveguide-HBT

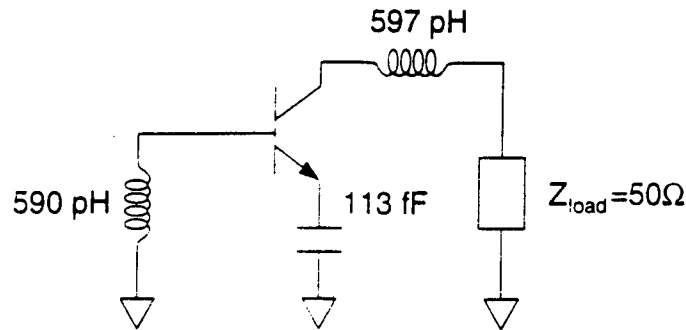


Figure 5.16: Preliminary oscillator design using ideal lumped elements

5.6 OEIC/MMIC Oscillators

With an f_{max} of 48 GHz, these transistors are well suited for use in microwave oscillators operating at frequencies up to 15 GHz. The program *Libra* by the software company EEsof was used to assist with oscillator design. The design goals were the same as those listed in Eqns. 3.12–3.14. The optimization of oscillator “Q”-factor (Eqn. 3.15) was not a design goal because higher Qs lead to lower injection locking ranges. The preliminary design consisted of ideal lumped elements for the feedback network. This oscillator is shown in Fig. 5.16.

The ideal capacitor and inductors were then replaced with monolithic circuit elements. The small signal grounds from Fig. 5.16 were replaced by bias-tee networks. Planar rectangular spiral inductors and thin film capacitors with initial reactances matching the ideal elements were first used. Using known parameters for metal conductivity, oxide dielectric constant and thickness, *Libra* was able to estimate the parasitic resistances and reactances of the actual devices. All the device dimensions were then tuned for optimum oscillation behavior. Appendix B shows the *Libra* circuit file used for designing

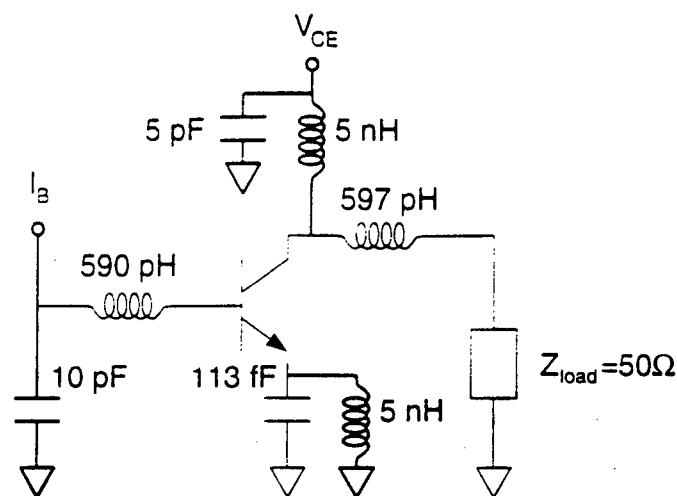


Figure 5.17: Final oscillator design using modeled microstrip elements and bias-tee networks. Bias-tee elements are drawn in bold lines.

the oscillator. The final oscillator circuit is shown in Fig. 5.17

Fabrication of the MMIC oscillators follows the same process sequence as for the HBT test devices. No additional mask steps were required. While an air bridge process is commonly used for connecting to the center spiral of a planar inductor, my process made use of a “sub-interconnect” metalization for this purpose. This sub-interconnect is from the same metalization step as the collector ohmic contact. Before depositing the collector contact, the isolation mesa and waveguide etches are performed. Then the collector metalization is deposited onto both the collector contact layer and on the substrate. Where the collector metalization is deposited onto the semi-insulating substrate, it forms the sub-interconnect metalization. In addition to forming the inductor bridges with the sub-interconnect, the thin film capacitors were formed using the sub-interconnect and interconnect metals as the parallel plates of the capacitor. The pad oxide doubled as the dielectric layer. A microphotograph of the fabricated MMIC oscillator is shown in Fig. 5.18. Figure 5.19 shows a

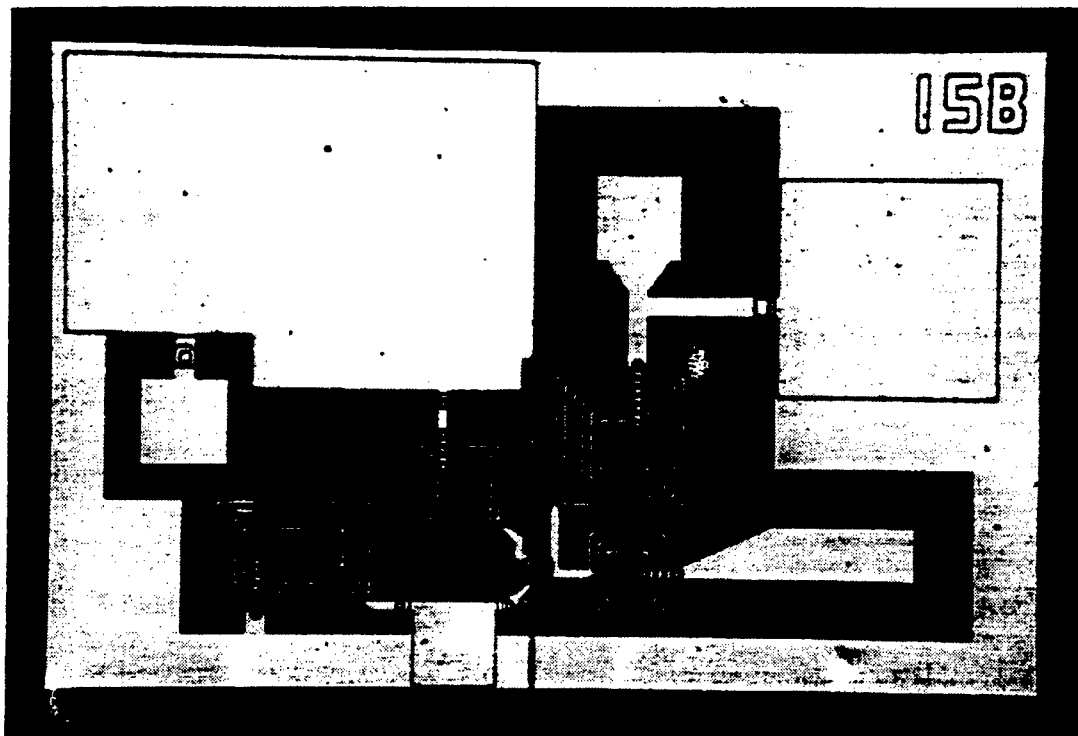


Figure 5.18: Microphotograph of fabricated 13.9 GHz waveguide-HBT oscillator. The optical waveguide can be seen in the lower center of the image.

close up view of one of the rectangular spiral inductors used in the circuit.

5.6.1 Oscillator Characteristics

An HP 8593A Spectrum Analyzer with a bandwidth of 9 KHz to 22 GHz was used to monitor the spectral characteristics of the oscillator's output. A Tektronics microwave probe was used to connect the spectrum analyzer to the oscillator circuit. Under bias condition of $I_C = 5$ mA and $V_{CE} = 2$ V, the oscillator produced oscillations at 13.9 GHz with a maximum output power of -4 dBm (0.4 mW). Since the DC power supplied to the modulator was 10 mW, this result corresponds to a DC-to-RF conversion efficiency of $\eta = \frac{P_{RF}}{P_{DC}} = 4\%$. Figure 5.20 (a) shows the output spectrum of the MMIC waveguide-HBT oscillator.

5.6.2 Optical Control Experiments

Optical control experiments were performed using an HP 38420A Light-wave Component Analyzer. The HP 38420A is capable of delivering 250 μ W of 1.55 μ m optical power through connectorized single-mode optical fibers. The output light can be modulated at frequencies up to 20 GHz.

To couple the control light into the waveguide-HBT oscillator, a bare cleaved fiber end was butt-coupled to the cleaved waveguide facet of the monolithic oscillator. Photoabsorption measurements showed that about 30% of the light available from the fiber was successfully absorbed in the HBT. This is lower than the predicted efficiency of 56% from the optical pulse propagation simulator due to coupling losses between the fiber and the waveguide.

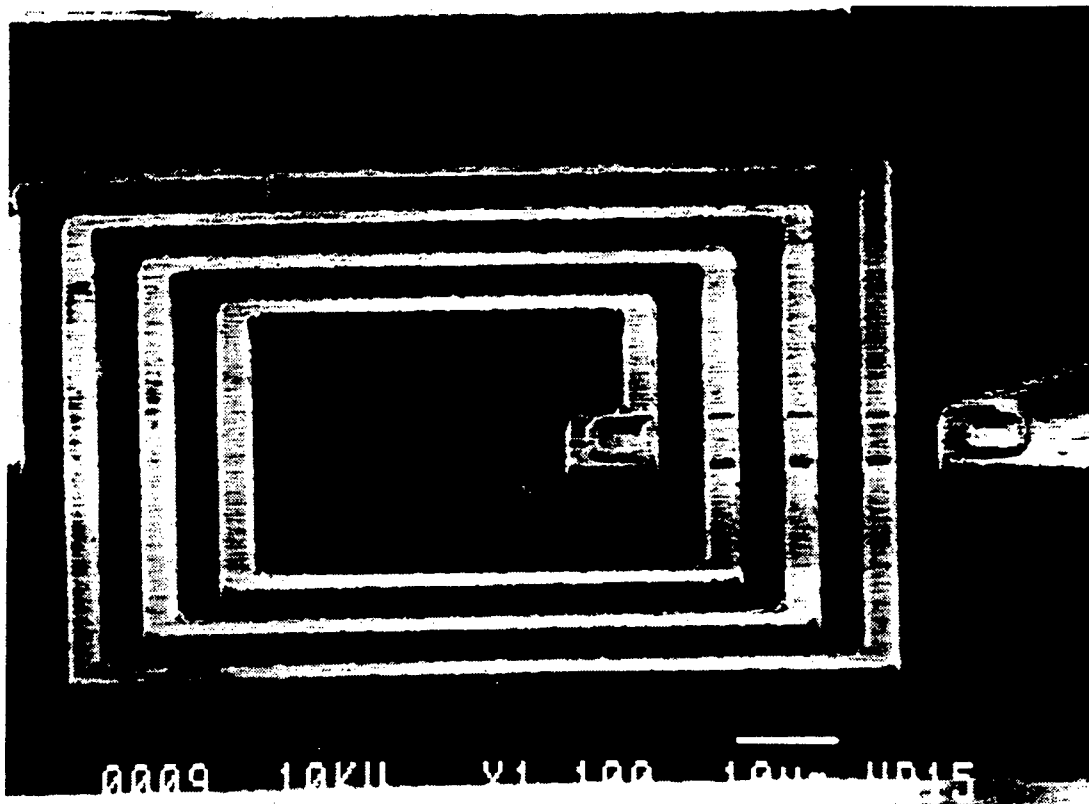


Figure 5.19: Scanning electron micrograph showing close-up of rectangular spiral inductor. A sub-interconnect metal was used to connect to the center spiral instead of a more processing intensive air-bridge process.

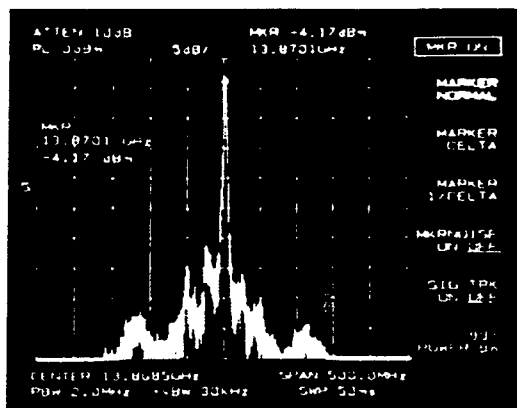
Optical Tuning

Optical tuning was observed when the input optical power was changed. When the available optical power was changed from 0 to 200 μW , a shift in the free-running oscillation frequency of -100 MHz was observed. Figure 5.20 (b) displays the spectral profiles of the oscillator with and without light which clearly shows the optical tuning effect. This shift to lower frequencies is consistent with the expected increase in base-emitter junction capacitance as the current through that forward biased junction is increased. The increase in capacitance causes a lowering of the resonant frequency of the *RLC* loop created by the base-emitter junction and the feedback network.

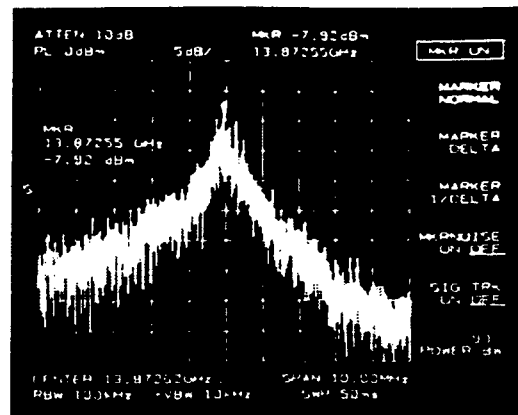
Optical Injection Locking

To perform optical injection locking experiments, the HP 38420A Lightwave Component Analyzer was configured to modulate its output light. The modulation frequency was supplied to the lightwave component analyzer from a HP 8350 sweep oscillator with 10 MHz to 50 GHz output capability. When the modulated optical signal was tuned to frequencies close to the oscillator's free running frequency, multiple sidebands were observed similar to those pictured in Fig. 3.8. When the modulated optical signal was tuned within the injection locking range, the output spectrum stabilized and oscillator phase noise was reduced. The output spectrum of the oscillator under unlocked and locked conditions is shown in Figs. 5.20 (c) and (d). An optical injection locking range of 0.5 MHz was observed.

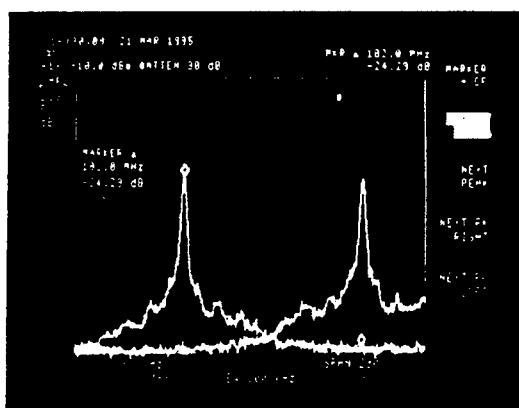
When the modulated optical signal was tuned to a frequency far away from the oscillation peak, the optically generated signal could be clearly viewed on



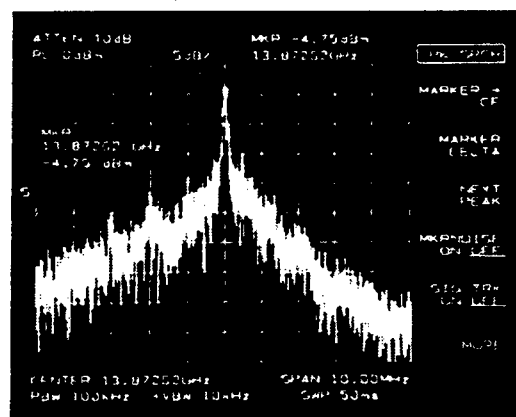
(a)



(c)



(b)



(d)

Figure 5.20: Output spectra of MMIC waveguide-HBT oscillator: (a) Output spectrum of free running oscillator; (b) Frequency shift with and without light shows optical tuning range; (c) Narrow spectrum view of oscillation peak of free-running oscillator; (d) Narrow spectrum view of optically injection locked oscillator.

the spectrum analyzer. In this manner, the optically generated microwave power was measured to be -61 dBm. This is a very small power level and serves to explain the small optical injection locking range. By using Adler's equation, we can estimate the quality factor of the oscillator as follows:

$$\omega_{max} = \frac{\omega_o}{2Q} \sqrt{\frac{P_{inj}}{P_0}}, \quad (5.1)$$

$$0.5 \text{ MHz} = \frac{13.9 \text{ GHz}}{2Q} \sqrt{\frac{0.8 \mu\text{W}}{0.4 \text{ mW}}}, \quad (5.2)$$

and therefore

$$Q = 20. \quad (5.3)$$

The fact that this quality factor is lower than those measured for the MQW-HBT and ITO-HBT oscillators indicates that the intended low- Q design was successful.

5.7 Summary

A HBT technology with direct optical input while still using an unmodified high-performance HBT layer structure and fabrication layout has been described. By incorporating a waveguide into the semiconductor layers directly below the HBT, problems associated with through-the-top or backside device illumination are avoided. The input light is delivered into the HBT's absorption region by deflection out of the waveguide layers and into the active device layers. Computer simulations of the optical mode profiles and the propagation of optical pulses in the waveguide-HBT were used to validate the optical design.

Fabricated InAlAs/InGaAs waveguide-HBT devices exhibited cutoff frequencies of $f_T = 32$ GHz and $f_{max} = 48$ GHz which represents a significant

improvement over the performance of previous HBTs with through-the-top optical input. Optically controlled MMIC oscillators operating at 13.9 GHz were designed and fabricated using these devices. With further material and process development, it is fully expected that the device's cutoff frequencies can be increased into the 100 GHz range.

CHAPTER VI

OPTICAL MODULATORS BASED ON THE BLOCKADED RESERVOIR AND QUANTUM WELL ELECTRON TRANSFER STRUCTURE

6.1 Introduction

Systems utilizing optical fibers for signal transmission and distribution require optical modulators for converting information from electrical into optical form. The required characteristics of the optical modulators vary depending on the system in question. In digital systems, the primary requirement for modulators is fast on-off and off-on switching times. For these applications, almost any fast optical modulator with good contrast ratio can be used. In microwave and millimeter wave systems, however, the characteristics of the modulator become much more critical to system operation. In addition to having a high response speed and large modulation depth, the modulator should ideally have a linear electrical to optical response characteristic in order for the spectral purity of the microwave signal to remain unchanged after optical transmission.

At wavelengths well below the semiconductor band gap, electro-optic modulators utilizing the Pockels effect have been used to achieve modulation band-

widths larger than 20 GHz [71, 72]. These modulators utilize a weak electro-optic effect so long devices are required and traveling wave techniques must be used to velocity match the electrical and optical waves. Unfortunately, the traveling wave structure imposes several practical limitations on modulation response at very high speeds. In addition, the transmission of a cross-polarized electro-optic modulator has a \sin^2 dependence on applied voltage. A semi-linear modulation can only be achieved by biasing the modulator near the 50% transmittance point and using small signal modulation. However, in addition to not being truly linear, this method restricts the available modulation depth.

Because they offer a large modulation depth and avoid the problems associated with the traveling wave structure, electro-absorption modulators operating near the semiconductor band gap have been a topic of intense research. Electro-absorption modulators can be made much shorter than electro-optic modulators due to their strong optical absorption capabilities. In fact, modulators are generally made small enough that they can be regarded as a lumped capacitance. With sub-picofarad device capacitances, modulation bandwidths as large as 40 GHz have been reported [73]. Electro-absorption modulators also have the advantages of requiring a smaller drive power than electro-optic modulators and they have the potential for integration with other opto-electronic devices such as semiconductor lasers.

Electro-absorption modulators have been demonstrated using the Franz-Keldysh effect [74], and the quantum confined Stark effect (QCSE) [73, 75]. However, With these near-band-edge modulators, high frequency response can be slowed by fundamental processes associated with the photo-excitation of free carriers such as carrier recombination time and hole trapping [76, 77, 78].

In addition, modulators relying on the shifting of the absorption edge exhibit a quadratic electrical to optical transfer function and therefore are not entirely suitable for use as a distortion free modulator.

In this chapter, I present the results of my study of a relatively new type of semiconductor waveguide modulator based on the blockaded reservoir and quantum well electron transfer (BRAQWET) structure.

6.2 The Blockaded Reservoir and Quantum Well Electron Transfer Structure

In a BRAQWET modulator, strong electroabsorption and electrorefraction are provided by a synchronous, voltage-controlled transfer of electrons into a quantum well [79]. Diagrams of the BRAQWET structure at several applied bias levels are shown in Fig. 6.1. The key regions of the structure are the electron reservoir, the quantum well and the planar doped barrier (PDB). The planar doped barrier provides a convenient method of positioning the quantum well energy levels relative to the electron reservoir. By changing the bias across the device, the bound states of the quantum well are dipped above and below the fermi level fixed by the electron reservoir. These states are then filled or emptied by a transfer of electrons from the reservoir region. Optical modulation is achieved as the free carriers screen the Coulombic interaction between the electron and hole in the quantum well. This causes a weakening of the exciton binding energy and reduces the oscillator strength of the exciton [36]. Since the electron transfer across the spacer is a very fast process, very high modulation speeds are expected with this device. It has been found [80, 81] that BRAQWET modulators are free from the speed limitations im-

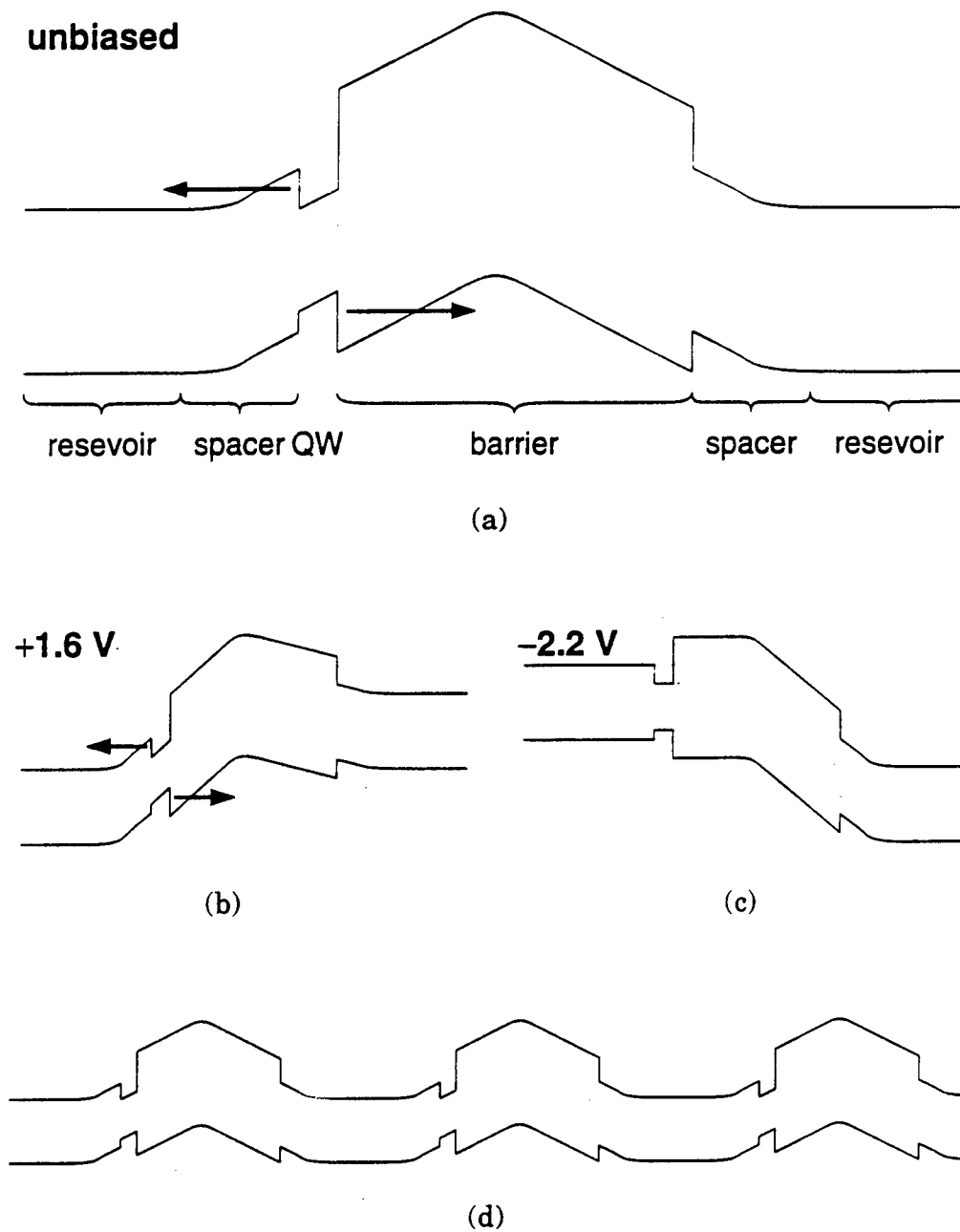


Figure 6.1: Band diagrams of the BRAQWET structure: (a) Unbiased device; (b) Under positive bias, absorption is maximized as electrons are swept out of well by electric field; (c) Under negative bias absorption is quenched due to free-electron screening of the excitonic states in the quantum well; (d) BRAQWET structure allows multiple periods to be stacked for increased modulation efficiency.

posed by recombination times and other carrier dynamics that are present in current injection band filling devices [82].

The PDBs integrated into the BRAQWET structure prevent external current flow so the devices will consume little DC power. In theory, this feature also allows several structures to be stacked (see Fig. 6.1 (d)) to improve modulation performance since field profiles will remain constant from device to device. However, as will be shown later, for amplitude modulators only the top BRAQWET structure is effective.

The modulation characteristics of the BRAQWET modulator are determined by examining the excitonic bleaching effects of free electrons in the quantum well. The electron density in a two-dimensional system is determined by integrating the product of the two-dimensional density of states, $N_{2D}(E)$ and the Fermi function, $f(E)$, which are given as

$$N_{2D}(E) = \frac{m^*}{\pi\hbar^2}, \quad (6.1)$$

$$f(E) = \frac{1}{1 + e^{(E-E_F)/kT}}. \quad (6.2)$$

The electron density is therefore

$$n = \int_{E_1}^{\infty} f(E) N_{2D}(E) dE \quad (6.3)$$

$$n = \int_{E_1}^{\infty} \frac{m^*/\pi\hbar^2}{1 + e^{(E-E_F)/kT}} dE. \quad (6.4)$$

where E_1 is the energy level of the first bound electronic state in the quantum well. The assumption has been made that there is no electronic filling of the second bound state. After substituting $E' = \frac{E-E_F}{kT}$ we proceed as follows:

$$n = \frac{kTm^*}{\pi\hbar^2} \int_{\frac{E_1-E_F}{kT}}^{\infty} \frac{1}{1 + e^{E'}} dE', \quad (6.5)$$

$$n = \frac{kTm^*}{\pi\hbar^2} \left[\ln \frac{e^{E'}}{1 + e^{E'}} \right]_{\frac{E_1 - E_F}{kT}}^{\infty} \quad (6.6)$$

$$n = -\frac{kTm^*}{\pi\hbar^2} \ln \frac{e^{(E_1 - E_F)/kT}}{1 + e^{(E_1 - E_F)/kT}} \quad (6.7)$$

When the energy of the quantum well bound state is below the Fermi energy ($E_1 < E_F$), Eqn 6.7 can be approximated by the linear function

$$n = \frac{m^*}{\pi\hbar^2} (E_1 - E_F) \quad (6.8)$$

Due to the nature of the PDB diode structure which is used to shift the height of the quantum well relative to the electron reservoir, the offset in energy levels ($E_1 - E_F$) and, consequently, the electron density n will show linear relationships to the applied voltage [83].

The change in the absorption coefficient due to free carrier screening of excitons in the quantum well was studied theoretically by Jaffe in 1989 [84]. The band-to-band absorption coefficient in a quantum well was shown to be

$$\alpha_{bb}(\omega) = \frac{q^2 E_p}{2t_W \epsilon \hbar (c/n) \hbar \omega} \sum_{c,v} g |\langle \phi_c | \phi_v \rangle|^2 \frac{\mu_{c,v}}{m_o} \times u(\hbar\omega - E_{c,v})(1 - f_e)(1 - f_h) \quad (6.9)$$

and the excitonic contribution to the absorption coefficient is

$$\alpha_{ex}(\omega) = \frac{2q^2 E_p \sqrt{\ln 2}}{m_o t_W \epsilon (c/n) \sqrt{\pi} \omega} \sum_{c,v} \frac{g}{(a_{c,v}^{ex})^2 \sigma} |\langle \phi_c | \phi_v \rangle|^2 \times \exp\left(-\frac{(\hbar\omega - E_{c,v}^{ex})^2 \ln 2}{\sigma^2}\right) (1 - f_{ex}), \quad (6.10)$$

where t_W is the well thickness, ϵ and n are the dielectric constant and refractive index of the material, respectively, $\mu_{c,v}$ and $E_{c,v}$ are the reduced mass and the energy of the transition from valance state v to conduction state c , and $u(E)$ is the unit step function. E_p is an energy associated with the optical matrix

elements of the system. g is the square of the coefficient of the reduced matrix element and accounts for polarization and valence band composition. f_e , f_h and f_{ex} are the Fermi filling factors of the available electron, hole, and excitonic states. The total absorption coefficient is the sum of the band to band and excitonic absorption coefficients or

$$\alpha_{total} = \alpha_{bb} + \alpha_{ex} . \quad (6.11)$$

In the BRAQWET modulator's quantum well, f_e and f_{ex} will be directly proportional to the electron density n given in Eqn. 6.7 while f_h will be approximately zero. Therefore, when the energy of the quantum well bound state is below the Fermi energy ($E_1 < E_F$) such that n can be approximated by the linear function in Eqn. 6.8, the total optical absorption coefficient α_{total} will also have a linear relationship to the shift in $(E_1 - E_F)$ caused by the operation of the PDB diode. The combination of these effects results in a structure which has a linear relationship between the applied bias voltage and the optical absorption coefficient, or

$$\alpha(V) = \alpha_o + \frac{\delta\alpha}{\delta V} V , \quad (6.12)$$

where α_o is the zero bias absorption coefficient and $\frac{\delta\alpha}{\delta V}$ is a constant. Transmission through an absorbing medium follows the exponential relationship

$$T = e^{-\alpha L} , \quad (6.13)$$

where L is the distance of propagation in the medium. The transmitted power of the BRAQWET modulator is thus expected to be

$$T = e^{-\alpha_o L} e^{-\frac{\delta\alpha}{\delta V} V L} . \quad (6.14)$$

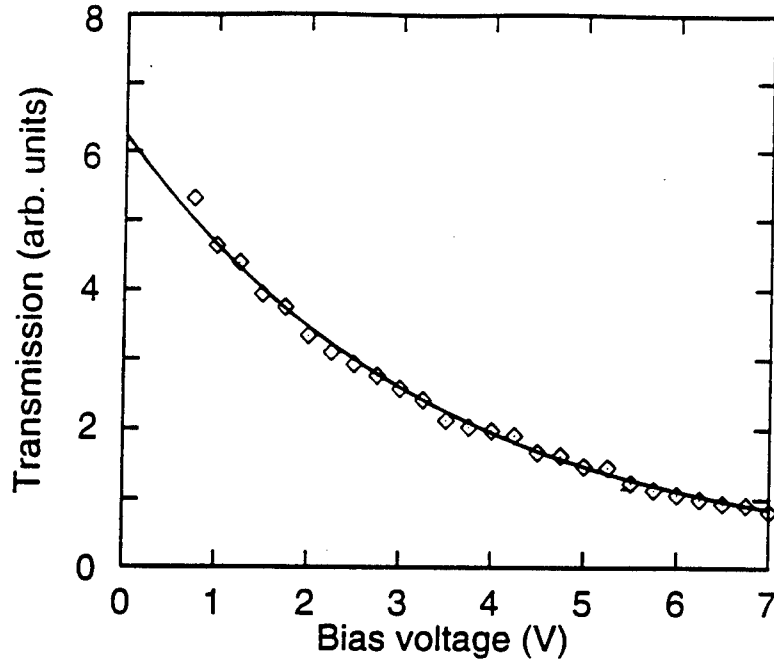


Figure 6.2: Transmission properties of a BRAQWET modulator showing the inverse exponential relationship to bias voltage. Actual measured data points are superimposed to show how well the model predicts experimental results.

This inverse exponential relationship is shown in Fig. 6.2 along with some actual data points from BRAQWET modulators described later in this chapter. It is readily apparent that this theoretical curve provides a very good fit to the measured data.

6.3 Three-Period GaAs/AlGaAs BRAQWET Modulator

The epitaxial layer structure for the first modulator structure that was investigated is shown in Table 6.1. Computer simulations of the optical mode profile of this structure were used to optimize the thicknesses of the device layers such that the final device forms a single mode optical waveguide. Fig-

Layer	Composition	Thickness	Doping (cm^{-3})
Contact	GaAs	50nm	$n = 2 \times 10^{18}$
Cladding	$\text{Al}_{0.5}\text{Ga}_{0.5}\text{As}$	$0.8\mu\text{m}$	$n = 1 \times 10^{18}$
spacer	$\text{Al}_{0.1}\text{Ga}_{0.9}\text{As}$	10nm	$n = 4 \times 10^{18}$
BRAQWET structure <i>repeat</i> <i>3 times</i>	$\text{Al}_{0.1}\text{Ga}_{0.9}\text{As}$	30nm	$n = 4 \times 10^{18}$
	$\text{Al}_{0.1}\text{Ga}_{0.9}\text{As}$	9nm	undoped
	GaAs	5nm	undoped
	$\text{Al}_{0.3}\text{Ga}_{0.7}\text{As}$	37nm	undoped
	$\text{Al}_{0.3}\text{Ga}_{0.7}\text{As}$	5nm	$p = 5 \times 10^{18}$
	$\text{Al}_{0.3}\text{Ga}_{0.7}\text{As}$	23nm	undoped
	$\text{Al}_{0.1}\text{Ga}_{0.9}\text{As}$	10nm	undoped
spacer	$\text{Al}_{0.1}\text{Ga}_{0.9}\text{As}$	10nm	$n = 4 \times 10^{18}$
Cladding	$\text{Al}_{0.5}\text{Ga}_{0.5}\text{As}$	$1.0\mu\text{m}$	$n = 1 \times 10^{18}$
Contact	GaAs	$0.2\mu\text{m}$	$n = 2 \times 10^{18}$

Table 6.1: Layer structure of 3-period GaAs/AlGaAs BRAQWET modulator

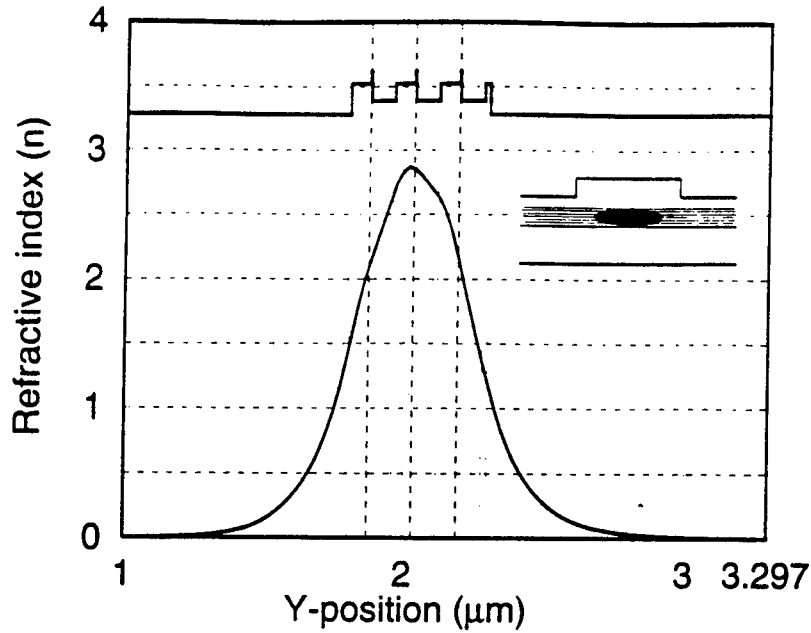


Figure 6.3: Refractive index profile in y-direction of 3-period GaAs-based BRAQWET modulator. The corresponding optical mode is also shown. The inset shows the position of the optical mode within the ridge waveguide.

Figure 6.3 shows a plot of the refractive index profile of the modulator and the single supported optical mode.

Since this structure uses $\text{Al}_{0.1}\text{Ga}_{0.9}\text{As}$ ($E_g = 1.55 \text{ eV}$) for the electron reservoir and GaAs ($E_g = 1.42 \text{ eV}$) for the quantum-well, this structure is expected to be an effective modulator for light with wavelengths in the range $0.81 \mu\text{m} < \lambda < 0.86 \mu\text{m}$. In practice, the degenerate doping of the reservoir region creates a lower bandgap region and the modulators were found to only operate properly with wavelengths between $0.83 \mu\text{m}$ and $0.86 \mu\text{m}$.

6.3.1 Device Results

Waveguide modulators were fabricated using the Laser-Modulator process described in section 2.6. The standard ridge waveguide process was used which

resulted in widths of $3\text{ }\mu\text{m}$ for the waveguide and $20\text{ }\mu\text{m}$ for the active device. The fabricated devices were cleaved to a waveguide length of $200\text{ }\mu\text{m}$. DC and RF optical modulation experiments were performed with the modulator mounted on the polished edge of a 0.5 mm thick copper strip attached to a test fixture. A microstrip launch was used to deliver the high frequency signal to the device. However, since microscope objectives were used for the input and output light coupling, a 1 mil Au bond wire was required to connect the modulator to the microstrip launcher. The length of this bond wire was nearly 10 mm . 850 nm light from a tunable AlGaAs laser diode was used for the modulation experiments.

Figures 6.4 and 6.5 show the I/V response curves of the modulator under dark and light guiding conditions respectively. While the dark modulator shows an ideal PDB response curve, a large photocurrent is observed under forward bias when light is guided in the modulator. This photocurrent arises from the photo-generated electrons in the top period of the stacked BRAQWET structure. As shown in Fig. 6.1 (d), although the electrons generated in the lower BRAQWET structures are prevented from leaving their reservoir region by the neighboring PDB structures, the electron generated in the top quantum well see no such barrier. So, while this effect is understandable, it suggests that all three of the BRAQWET structures are not experiencing identical conditions. It is important that all structures in the stack act in concert for maximum efficiency. In addition, the photocurrent out of the top structure was found to reach levels of over 1 mA with sufficient light input to the waveguide. It is unlikely that the 30 nm reservoir layers will be able to absorb this large volume of electrons. It is probable that the electron concentrations in the region will

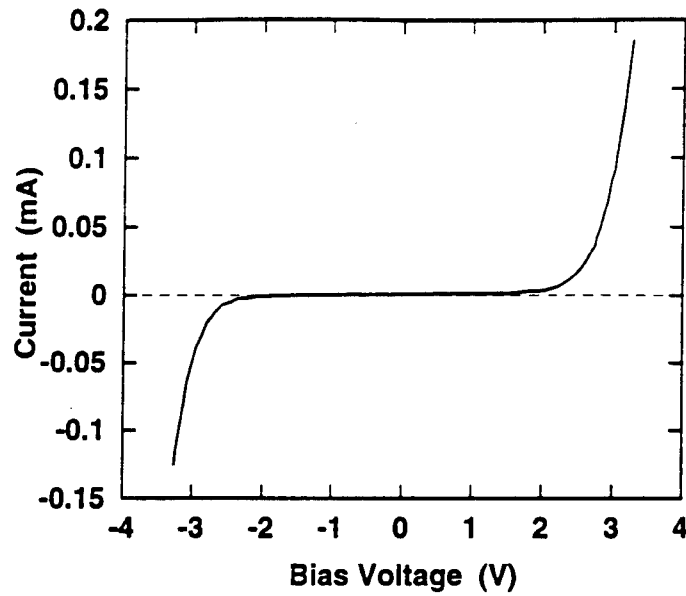


Figure 6.4: BRAQWET I/V response in dark conditions showing ideal PDB response

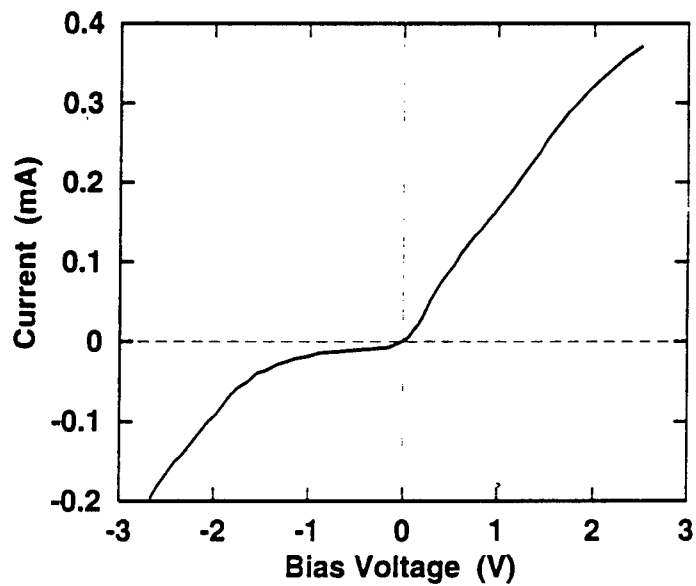


Figure 6.5: BRAQWET I/V response with light guided in waveguide showing large photocurrents under positive bias.

rise to levels that will prevent any further electron absorption in the quantum wells.

Figure 6.6 shows the transmitted optical intensity as a function of the applied DC bias. The device exhibited an inverse exponential modulation characteristic as expected from the nature of the fermi distribution set by the electron reservoir. The modulation depth was found to be as high as 90%. For 50% modulation, the required voltage swing is a mere 1 volt ($V_{3dB} = 1.0$ V). This result is comparable to the best reported QCSE modulators [85, 86]. The kink in the response curve near 0.25 V corresponds directly to the voltage required to overcome the 0.22 V conduction band offset between the $Al_{0.1}Ga_{0.9}As$ reservoir region and the $Al_{0.5}Ga_{0.5}As$ upper cladding.

High frequency optical modulation results are shown in Fig. 6.7. This result indicates a 3dB modulation bandwidth of 1.0 GHz. However, the roll-off of the response curve was much faster than would be expected for an RC limited response. One-port microwave S-parameter measurements followed by an equivalent circuit analysis revealed that the sharp drop-off in response is due to a resonance set up between the large inductance of the 10 mm bond wire and the capacitance of the modulator. The actual RC limited response as determined from the electrical measurements was 1.6 GHz.

This low RC limited response is primarily due to the large capacitance of the fabricated structure. The modulator device consists of three periods of the BRAQWET structure, each consisting of an 89 nm planar doped barrier to prevent unwanted current flow. Consequently, the electrical equivalent circuit of the device is modeled as three series capacitors, each with capacitance

$$C_0 = \frac{\epsilon_s \epsilon_0 A}{d} \quad (6.15)$$

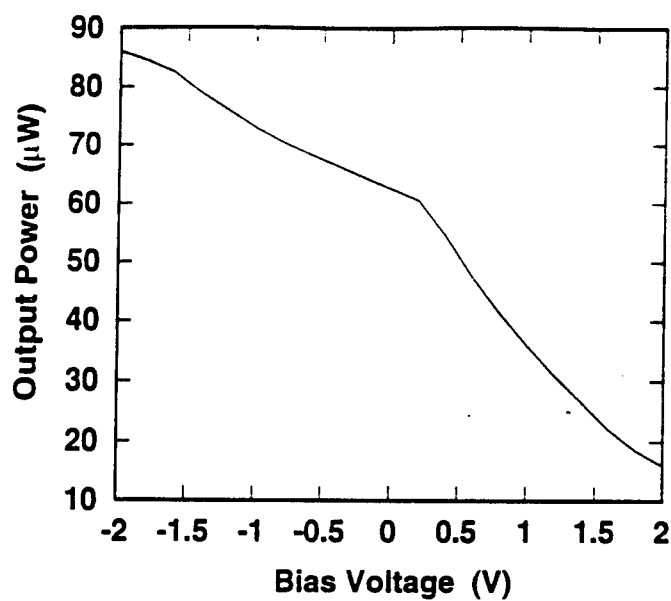


Figure 6.6: Output power as a function of DC bias for 3-period GaAs-based BRAQWET modulator

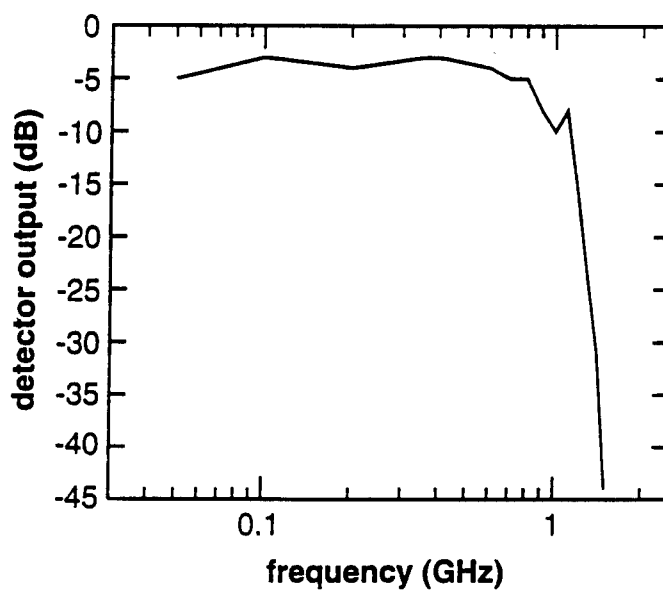


Figure 6.7: Measured optical modulation bandwidth of 3-period GaAs-based BRAQWET modulator

$$= 4.9\text{pF} . \quad (6.16)$$

where the relative dielectric constant $\epsilon_r = 12.2$ for the $\text{Al}_{0.3}\text{Ga}_{0.7}\text{As}$ barrier layers, device area $A = 20\mu\text{m} \times 200\mu\text{m}$ for the waveguides tested, and the dielectric thickness is the width of the PDB ($d = 89\text{nm}$). Since three such structures are present, the total capacitance is one third of the above value. Then, considering the 50 source resistance, the 3dB RC limited bandwidth can be estimated to be

$$f_{3\text{dB}} = \frac{1}{2\pi R \frac{C_0}{3}} \quad (6.17)$$

$$= 1.9 \text{ GHz} . \quad (6.18)$$

This is in good agreement with the measured electrical bandwidth.

6.3.2 Increasing RC Limited Frequency Response

The capacitance of the devices was found to be the critical factor limiting high-speed performance. The devices are fabricated as ridge waveguides with a $3\mu\text{m}$ ridge but with a full $20\mu\text{m}$ device width. Although the entire $20\mu\text{m}$ width of the modulator contributes to the device capacitance, only the small portion of the device directly under the ridge is actually necessary for modulating the light as this is where the guided optical mode is located. The remainder of the device area is unnecessary and should be considered a parasitic capacitance.

To reduce the capacitance, the device area must be reduced. One option is to shorten the length of the waveguide. Cleaving waveguide modulators to lengths shorter than $150\mu\text{m}$ is difficult as the substrate thickness must be less than half the cleave length. Ido *et al.* [87] recently reported on a process by which a short modulator (lengths down to $50\mu\text{m}$) is integrated with passive

waveguides such that the actual fabricated device can have long (1 mm) lengths for easy cleaving, but low RC-limited bandwidths. Their process requires complex etching steps and epitaxial regrowth of the passive waveguide. So, while this technique is promising, it was not easily incorporated into my fabrication process.

6.3.3 Self-Aligned Double-Ridge Process for Low Capacitance Single-Mode Waveguides

The width of the device must be reduced to lower the capacitance of the modulator structure. One option is to continue the 3 μm ridge etch all the way through the device active regions. However, if the ridge etch was continued completely through the waveguiding layers, an undesirable multi-mode waveguide would result. The only way to restore the single-mode nature of the waveguide after the deep etch would be to re-grow an insulating semiconductor cladding layer over the side-walls of the etched waveguide. This regrowth adds great complexity to the device processing and was not pursued for this work.

To create the low capacitance single mode waveguide, the original ridge structure was retained, but the active device area was reduced by means of a second ridge etch. An examination of the transverse mode profile of the guided wave was necessary to determine how far the second ridge should extend to retain the single mode nature of the waveguide. From Fig. 6.8 we see that at distances just 1 μm from the edge of the 3 μm etched ridge, the optical mode intensity has already dropped by almost four orders of magnitude. Therefore, a 5 μm second ridge would be sufficient. However, creating an etch mask

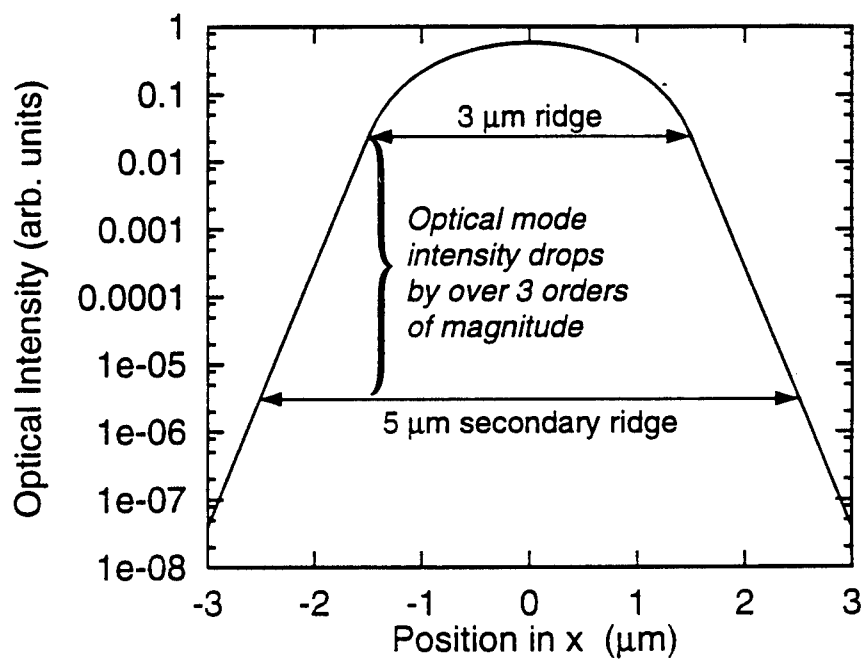


Figure 6.8: Transverse optical mode profile in 3 μm ridge waveguide. At just 1 μm from the edge of the ridge the intensity of the optical mode is already over three order of magnitude below the intensity at the edge of ridge.

that extends only 1 μm from the sides of the original ridge poses a special problem due to difficulties in performing the optical lithography with such a small tolerance for misalignment.

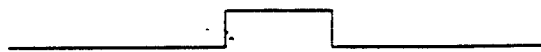
A self-aligned double-ridge waveguide process was developed which retains the single mode nature of the original structure but reduces the device area and capacitance by 75%. Instead of relying on a optical alignment to create the etch mask, a novel PECVD SiO_2 sidewall process is used to create a self-aligned etch mask. Figure 6.9 shows the processing steps required to fabricate this second ridge. Note that the device etch is completely self-aligned to the ridge. A scanning electron micrograph showing the cleaved waveguide facet of a BRAQWET modulator fabricated with the self-aligned double-ridge process is shown in Fig. 6.10

6.4 Modulator with Top PDB Barrier

From the strong forward-bias-only photocurrent displayed in Fig. 6.5, it is evident that the top BRAQWET structure is operating under different conditions from the other two. In fact, due to the large volume of photogenerated electrons and their inability to escape from the reservoir region, there is the possibility that electron concentrations in the confined region will rise to levels that will prevent any further electron absorption in the quantum wells

To study this, a modulator structure was designed in which electrons photogenerated by the top BRAQWET structure are prevented from escaping the reservoir region by the incorporation of an additional PDB structure in the upper cladding region. The layer structure for this device is shown in Table 6.2.

1) Perform standard ridge etch



2) Deposit conformal PECVD oxide with 1 μm thickness



3) Use directional RIE etch to remove oxide while leaving sidewalls intact



4) Use RIE etch process to etch through waveguiding layer

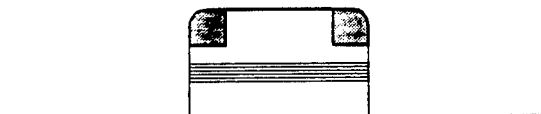


Figure 6.9: Self-aligned double-ridge process for reducing device area of BRAQWET modulators

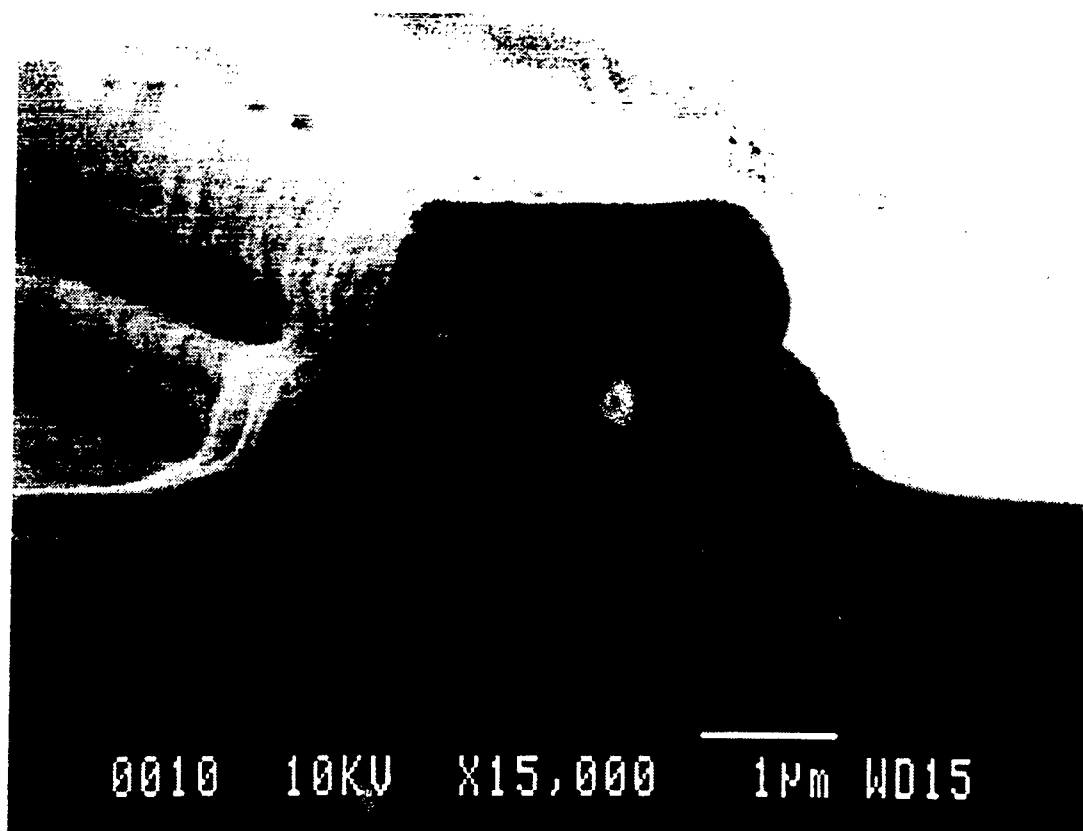


Figure 6.10: Scanning electron micrograph of waveguide facet of BRAQWET modulator showing double-ridge fabrication profile

Layer	Composition	Thickness	Doping (cm^{-3})
Contact	GaAs	50nm	$n = 5 \times 10^{18}$
Cladding	$\text{Al}_{0.3}\text{Ga}_{0.7}\text{As}$	$0.9\mu\text{m}$	$n = 2 \times 10^{17}$
planar doped barrier	$\text{Al}_{0.1}\text{Ga}_{0.9}\text{As}$	10nm	$n = 5 \times 10^{18}$
	$\text{Al}_{0.1}\text{Ga}_{0.9}\text{As}$	15nm	undoped
	$\text{Al}_{0.3}\text{Ga}_{0.7}\text{As}$	35nm	undoped
	$\text{Al}_{0.3}\text{Ga}_{0.7}\text{As}$	5nm	$p = 3 \times 10^{18}$
	$\text{Al}_{0.3}\text{Ga}_{0.7}\text{As}$	50nm	undoped
	$\text{Al}_{0.1}\text{Ga}_{0.9}\text{As}$	5nm	undoped
BRAQWET structure <i>repeat 4 times</i>	$\text{Al}_{0.1}\text{Ga}_{0.9}\text{As}$	20nm	$n = 5 \times 10^{18}$
	$\text{Al}_{0.1}\text{Ga}_{0.9}\text{As}$	10nm	undoped
	GaAs	5nm	undoped
	$\text{Al}_{0.3}\text{Ga}_{0.7}\text{As}$	35nm	undoped
	$\text{Al}_{0.3}\text{Ga}_{0.7}\text{As}$	5nm	$p = 3 \times 10^{18}$
	$\text{Al}_{0.3}\text{Ga}_{0.7}\text{As}$	50nm	undoped
	$\text{Al}_{0.1}\text{Ga}_{0.9}\text{As}$	5nm	undoped
spacer	$\text{Al}_{0.1}\text{Ga}_{0.9}\text{As}$	10nm	$n = 5 \times 10^{18}$
Cladding	$\text{Al}_{0.3}\text{Ga}_{0.7}\text{As}$	$1.4\mu\text{m}$	$n = 2 \times 10^{17}$
Contact	GaAs	$0.5\mu\text{m}$	$n = 5 \times 10^{18}$
Semi-Insulating GaAs Substrate			

Table 6.2: Layer structure for GaAs-based modulator with top PDB barrier. The extra barrier prevents the photo-generated electrons in the top BRAQWET period from flowing out of the device.

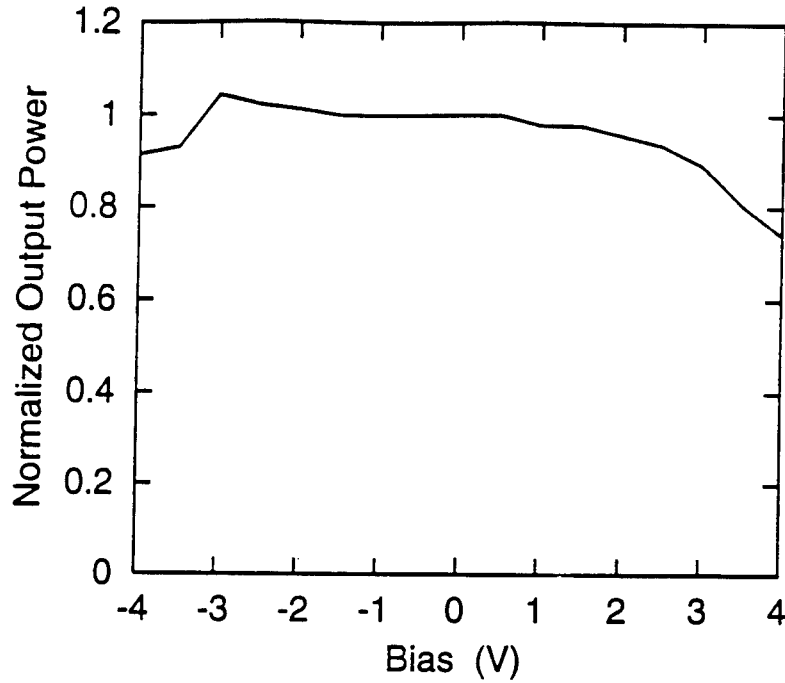


Figure 6.11: Output power as a function of DC bias for 3-period GaAs-based BRAQWET modulator with top PDB barrier

Device Results

This device exhibited a similar I/V profile in dark conditions as that shown in Fig. 6.4. The response curves indicated that current begins to flow over the PDB barriers at bias levels of ± 3 V. However, the I/V curves when light was guided by the waveguide did not show the photocurrent under forward bias as was observed before. This indicated that the additional PDB structure was performing its desired function.

The measured DC optical modulation response is shown in Fig. 6.11. The observed response shows that there is practically no optical modulation in the region of normal device operation. For bias levels outside the range of ± 3 V, slight optical modulation is observed — but the output power decreases for *both* positive and negative biases. This supports the theory that absorption

will be totally quenched by the build-up of electrons in the confined reservoir regions. For the bias levels where electrons start to flow over the planar doped barriers and out of the device, there is a reduction in electron concentration within the device and the quantum wells are able to absorb photons again.

This result confirms that, when used as an amplitude modulator, there is no benefit for stacking multiple BRAQWET structures. Only the top device contributes to modulation because it is the only one with a current path for the removal of the photo-generated electrons.

6.5 Modulator with only One Period of BRAQWET Structure

Having established that only the top BRAQWET structure contributes to optical modulation, one final modulator was designed. To realize the high modulation frequencies promised by this modulator technology, the device capacitance must be reduced as much as possible. In previous designs, one constraint on the capacitance was that the multiply stacked planar doped barriers needed to be thin enough that several of them could fit entirely within the waveguide region. However, since only one PDB needs to be present, there is no reason it must be contained entirely within the waveguide region. The layer structure of the one-period BRAQWET modulator design is shown in Table 6.3 and the corresponding waveguide mode profile is shown in Fig. 6.12. This design incorporates the PDB layer into the lower waveguide cladding layer. A total PDB thickness of $0.5\text{ }\mu\text{m}$ was possible using this design. The estimated capacitance of a fabricated $5\text{ }\mu\text{m} \times 200\text{ }\mu\text{m}$ device made with this structures is only 0.22 pF. With this sub-picofarad capacitance, the RC limited device

Layer	Composition	Thickness	Doping (cm^{-3})
Contact	GaAs	50nm	$n = 5 \times 10^{18}$
Cladding	$\text{Al}_{0.4}\text{Ga}_{0.6}\text{As}$	$1.0\mu\text{m}$	$n = 2 \times 10^{17}$
reservoir	$\text{Al}_{0.1}\text{Ga}_{0.9}\text{As}$	180nm	$n = 5 \times 10^{18}$
spacer	$\text{Al}_{0.1}\text{Ga}_{0.9}\text{As}$	20nm	undoped
QW	GaAs	6nm	undoped
PDB	$\text{Al}_{0.3}\text{Ga}_{0.7}\text{As}$	300nm	undoped
	$\text{Al}_{0.3}\text{Ga}_{0.7}\text{As}$	50nm	$p = 1 \times 10^{19}$
	$\text{Al}_{0.3}\text{Ga}_{0.7}\text{As}$	125nm	undoped
spacer	$\text{Al}_{0.3}\text{Ga}_{0.7}\text{As}$	150nm	$n = 5 \times 10^{18}$
Cladding	$\text{Al}_{0.3}\text{Ga}_{0.7}\text{As}$	850nm	$n = 2 \times 10^{17}$
Contact	GaAs	500nm	$n = 5 \times 10^{18}$
S.I. GaAs Substrate			

Table 6.3: Layer structure for GaAs-based modulator with only one period of BRAQWET structure. By merging the PDB structure with the lower cladding, the device capacitance is reduced while still keeping the waveguide region below the critical thickness for assuring single mode operation.

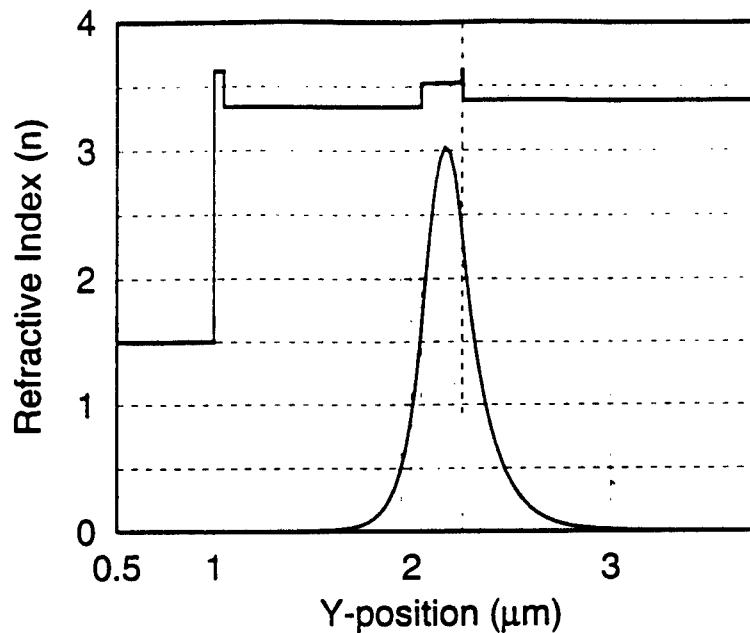


Figure 6.12: Refractive index profile in y-direction of single-period GaAs-based BRAQWET modulator. The corresponding optical mode is also shown.

response is estimated to be $f_{3dB} = 15$ GHz.

Another feature of this device is that the PDB diode was made strongly asymmetric so that device would have a larger turn-on voltage in the forward biased direction than in the reverse. The previous result (see Fig. 6.6) showed a greater modulation depth while operating in forward biased mode where electrons are able to escape the device. With this in mind, the modulator was designed primarily for operation under forward bias.

Device Results

This device exhibited the same characteristic I/V profile in dark conditions as both of the other modulators. However, the turn on voltages where current would start to flow were much higher due to the larger size of the PDB diode. This is expected due to the increased length and height of the planar doped

barrier. The forward bias turn on voltage was measured to be 10 V.

The measured DC optical modulation response is shown in Fig. 6.13 and the corresponding device photocurrent is shown in Fig. 6.14. This modulator is shown to have an 80% total modulation depth with a 50% modulation possible with a voltage swing of just 2 V. The increased voltage for 50% modulation is the trade off made when using the extra thick PDB structure. However, it is evident that this modulator is comparable in modulation depth and drive voltage to the original modulator which had the stack of three BRAQWET structures. This further verifies that only one BRAQWET structure is contributing to optical modulation.

One-port microwave S-parameter measurements were used to evaluate the RC limited frequency response of these modulators. The measured data were used to determine the equivalent circuit of the device. The modulator was found to fit to a simple circuit with three elements: C_{dev} is the capacitance of the modulator, R_{ser} accounts for the series resistances in the structure, and C_{pad} represents the capacitances caused by the interconnect metal and contact pads. A diagram of the equivalent circuit and the corresponding *Libra* circuit file can be found in App. B.

The best fit to the measured data was found to be: $C_{dev} = 260$ fF, $R_{ser} = 79.2$ and $C_{pad} = 168$ fF. Another *Libra* simulation was then performed to determine the RC-limited frequency response of this structure. Figure 6.15 shows a plot of S_{21} which indicates that the modeled RC-limited bandwidth of the modulator is $f_{3dB} = 17$ GHz. Please note that while the extracted device capacitance is in good agreement with the predicted value, this result is higher than predicted RC limited response. This is due to the non-zero pad capacitance C_{pad} which

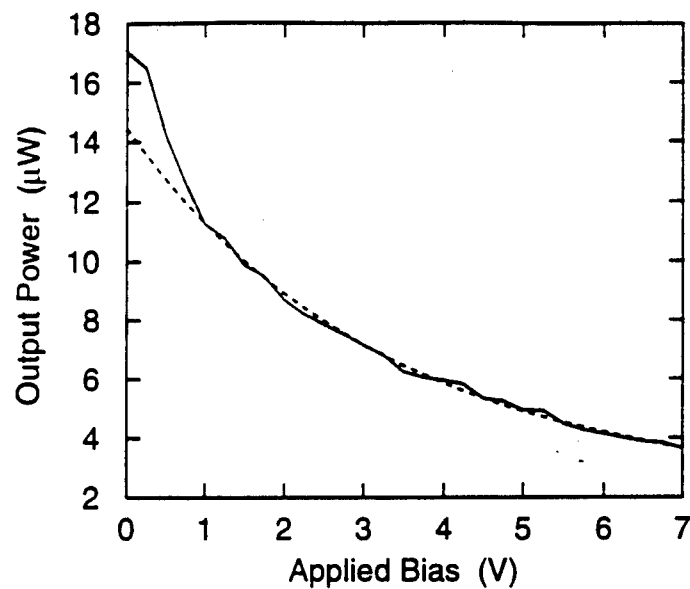


Figure 6.13: Output power as a function of DC bias for single-period GaAs-based BRAQWET modulator. The dashed line shows a fit to the theoretical modulator response with a linear bias to absorption coefficient behavior.

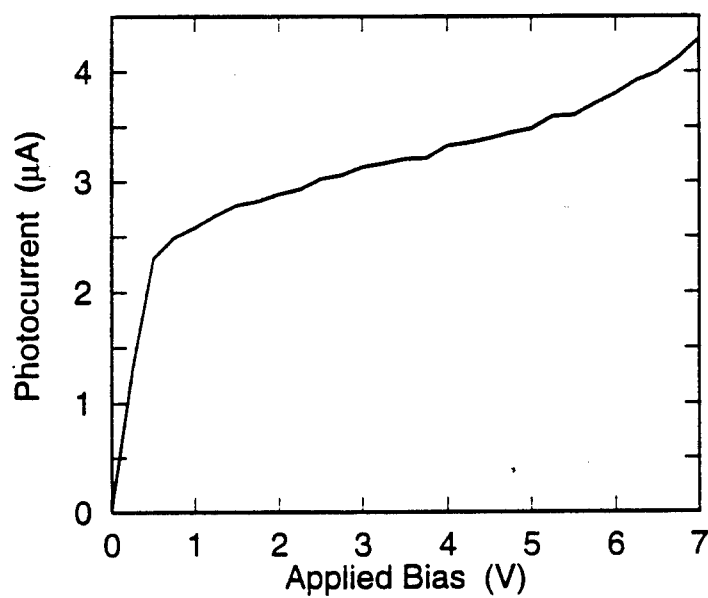


Figure 6.14: I/V response of single-period GaAs-based BRAQWET modulator

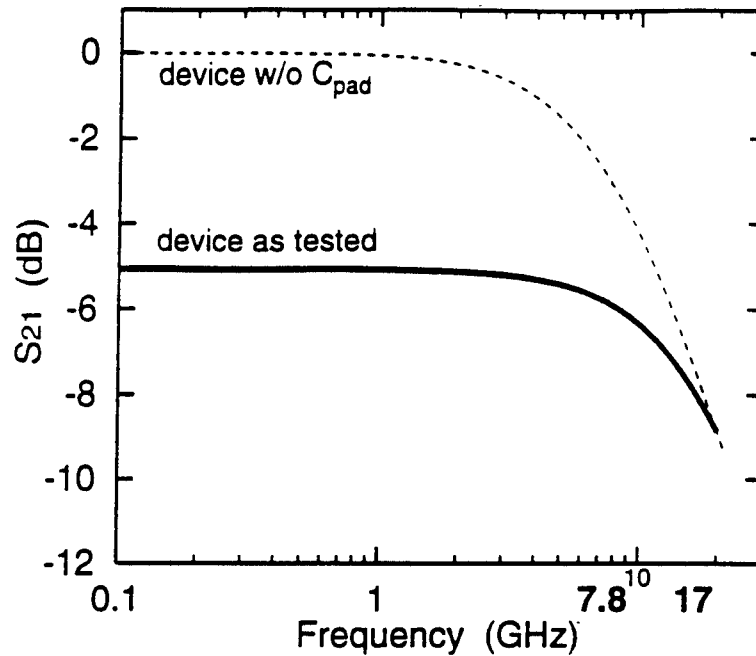


Figure 6.15: S_{21} simulation of modulator equivalent circuit indicates a RC limited bandwidth of 17 GHz.

lowered the low frequency values of S_{21} from 0 dB to -5.4 dB and therefore pushed out the 3dB roll-off point. While the increased bandwidth is appealing, it comes at the cost of requiring a larger drive power to achieve the same modulation depth. If the interconnect pads were removed, lower drive power would be necessary but the device would exhibit a bandwidth of only 8 GHz which is lower than the predicted value due to a relatively high R_{ser} . Further work on these devices will require effort to reducing the series resistance in the device.

6.6 Summary

Devices based on the blockaded reservoir and quantum well electron transfer structure were investigated for creating the modulated optical signals required for the optical injection locking experiments. Experimental work has

shown that only the top BRAQWET structure contributes to optical amplitude modulation. A self-aligned double-ridge waveguide processes was developed to reduce the device capacitance and consequently, to increase the RC limited frequency response. A GaAs-based BRAQWET modulator incorporating only one quantum well and fabricated using the double-ridge structure demonstrated an 80% modulation depth and was determined to have an RC limited 3dB bandwidth of $f_{3dB} = 17$ GHz.

APPENDIX A

EXTRACTION AND CONVERSION OF OPTICAL IMPULSE RESPONSE

A.1 Extraction of Impulse Response from Measurements

Optical impulse response measurements generally result in a measured response profile which is wider than the true impulse response of the device under test. The device's impulse response is convolved with the time profile of the optical pulse and with the transfer function of the oscilloscope sampling head used for the measurement. The measured response $v(t)$ to an optical pulse $P_{opt}(t)$ can be expressed as

$$v(t) = [\eta P_{opt}(t) * f_{dev}(t)] * f_{scope}(t), \quad (A.1)$$

where $f_{dev}(t)$ and $f_{scope}(t)$ represent the impulse transfer functions of the device and oscilloscope respectively. η represents a scaling constant which represents the conversion of optical power into photo-generated current.

While Eqn. A.1 cannot be easily used to rigorously solve for $f_{dev}(t)$, a good estimate for the full width at half maximum (*FWHM*) of the devices impulse response is possible. If all the response function are approximated as having

Gaussian profiles with *FWHM* values that match the actual responses, the *FWHM* of the device under test can be extracted.

When two Gaussian functions, $f(t)$ and $g(t)$ are convolved, the result is a third Gaussian function $h(t)$. The convolution proceeds as follows.

$$f(t) = \exp(-at^2), \quad (\text{A.2})$$

$$g(t) = \exp(-bt^2), \quad (\text{A.3})$$

$$h(t) = f(t) * g(t). \quad (\text{A.4})$$

In Fourier transform space, these equations become: $F(\omega) = \mathcal{F}\{f(t)\}$

$$F(\omega) = \frac{1}{\sqrt{2a}} \exp\left(-\frac{\omega^2}{4a}\right), \quad (\text{A.5})$$

$$H(\omega) = F(\omega)G(\omega) \quad (\text{A.6})$$

$$= \frac{1}{\sqrt{2a}} \exp(-\omega^2/4a) \frac{1}{\sqrt{2b}} \exp(-\omega^2/4b) \quad (\text{A.7})$$

$$= \frac{1}{\sqrt{4ab}} \exp\left(-\omega^2 \frac{a+b}{4ab}\right), \quad (\text{A.8})$$

$$h(t) = \frac{1}{\sqrt{2(a+b)}} \exp\left(-\frac{ab}{a+b} t^2\right). \quad (\text{A.9})$$

Equation A.9 is just the Gaussian function $h(t) \propto \exp(-ct^2)$ with

$$c = \frac{ab}{a+b}. \quad (\text{A.10})$$

Now we must determine how the *FWHM*'s of the Gaussian functions are changed by the convolution. First, the relationship between the exponential multipliers a , b and c and the *FWHM* of the Gaussian is determined by considering that $f(t)$ is at half maximum when $t = \frac{1}{2}FWHM$.

$$f(t) = \exp(-at^2), \quad (\text{A.11})$$

$$1/2 = \exp\left[-a \left(\frac{FWHM}{2}\right)^2\right], \quad (\text{A.12})$$

$$a = \frac{4 \ln 2}{(FWHM)^2}. \quad (\text{A.13})$$

From Eqn. A.13 we see that a is proportional to $(FWHM)^{-2}$. Now, defining τ_f , τ_g and τ_h as the $FWHM$ values for $f(t)$, $g(t)$ and $h(t)$, we can use Eqn. A.10 to solve for τ_h .

$$\tau_h^{-2} = \frac{\tau_f^{-2} \tau_g^{-2}}{\tau_f^{-2} + \tau_g^{-2}} . \quad (\text{A.14})$$

$$\tau_h^2 = \tau_f^2 \tau_g^2 \left(\frac{1}{\tau_f^2} + \frac{1}{\tau_g^2} \right) . \quad (\text{A.15})$$

which reduces to

$$\tau_h^2 = \tau_f^2 + \tau_g^2 . \quad (\text{A.16})$$

Equation A.16 is easily extended to include further Gaussian convolutions. We can now extract the device response from the convolution expression in Eqn. A.1.

$$v(t) = [\eta P_{opt}(t) * f_{dev}(t)] * f_{scope}(t) , \quad (\text{A.17})$$

$$\tau_{meas}^2 = \tau_{pulse}^2 + \tau_{device}^2 + \tau_{head}^2 , \quad (\text{A.18})$$

$$\tau_{device} = \sqrt{\tau_{meas}^2 - \tau_{pulse}^2 - \tau_{head}^2} , \quad (\text{A.19})$$

where τ_{meas} is the $FWHM$ of the measured impulse response, τ_{pulse} is the $FWHM$ of the optical pulse, τ_{head} is the $FWHM$ of the oscilloscope sampling head response and τ_{device} is the $FWHM$ of the actual device response.

A.2 Conversion of Impulse Response to Bandwidth

The 3dB cutoff frequency of the device as a photo-detector can be extracted from the impulse response by performing a Fourier transform. The Fourier transform of the time-domain impulse response gives the frequency domain

spectrum. If the same assumption is made that the impulse response has a Gaussian profile in time, the frequency bandwidth can be extracted directly. The impulse response is approximated modeled as the Gaussian function $v(t) = \exp(-at^2)$ with the same *FWHM* as extracted impulse response. a is determined from the *FWHM* using Eqn. A.13.

$$a = \frac{4 \ln 2}{(FWHM)^2} \quad (A.20)$$

The Fourier transform of the Gaussian pulse $V(f) = \mathcal{F}\{v(t)\}$ is found to be

$$V(f) = \mathcal{F}\{\exp(-at^2)\} \quad (A.21)$$

$$V(f) = \frac{1}{\sqrt{2a}} \exp[-(2\pi f)^2/4a] \quad (A.22)$$

$$V(f) = \frac{FWHM}{\sqrt{8 \ln 2}} \exp\left[-\frac{\pi^2(FWHM)^2}{4 \ln 2} f^2\right] \quad (A.23)$$

The 3dB bandwidth of the device is then determined from Eqn. A.23 as the frequency where $V(f)$ drops to half of its maximum value.

$$1/2 = \exp\left[-\frac{\pi^2(FWHM)^2}{4 \ln 2} f_{3dB}^2\right] \quad (A.24)$$

$$f_{3dB} = \frac{2 \ln 2}{\pi} (FWHM)^{-1} \quad (A.25)$$

It is important to note that, although Eqn. A.25 properly determines the 3dB bandwidth from a Gaussian profile in time, actual impulse response measurements are seldom truly Gaussian. Equation A.25 can still be used to *approximate* the frequency bandwidth, but a more accurate Fourier transform method should be used for a more correct result.

APPENDIX B

LIBRA CIRCUIT FILES

B.1 MMIC Oscillator

This is an example Libra circuit file for the design of a 15 GHz MMIC oscillator. Libra was used to tune the sizes of the spiral inductors and parallel plate capacitors for proper circuit operation.

```
! 15 GHz MMIC Oscillator
```

```
DIM
```

```
  FREQ GHZ  
  RES OH  
  IND PH  
  CAP FF  
  LNG UM  
  TIME PS  
  COND /KOH  
  ANG DEG
```

```
VAR
```

```
  Lb = 593.5540  
  Ce = 113.1246    ! size=78x78  
  Lc = 597.5202
```

```
  XLb = 77  
  XLc = 72
```

```
CKT
```

```

MSUB ER=12.61 H=150 T=2 RHO=1 RGH=0

S2P 1 2 4 c1_5a09
! IND 1 5 L^Lb
MRIND 1 5 N=2.5 L1^XLb L2^XLb W=3 S=5 W1=10 W2=10
CAP 4 0 C^Ce
! IND 2 3 L^Lc
MRIND 2 3 N=2.5 L1^XLc L2^XLc W=3 S=5 W1=10 W2=10

! BIAS TEE ELEMENTS
! MRIND 5 0 N=4.5 L1=120 L2=120 W=3 S=5 W1=10 S2=10
MRIND 2 0 N=4.5 L1=120 L2=120 W=3 S=5 W1=1 S2=10
MRIND 4 7 N=5.5 L1=120 L2=120 W=3 S=5 W1= S2=10
TFC 7 0 W=200 L=200 T=1 ER=2.1 RHO=1 TAND. C0=10 D0=10
TFC 5 0 W=300 L=300 T=1.0 ER=2.1 RHO=1 TAN. C0=10 D0=10
RES 5 0 R=50

DEF1P 3 OSC

FREQ
SWEEP 10.0 20.0 0.5

OUT
OSC z11 SCN

OPT
freq 15 15
OSC re[z1] = -100
OSC im[z1] = 0

! END OF LIBRA CIRCUIT FILE

```

B.2 HBT Equivalent Circuit

This is a Libra circuit file for the equivalent circuit modeling of a heterojunction bipolar transistor (HBT). The circuit described by this file follows the circuit model pictured in Fig. 4.13.

```
! light3.ckt  (error in fit = 0.00039)
```

```
DIM
```

```
  FREQ GHZ
  RES OH
  IND PH
  CAP FF
  LNG UM
  TIME PS
  COND /KOH
  ANG DEG
```

```
VAR
```

```
  Rb   = 10.94921
  Re   = 12.38323
  Rc   = 11.20737
  Cb   = 2414.884
  Rbi  = 32.17167
  Cfb  = 122.6018
  Rfb  = 5771.093
  Rjc  = 76129.82
  Cjc  \ 89.89600
  Rje  \ 7.182258
  Cje  = 37.42512
  Cbe  \ 871.3925
  Lb   = 52.95326
  Cpad = 22.66306
  ALPHA \ 0.979106
```

```
CKT
```

```
  S2P 1 2 0 light3
  DEF2P 1 2 B
```

```
! base:1, collector:2, emitter:10. T-model
  IND_b    1 3 L^Lb
  PRC_b    3 4 R^Rb C^Cb
  PRC_fb   4 6 R^Rfb C^Cfb
```

```

RES_bi    4 5 R^Rbi
PRC_jc    5 6 R^Rjc C^Cjc
CCCS      7 6 8 5 M^ALPHA A=0 R1=0 R2=0 F=0 T=0
RES_c     6 2 R^Rc
RES_je    5 7 R^Rje
CAP_je    5 7 C^Cje
CAP_be    5 8 C^Cbe
RES_e     8 10 R^Re
CAP_pad   1 10 C^Cpad
CAP_pad   2 10 C^Cpad
DEF3P     1 2 10 HBT

```

```

HBT 1 2 0
DEF2P 1 2 A

```

```

FREQ
SWEEP 1.0 20.0 0.5

```

```

OUT
A S11 sc2
B S11 sc2
A S22 sc2
B S22 sc2
A S12 sc1
B S12 sc1
A S21 sc1
B S21 sc1

```

```

OPT
A MODEL B

```

```

: END OF LIBRA CIRCUIT FILE

```

B.3 Waveguide Modulator

This is a Libra circuit file for the extraction of the RC limited frequency response of a waveguide modulator. The modulator is modeled as three elements as shown in Fig. B.1. Cpad is a shunted parasitic capacitor which accounts for the capacitance of the bonding pads. Rser is a series resistance to account for ohmic contact and bulk resistances. Cdev is the series capacitor representing the intrinsic modulator device.

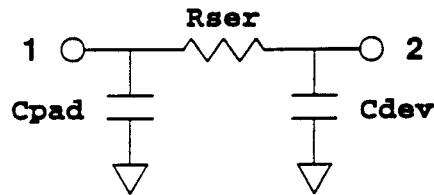


Figure B.1: Equivalent circuit of RC limited BRAQWET modulator

After fitting the three elements so that S_{11} from the simulated circuit (model) matched the measured data (data), a second circuit (xfer) was used to determine the modulator's bandwidth.

```
! braqwet.ckt
```

```
DIM
```

```
FREQ GHZ
```

```
RES OH
```

```
IND PH
```

```
CAP FF
```

```
LNG UM
```

```
TIME PS
```

```
COND /KOH
```

```
ANG DEG
```

```
VAR
```

```
Cdev \ 215.2244
```

```
Cpad \ 164.8586
```

```
Rser \ 86.80676
```


CKT

s2p 1 0 0 one2.s2p
def1p 1 data

cap 1 0 c^Cpad
res 1 2 r^Rser
cap 2 0 c^Cdev
def1p 1 model

cap 1 0 c^Cpad
res 1 2 r^Rser
cap 2 0 c^Cdev
def2p 1 2 xfer

FREQ

SWEEP 0.1 20.0 0.2

GRID

lrange .1 20
gr1 -11 -2 3

OUT

xfer db[s21] gr1
data s11 sc2
model s11 sc2

OPT

model model data

! END OF LIBRA CIRCUIT FILE

BIBLIOGRAPHY

BIBLIOGRAPHY

- [1] H. Sobol, "The application of microwave techniques in lightwave systems," *J. Lightwave Tech.*, vol. LT-5, pp. 293-299, Mar. 1987.
- [2] R. Simons, *Optical Control of Microwave Devices*. Boston: Artech House, 3 ed., 1990.
- [3] A. J. Seeds and A. A. deSalles, "Optical control of microwave semiconductor devices," *IEEE Trans. MTT*, vol. 38, pp. 577-584, 1990.
- [4] R. Adler, "A study of locking phenomena in oscillators," *Proc. IEEE*, vol. 61, pp. 1380-1385, Oct. 1973.
- [5] A. A. A. DeSalles and J. R. Forrest, "Initial observations of optical injection locking of GaAs metal semiconductor field effect transistor oscillators," *Appl. Phys. Lett.*, vol. 38, pp. 392-394, Mar. 1981.
- [6] I. D. Blanchflower and A. J. Seeds, "Optical control of frequency and phase of GaAs MESFET oscillator," *Electron. Lett.*, vol. 25, pp. 359-360, 1989.
- [7] R. D. Esman, L. Goldberg, and J. F. Weller, "Optical phase control of optically injected-locked FET microwave oscillator," *IEEE Trans. MTT*, vol. 37, pp. 1512-1518, Oct. 1989.
- [8] R. Lai, P. K. Bhattacharya, and T. Brock, "Optical tuning of monolithic $\text{In}_{0.53}\text{Ga}_{0.47}\text{As}/\text{In}_{0.52}\text{Al}_{0.48}\text{As}/\text{InP}$ modulation-doped field-effect transistor oscillators at X and R band," *Electron. Lett.*, vol. 27, pp. 1056-1058, 6 Jun. 1991.
- [9] D. Yang, P. K. Bhattacharya, and T. Brock, "Direct optical injection locking of monolithically integrated $\text{In}_{0.53}\text{Ga}_{0.47}\text{As}/\text{In}_{0.52}\text{Al}_{0.48}\text{As}$ MODFET oscillators," *Electron. Lett.*, vol. 29, pp. 944-945, May 1993.
- [10] D. Yang, P. K. Bhattacharya, R. Lai, T. Brock, and A. Paoella, "Optical control and injection locking of monolithically integrated $\text{In}_{0.53}\text{Ga}_{0.47}\text{As}/\text{In}_{0.52}\text{Al}_{0.48}\text{As}$ MODFET oscillators," *IEEE Trans. Elec. Dev.*, vol. 42, pp. 31-37, Jan. 1995.

- [11] P. M. Asbeck, M. F. Chang, K. C. Wang, D. L. Miller, G. J. Sullivan, N. Sheng, E. Sovero, and J. A. Higgins, "Heterojunction bipolar transistors for microwave and millimeter-wave integrated circuits," *IEEE Trans. Elec. Dev.*, pp. 2571–2579, 1987.
- [12] Y. Lam, *Static and Dynamic Properties of Pseudomorphic Quantum Well Lasers*. PhD thesis, The University of Michigan, Ann Arbor, 1993.
- [13] I. Suemune, L. A. Coldren, M. Yamanishi, and Y. Kan, *Appl. Phys. Lett.*, vol. 53, p. 1378, 1988.
- [14] K. Wakita, I. Kotaka, O. Mitomi, Y. Kawamura, and H. Asai, *IEEE Photon. Technol. Lett.*, vol. 3, p. 138, 1991.
- [15] R. E. Williams, *Gallium Arsenide Processing Techniques*. Massachusetts: Artech House, 1984.
- [16] J. C. Cowles, *InP-Based Heterojunction Bipolar Trnasistor Technology for High Speed Devices and Circuits*. PhD thesis, The University of Michigan, Ann Arbor, 1994.
- [17] A. Stano, "Chemical etching characteristics of InGaAs/InP and InAlAs/InP heterostructures," *J. Electrochem. Soc.*, vol. 134, pp. 448–452, Feb. 1987.
- [18] S. Adachi and K. Oe, "Chemical etching characteristics of (001) GaAs," *J. Electrochem. Soc.*, vol. 130, pp. 2427–2435, Dec. 1983.
- [19] S. Adachi, Y. Noguchi, and H. Kawaguchi, "Chemical etching of InGaAsP/InP DH wafer," *J. Electrochem. Soc.*, vol. 129, pp. 1053–1062, May 1982.
- [20] T. Matsuoka and H. Hagai, "InP etchant for submicron patterns," *J. Electrochem. Soc.*, vol. 133, no. 12, pp. 2485–2491, 1986.
- [21] K. Kenefickh, "Selective etching characteristics of peroxide/ammonium-hydroxide solutions for GaAs/Al_{0.16}Ga_{0.84}As," *Semicon. Sci. Tech.*, vol. 129, no. 10, 1982.
- [22] Y. Uenishi, H. Tanaka, and H. Ukita, "Characterization of AlGaAs microstructure fabricated by AlGaAs/GaAs micromachining," *IEEE Trans. Elec. Dev.*, vol. 41, no. 10, pp. 1778–1783, 1994.
- [23] N. J. Sauer and K. B. Chough, "A selective etch for InAlAs over InGaAs and for different InGaAlAs quaternaries," *J. Electrochem. Soc.*, vol. 139, no. 1, pp. L10–L11, 1992.
- [24] L. He and W. A. Anderson, "Effects of oxygen implantation in GaAs," *Solid State Elect.*, vol. 36, no. 2, pp. 173–178, 1993.

- [25] M. F. Chang, P. M. Asbeck, K. C. Wang, G. J. Sullivan, N. Sheng, J. A. Higgins, and D. L. Miller, "AlGaAs/GaAs heterojunction bipolar transistors fabricated using a self-aligned dual-lift-off process," *IEEE Elec. Dev. Lett.*, vol. EDL-8, pp. 303–305, July 1987.
- [26] S. Yamahata, Y. Matsuoka, and T. Ishibashi, "High- f_{max} collector-up AlGaAs/GaAs heterojunction bipolar transistors with a heavily carbon-doped base fabricated using oxygen-ion implantation," *IEEE Elec. Dev. Lett.*, vol. 14, pp. 173–175, Apr. 1993.
- [27] D. V. Morgan and F. H. Eisen, *Gallium Arsenide Materials, Devices and Circuits*, ch. 5. New York: Wiley, 1985.
- [28] B. Tell, T. Y. Chang, K. F. Brown-Goebeler, J. M. Kuo, and N. J. Sauer, "High-resistance regions produced in an $\text{In}_x\text{Ga}_y\text{Al}_{1-x-y}\text{As}$ system by He ion implantations," *J. Appl. Phys.*, vol. 64, pp. 3290–3292, 1988.
- [29] S. J. Pearton, C. R. Abernathy, M. B. Panish, R. A. Hamm, and L. M. Lunardi, "Implant-induced high-resistivity regions in InP and InGaAs," *J. Appl. Phys.*, vol. 66, no. 2, pp. 656–662, 15 July 1989.
- [30] R. G. Elliman, M. C. Ridgway, C. Jagadish, S. J. Pearton, F. Ren, J. Lothian, T. R. Fullowan, A. Katz, and C. R. Abernathy, "Single-energy, MeV implant isolation of multilayer III-V device structures," *J. Appl. Phys.*, vol. 71, no. 2, pp. 1010–1013, 15 Jan 1992.
- [31] S. J. Pearton, F. Ren, J. R. Lothian, T. R. Fullowan, A. Katz, P. W. Wisk, C. R. Abernathy, and R. F. Kopf, "Use of MeV O^+ ion implantation for isolation of GaAs/AlGaAs heterojunction bipolar transistors," *J. Appl. Phys.*, vol. 71, pp. 4949–4954, May 1992.
- [32] J. B. Biersack and L. G. Hagmark, *Nucl. Instrum. Meth.*, vol. 174, p. 237, 1980.
- [33] T. Henderson and B. Bayraktaroglu, "Base-emitter leakage and recombination current in an implant isolated region of a GaAs/AlGaAs heterojunction bipolar transistor," *J. Appl. Phys.*, vol. 72, no. 11, pp. 5489–5491, 1992.
- [34] G. Lengyel, K. W. Jelley, and R. W. H. Engelmann, "A semi-empirical model for electroabsorption in GaAs/AlGaAs multiple quantum well modulator structures," *IEEE J. Quant. Elec.*, vol. 26, pp. 296–304, Feb. 1990.
- [35] P. K. Bhattacharya, *Semiconductor Optoelectronic Devices*. New Jersey: Prentice Hall, 1994.
- [36] J. Singh, *Physics of Semiconductors and Their Heterostructures*. New York: McGraw-Hill, 1993.

- [37] G. Bastard, E. E. Mendez, L. L. Chang, and L. Esaki, "Variational calculations on a quantum well in an electric field," *Phys. Rev. B*, vol. 28, no. 6, pp. 3241–3245, 1983.
- [38] S. Goswami, S. C. Hong, D. Biswas, P. K. Bhattacharya, J. Singh, and W. Q. Li, "Low-power exciton-based heterojunction bipolar transistors for thresholding logic applications," *IEEE J. Quant. Elec.*, vol. 27, pp. 760–768, Mar. 1991.
- [39] W. Q. Li, S. Goswami, P. K. Bhattacharya, and J. Singh, "Programmable memory cell using quantum confined Stark effect in multi-quantum well heterojunction bipolar transistors," *Electron. Lett.*, vol. 27, pp. 31–32, Jan. 1991.
- [40] S. Goswami, L. Davis, S. C. Hong, P. K. Bhattacharya, and G. I. Haddad, "Negative differential resistance of GaAs/AlGaAs multiquantum well structures under high power photoexcitation: Structure optimization for an oscillator," *Electron. Lett.*, vol. 28, pp. 915–916, May 1992.
- [41] W. Q. Li, M. Karaküçük, P. N. Freeman, J. R. East, G. I. Haddad, and P. K. Bhattacharya, "High-speed $\text{Al}_{0.2}\text{Ga}_{0.8}\text{As}/\text{GaAs}$ multi-quantum-well phototransistors with tunable spectral response," *IEEE Elec. Dev. Lett.*, vol. 14, pp. 335–337, July 1993.
- [42] M. Karaküçük, W. Q. Li, P. N. Freeman, J. R. East, G. I. Haddad, and P. K. Bhattacharya, "A direct optically injection locked 2.6 GHz HBT oscillator," *Microwave Opt. Tech. Lett.*, vol. 6, pp. 609–611, Aug. 1993.
- [43] G. D. Vendelin, *Design of Amplifiers and Oscillators by the S-parameter method*. New York: Wiley, 1982.
- [44] S. W. Wedge, R. Compton, and D. Rutledge, *PUFF – Computer Aided Design for Microwave Integrated Circuits*. Pasadena: California Institute of Technology, 1991.
- [45] M. Armand, "On the output spectrum of unlocked driven oscillators," *Proc. IEEE*, vol. 57, pp. 798–799, 1969.
- [46] S. Naseen and T. J. Coutts, "Indium tin oxide / gallium arsenide solar cells," *J. Appl. Phys.*, vol. 58, pp. 4463–4463, 1 Dec 1985.
- [47] X. Li, M. W. Wanlass, T. A. Gessert, K. A. Emery, and T. J. Coutts, "High-efficiency indium tin oxide / indium phosphide solar cells," *Appl. Phys. Lett.*, vol. 54, pp. 2674–2676, June 1989.
- [48] D. G. Parker, "Use of transparent indium tin oxide to form a highly efficient 20 GHz Schottky barrier photodiode," *Electron. Lett.*, vol. 21, no. 18, pp. 777–778, 1985.

- [49] M. Zirngible, Y. Hu, R. Sachot, and M. Illegems, "Characterization of a top-illuminated p-i-n diode with indium tin oxide contact," *Appl. Phys. Lett.*, vol. 54, no. 21, pp. 2076–2078, 1989.
- [50] J. W. Seo, A. A. Ketterson, D. G. Ballegeer, K. Y. Cheng, I. Adesida, X. Li, and T. Dessert, "A comparative study of metal-semiconductor-metal photodetectors on GaAs with indium-tin-oxide and Ti/Au electrodes," *IEEE Photon. Technol. Lett.*, vol. 4, no. 8, pp. 888–890, 1992.
- [51] E. Shanthi, A. Bannerjee, V. Dutta, and K. L. Chopra, *J. Appl. Phys.*, vol. 53, p. 1615, 1982.
- [52] R. L. Weiher and B. G. Dick, *J. Appl. Phys.*, vol. 35, pp. 3511–3515, 1964.
- [53] M. Buchanan, J. B. Webb, and D. F. Williams, "Preparation of conducting and transparent thin films of tin-doped indium oxide by magnetron sputtering," *Appl. Phys. Lett.*, vol. 37, pp. 213–215, 15 Jul. 1980.
- [54] K. L. Chopra, S. Major, and D. K. Pandya, "Transparent conductors — a status review," *Thin Solid Films*, vol. 102, pp. 1–46, 1983.
- [55] I. Adesida, D. G. Ballegeer, J. W. Seo, A. Ketterson, H. Chang, K. Y. Cheng, and T. Gessert, "Etching of indium tin oxide in methane/hydrogen plasmas," *J. Vac. Sci. Technol. B*, vol. 9, no. 6, pp. 3551–3554, 1991.
- [56] T. J. Cunningham, L. J. Guido, J. C. Beggy, and R. C. Barker, "Annealed indium oxide transparent ohmic contacts to GaAs," *J. Appl. Phys.*, vol. 71, pp. 1070–1072, 15 Jan 1992.
- [57] P. R. Berger, N. K. Dutta, G. Zydzik, H. M. O'Bryan, U. Keller, P. R. Smith, J. Lopata, D. Sivco, and A. Y. Cho, "In_{0.52}Ga_{0.47}As p-i-n photodiodes with transparent cadmium tin oxide contacts," *Appl. Phys. Lett.*, vol. 61, no. 14, pp. 1673–1675, 1992.
- [58] L. Tu, E. F. Schubert, H. M. O'Bryan, Y. Wang, B. E. Weir, G. J. Zydzik, and A. Y. Cho, "Transparent conductive metal-oxide contacts in vertical-injection top-emitting quantum well lasers," *Appl. Phys. Lett.*, vol. 58, no. 8, pp. 790–792, 1991.
- [59] Y. Shapira, H. Aharoni, and J. Bregman, "Effects of oxygen partial pressure during deposition on the properties of ion-beam-sputtered indium-tin-oxide thin films," *J. Appl. Phys.*, vol. 67, pp. 3750–3753, Apr. 15 1990.
- [60] S. M. Sze, *Physics of Semiconductor Devices*. New York: Wiley, 2nd ed., 1981.
- [61] W. Q. Li, J. Kulman, M. Karaküçük, J. P. East, G. I. Haddad, and P. K. Bhattacharya, "High frequency GaAs/Al_{0.2}Ga_{0.8}As heterojunction bipolar

- transistors with transparent indium-tin-oxide emitter contacts," *Electron. Lett.*, vol. 29, no. 25, pp. 2217–2219, 1993.
- [62] P. N. Freeman, M. Karaküçük, W. Q. Li, J. R. East, G. I. Haddad, and P. K. Bhattacharya, "Optically controlled microwave oscillators fabricated using GaAs / AlGaAs HBTs with transparent ITO emitter contacts," in *Optoelectronic Signal Processing for Phased-Array Antennas IV* (B. M. Hendrickson, ed.), pp. 24–28, Proc. SPIE 2155, Jan. 1994.
 - [63] P. N. Freeman, M. Karaküçük, and P. K. Bhattacharya, "Optical tuning behavior of $\text{Al}_{0.25}\text{Ga}_{0.75}\text{As}/\text{GaAs}$ HBT oscillators with transparent ITO emitter contacts," *Microwave Opt. Tech. Lett.*, July 1995.
 - [64] W. L. Chen, J. C. Cowles, G. I. Haddad, G. O. Munns, K. W. Eisenbeiser, and J. R. East, "Ohmic contact study for quantum effect transistors and heterojunction bipolar transistors with InGaAs contact layers," *J. Vac. Sci. Technol. B*, vol. 10, no. 6, pp. 2354–2360, 1992.
 - [65] G. Y. Robinson, *Solid State Elect.*, vol. 18, p. 331, 1975.
 - [66] M. Shur, *Physics of Semiconductor Devices*. New Jersey: Prentice Hall, 1990.
 - [67] H. Fukano, Y. Takanashi, and M. Fujimoto, "High-speed InP-InGaAs heterojunction phototransistors employing a nonalloyed electrode metal as a reflector," *IEEE J. Quant. Elec.*, vol. 30, pp. 2889–2895, Dec. 1994.
 - [68] D. Wake, D. J. Newson, M. J. Harlow, and I. D. Henning, "Optically-biased, edge-coupled InP/InGaAs heterojunction phototransistors," *Electron. Lett.*, vol. 29, no. 25, pp. 2223–2225, 9 Dec. 1993.
 - [69] M. J. Mondry, D. I. Babic, J. E. Bowers, and L. A. Coldren, "Refractive indexes of (Al, Ga, In)As epilayers on InP for optoelectronic applications," *IEEE Photon. Technol. Lett.*, vol. 4, pp. 627–630, June 1992.
 - [70] I. Vurgaftman, P. N. Freeman, P. K. Bhattacharya, and J. Singh, "Time-domain optical wave propagation in disordered and nonuniform guiding structures," *submitted to IEEE J. Quant. Elec.*, 1995.
 - [71] S. H. Lin, S. Y. Wang, and Y. M. Houng, *Appl. Phys. Lett.*, vol. 51, p. 83, 1987.
 - [72] R. G. Walker, I. Bennion, and A. C. Carter, *Electron. Lett.*, vol. 25, p. 1549, 1989.
 - [73] K. Wakita, I. Kotaka, O. Mitomi, H. Asai, and Y. Kawamura, "High-speed InGaAs/InAlAs MQW optical modulators with bandwidths in excess of 40 GHz at $1.55\ \mu\text{m}$," in *Proc. Conf. Lasers Electro-Opt. 1990, Tech. Dig. Ser.*, vol. 7, pp. 70–71, 1990.

- [74] H. Tanaka, M. Suzuki, M. Usami, H. Taga, S. Yamamoto, and Y. Matsushima, *J. Lightwave Tech.*, vol. 48, p. 1357, 1990.
- [75] T. H. Wood, C. A. Burrus, D. A. B. Miller, D. S. Chemla, T. C. Damen, A. C. Gossard, and W. Wiegmann, "High-speed optical modulation with GaAs/AlGaAs quantum wells in a p-i-n diode structure," *Appl. Phys. Lett.*, vol. 44, p. 16, 1984.
- [76] U. Koren, B. I. Miller, T. L. Koch, G. Eisenstein, R. S. Tucker, I. BarJoseph, and D. S. Chemla, *Appl. Phys. Lett.*, vol. 51, p. 1132, 1987.
- [77] M. Suzuki, H. Tanaka, and S. Akiba, *Electron. Lett.*, vol. 25, p. 88, 1989.
- [78] R. E. Cavicchi, D. V. Lang, D. Gershoni, A. M. Sergent, H. Temkin, and M. Panish, *Phys. Rev. B*, vol. 38, p. 13475, 1988.
- [79] J. E. Zucker, M. Wegener, K. L. Jones, T. Y. Chang, N. J. Sauer, and D. S. Chemla, *Appl. Phys. Lett.*, vol. 56, p. 1951, 1990.
- [80] M. Wegener, T. Y. Chang, I. Bar-Joseph, J. M. Kuo, and D. S. Chemla, "Electroabsorption and refraction by electron transfer in asymmetric modulation-doped multiple quantum well structures," *Appl. Phys. Lett.*, vol. 55, pp. 583-585, 7 Aug 1989.
- [81] J. E. Zucker, K. L. Jones, M. Wegener, T. Y. Chang, N. J. Sauer, M. D. Divino, and D. S. Chemla, "Multi-gigahertz-bandwidth intensity modulators using tunable-electron-density multiple quantum well waveguides," *Appl. Phys. Lett.*, vol. 59, pp. 201-203, 8 Jul 1991.
- [82] D. H. Hartman, Y. Takahashi, and H. Inoue, *Electron. Lett.*, vol. 26, p. 436, 1990.
- [83] S. M. Sze, ed., *High-Speed Semiconductor Devices*. New York: Wiley, 1990.
- [84] M. D. Jaffe, *Studies on the Electronic Properties and Applications of Coherently Strained Semiconductors*. PhD thesis, The University of Michigan, Ann Arbor, 1989.
- [85] K. Wakita, Y. Kawamura, M. Nakao, and H. Asai, "Long-wavelength waveguide multiple quantum well optical modulators," *IEEE J. Quant. Elec.*, vol. 23, p. 2210, 1987.
- [86] I. Kotaka, K. Wakita, K. Kawano, M. Asai, and M. Naganuma, "High-speed and low-driving voltage InGaAs/InAlAs multiquantum well optical modulators," *Electron. Lett.*, vol. 27, pp. 2163-2164, Nov. 1991.
- [87] T. Ido, H. Sano, S. Tanaka, and H. Inoue, "High-speed MQW electroabsorption optical modulators integrated with low-loss waveguides," *IEEE Photon. Technol. Lett.*, vol. 7, pp. 170-172, Feb. 1995.

DISTRIBUTION LIST

addresses	number of copies
JAMES R. HUNTER ROME LABORATORY/OCPC 25 ELECTRONIC PKY ROME NY 13441-4515	10
UNIVERSITY OF MICHIGAN DEPT OF EE & COMPUTER SCIENCE ANN ARBOR MI 48109-2122	5
ROME LABORATORY/SUL TECHNICAL LIBRARY 26 ELECTRONIC PKY ROME NY 13441-4514	1
ATTENTION: DTIC-DCC DEFENSE TECHNICAL INFO CENTER 8725 JOHN J. KINGMAN ROAD, STE 0944 FT. BELVOIR, VA 22060-6218	2
ADVANCED RESEARCH PROJECTS AGENCY 3701 NORTH FAIRFAX DRIVE ARLINGTON VA 22203-1714	1
ROME LABORATORY/C3AB 525 BROOKS RD ROME NY 13441-4505	1
ATTN: RAYMOND TADROS GIDEP P.O. BOX 8000 CORONA CA 91718-8000	1
ATTN: WALTER HARTMAN WRIGHT LABORATORY/AAM, BLDG. 620 2241 AVIONICS CIRCLE, RM N3-F10 WRIGHT-PATTERSON AFB OH 45433-7333	1

AFIT ACADEMIC LIBRARY/LDEE 1
2950 P STREET
AREA B, BLDG 642
WRIGHT-PATTERSON AFB OH 45433-7765

ATTN: R.L. DENISON 1
WRIGHT LABORATORY/MLPD, BLDG. 651
3005 P STREET, STE 6
WRIGHT-PATTERSON AFB OH 45433-7707

WRIGHT LABORATORY/MTM, BLDG 653 1
2977 P STREET, STE 6
WRIGHT-PATTERSON AFB OH 45433-7739

WRIGHT LABORATORY/FIVS/SURVIAC 1
2130 EIGHTH STREET, BLDG 45, STE 1
WRIGHT-PATTERSON AFB OH 45433-7542

ATTN: GILBERT G. KUPERMAN 1
AL/CFHI, BLDG. 248
2255 H STREET
WRIGHT-PATTERSON AFB OH 45433-7022

DL AL HSC/HRG, BLDG. 190 1
2698 G STREET
WRIGHT-PATTERSON AFB OH 45433-7604

AUL/LSAD 1
600 CHENNAULT CIRCLE, BLDG. 1405
MAXWELL AFB AL 36112-6424

US ARMY STRATEGIC DEFENSE COMMAND 1
CSSD-IM-PA
P.O. BOX 1500
HUNTSVILLE AL 35807-3801

NAVAL AIR WARFARE CENTER 1
6000 E. 21ST STREET
INDIANAPOLIS IN 46219-2189

COMMANDING OFFICER NCCOSC RDT&E DIVISION ATTN: TECHNICAL LIBRARY, CODE 0274 53560 HULL STREET SAN DIEGO CA 92152-5001	1
COMMANDER, TECHNICAL LIBRARY 474700D/C0223 NAVAIRWARCENWPNDIV 1 ADMINISTRATION CIRCLE CHINA LAKE CA 93555-6001	1
SPACE & NAVAL WARFARE SYSTEMS COMMAND (PMW 178-1) 2451 CRYSTAL DRIVE ARLINGTON VA 22245-5200	2
SPACE & NAVAL WARFARE SYSTEMS COMMAND, EXECUTIVE DIRECTOR (PD13A) ATTN: MR. CARL ANDRIANI 2451 CRYSTAL DRIVE ARLINGTON VA 22245-5200	1
COMMANDER, SPACE & NAVAL WARFARE SYSTEMS COMMAND (CODE 32) 2451 CRYSTAL DRIVE ARLINGTON VA 22245-5200	1
CDR, US ARMY MISSILE COMMAND RSIC, BLDG. 4484 AMSMI-RD-CS-R, DOCS REDSTONE ARSENAL AL 35898-5241	2
ADVISORY GROUP ON ELECTRON DEVICES SUITE 500 1745 JEFFERSON DAVIS HIGHWAY ARLINGTON VA 22202	1
REPORT COLLECTION, CIC-14 MS P364 LOS ALAMOS NATIONAL LABORATORY LOS ALAMOS NM 87545	1
AEDC LIBRARY TECHNICAL REPORTS FILE 100 KINDEL DRIVE, SUITE C211 ARNOLD AFB TN 37389-3211	1

COMMANDER
USAISC
ASHC-IMD-L, BLDG 61801
FT HUACHUCA AZ 85613-5000

1

US DEPT OF TRANSPORTATION LIBRARY
FB10A, M-457, RM 930
800 INDEPENDENCE AVE, SW
WASH DC 22591

1

AFIWC/MSO
102 HALL BLVD, STE 315
SAN ANTONIO TX 78243-7016

1

DIRNSA
R509
9800 SAVAGE ROAD
FT MEADE MD 20755-6000

1

NSA/CSS
K1
FT MEADE MD 20755-6000

1

PHILLIPS LABORATORY
PL/TL (LIBRARY)
5 WRIGHT STREET
HANSCOM AFB MA 01731-3004

1

THE MITRE CORPORATION
ATTN: E. LADURE
D460
202 BURLINGTON RD
BEDFORD MA 01732

1

OUSD(P)/DTSA/DUTD
ATTN: PATRICK G. SULLIVAN, JR.
400 ARMY NAVY DRIVE
SUITE 300
ARLINGTON VA 22202

2

~~ROME LABORATORY/ERAA~~
~~ATTN: DAVID D. CURTIS~~
~~HANSCOM AFB, MA 01731-5000~~

~~1~~

ROME LABORATORY/ERD 1
ATTN: RICHARD PAYNE
HANSCOM AFB, MA 01731-5000

ROME LABORATORY/EROC 1
ATTN: JOSEPH P. LORENZO, JR.
HANSCOM AFB, MA 01731-5000

ROME LABORATORY/ERDP 1
ATTN: JOSEPH L. HORNER
HANSCOM AFB, MA 01731-5000

ROME LABORATORY/EROC 1
ATTN: RICHARD A. SOREF
HANSCOM AFB, MA 01731-5000

ROME LABORATORY/ERXE 1
ATTN: JOHN J. LARKIN
HANSCOM AFB, MA 01731-5000

ROME LABORATORY/ERDR 1
ATTN: DANIEL J. BURNS
525 BROOKS RD
ROME NY 13441-4505

ROME LABORATORY/IRAP 1
ATTN: ALBERT A. JAMBERDINO
32 HANGAR RD
ROME NY 13441-4114

ROME LABORATORY/OCP 1
ATTN: BRIAN M. HENDRICKSON
25 ELECTRONIC PKY
ROME NY 13441-4515

ROME LABORATORY/OCPC 1
ATTN: GREGORY J. ZAGAR
25 ELECTRONIC PKY
ROME NY 13441-4515

ROME LABORATORY/C38C 1
ATTN: ROBERT L. KAMINSKI
525 BROOKS RD
ROME NY 13441-4505

ROME LABORATORY/DCP 1
ATTN: JAMES W. CUSACK
25 ELECTRONIC PKY
ROME NY 13441-4515

ROME LABORATORY/DCP 1
ATTN: JOANNE L. ROSSI
25 ELECTRONIC PKY
ROME NY 13441-4515

ROME LABORATORY/DCPA 1
ATTN: ANDREW R. PIRICH
25 ELECTRONIC PKY
ROME NY 13441-4515

ROME LABORTORY/DCP 1
ATTN: RICHARD J. MICHALAK
25 ELECTRONIC PKY
ROME NY 13441-4515

NY PHOTONIC DEVELOPMENT CORP 1
MVCC ROME CAMPUS
UPPER FLOYD AVE
ROME, NY 13440

NRAD/CODE 55 1
ATTN: DR. STEVE PAPPERT
SAN DIEGO CA 92152-5000

PHILLIPS LABORATORY/VTET 2
ATTN: MR. EDWARD W. TAYLOR
3550 ABERDEEN AVENUE SE, BLDG 902
KIRTLAND AFB NM 87117-5776

LABORATORY FOR PHYSICAL SCIENCES 1
ATTN: DONALD LA FAW
4928 COLLEGE AVENUE
COLLEGE PARK MD 20740

WRIGHT LABORATORY/XPN
ATTN: E. UTT
BLDG 254
2591 "K" STREET
WRIGHT-PATTERSON AFB OH 45433-7602

3

USA PHOTONICS RESEARCH CELL
ATTN: LTC A. H. SAYLES
DEPT OF EE AND CS
UNITED STATES MILITARY ACADEMY
WEST POINT, NY 10996

2

USA/CECOM
ATTN: AMSEL-RD-C3-AC-L
ATTN: J. WRIGHT/L. CORYELL
FORT MONMOUTH NJ 07703-5205

2

MISSION OF ROME LABORATORY

Mission. The mission of Rome Laboratory is to advance the science and technologies of command, control, communications and intelligence and to transition them into systems to meet customer needs. To achieve this, Rome Lab:

- a. Conducts vigorous research, development and test programs in all applicable technologies;
- b. Transitions technology to current and future systems to improve operational capability, readiness, and supportability;
- c. Provides a full range of technical support to Air Force Material Command product centers and other Air Force organizations;
- d. Promotes transfer of technology to the private sector;
- e. Maintains leading edge technological expertise in the areas of surveillance, communications, command and control, intelligence, reliability science, electro-magnetic technology, photonics, signal processing, and computational science.

The thrust areas of technical competence include: Surveillance, Communications, Command and Control, Intelligence, Signal Processing, Computer Science and Technology, Electromagnetic Technology, Photonics and Reliability Sciences.